

# Quantum Traits in the Dynamics of Biomolecular Systems

Edward J. O'Reilly

Department of Physics & Astronomy

University College London

A thesis submitted for the degree of

*Doctor of Philosophy*

I, Edward J. O'Reilly confirm that the work presented in this thesis is my own. Where information has been derived from other sources, I confirm that this has been indicated in the thesis.

Edward J. O'Reilly

## Acknowledgements

It is a pleasure to acknowledge the supervision and support afforded to me by Alexandra Olaya-Castro throughout my studies. I would like to express thanks to all collaborators - it has been rewarding partnership. Special thanks are also due to past and present members of the Olaya-Castro group for helpful discussions and fruitful collaborations: Avinash Kolli, Hoda Hossein-Nejad, Francesca Fassioli, Richard Stones and David Holdaway. This work was supported by the Engineering and Physical Research Council (EPSRC) [EP/G005222/1]. Finally I would like to thank my friends and family for their support.

# Abstract

The majority of biology can be adequately described by classical laws, yet there are suggestions that a variety of organisms may harness non-trivial quantum phenomena to gain a biological advantage. This thesis is concerned with the light induced dynamics in photosynthetic light harvesting antennae. Quantum coherences persisting on picosecond time-scales have been repeatedly observed in a variety of species. This ran contrary to the prevailing theories of energy transfer dynamics in these systems. A consensus has emerged that a delicate competition between electronic and vibrational interactions is responsible for prolonging coherences between electronic states of chromophores. In particular, interactions with specific under-damped vibrational modes are known to play a fundamental role.

This thesis demonstrates that room temperature, efficient vibration-assisted energy transfer in a biologically relevant exciton-vibration dimers can manifest and benefit from non-classical fluctuations of collective pigment motions. The inadequacy of a classical description of selected vibrations is further illustrated by identifying features of electronic dynamics that are enhanced by quantum properties. A quantum-thermodynamical formalism describing heat and work fluxes between partitions of a closed quantum system is extended to open quantum systems in the non-perturbative regime. This reveals non-trivial relations between the electronic interactions among chromophores and the relative contribution of work- and heat-like energy fluxes between electronic and vibrational motions. This in turn highlights relations between structure and energy transformations in photosynthetic complexes. Finally, the thesis investigates energy transfer within and between antennae of purple bacteria acclimated to different illumination conditions. The protein composition is altered depending on the light levels. Consequently, the electronic energy landscape is modified to accelerate intra-complex energy transfer without detriment to inter-complex transfer, thereby promoting or diminishing resonances with specific vibrational motions. This suggests that acclimation may serve to exploit non-trivial quantum phenomena.



# Contents

<b>Contents</b>	<b>iv</b>
<b>Introduction</b>	<b>1</b>
<b>1 Theory of quantum dynamics in biomolecular systems</b>	<b>7</b>
1.1 Theoretical framework: open quantum systems . . . . .	7
1.1.1 Hamiltonian description of biomolecules . . . . .	9
1.1.2 Reduced system dynamics . . . . .	11
1.1.3 Bath correlation and spectral densities . . . . .	12
1.2 Perturbative approaches to quantum dynamics . . . . .	15
1.2.1 Redfield theory . . . . .	15
1.2.2 Förster theory . . . . .	17
1.3 Interpolating approaches to quantum dynamics . . . . .	18
1.3.1 Hierarchical expansion of dynamics . . . . .	18
1.3.2 Other approaches . . . . .	20
1.4 Quantum traits in electronic and vibrational dynamics . . . . .	21
1.4.1 Quantum coherence . . . . .	21
1.4.2 Exciton delocalization . . . . .	22
1.4.3 Quasiprobabilities . . . . .	23
1.4.4 Non-classical statistics . . . . .	24
<b>2 Non-classicality of molecular vibrations</b>	<b>26</b>
2.1 Prototype dimers and collective vibrations . . . . .	28
2.2 Non-classicality via coherent exciton-vibrational dynamics . . . . .	31
2.3 Dynamics under thermal relaxation . . . . .	33
2.3.1 Non-classicality . . . . .	35
2.4 The functional role of non-classicality . . . . .	37
2.5 Concluding remarks and outlook . . . . .	40
2.A LHCII Chl <sub>(b601)</sub> -Chl <sub>(a602)</sub> dimer . . . . .	42

<b>3</b>	<b>Quantum enhanced features of vibration-assisted excitation energy transport</b>	<b>43</b>
3.1	Quasiclassical description of molecular vibrations . . . . .	44
3.2	Cryptophyte antennae proteins . . . . .	46
3.3	Quantum enhanced transport and directionality . . . . .	48
3.4	Exciton population oscillations . . . . .	50
3.4.1	Quantum coherent exciton-vibration dynamics . . . . .	51
3.4.2	Classical exciton-vibration dynamics . . . . .	53
3.4.3	Thermalisation of classical vibrations . . . . .	54
3.5	Energy storage . . . . .	55
3.6	Concluding remarks and outlook . . . . .	57
3.A	Electronic parameters of PE545 and PC645 subunits . . . . .	59
<b>4</b>	<b>Work exchange and the thermodynamic implications of non-equilibrium vibrations</b>	<b>60</b>
4.1	Energy fluxes in the quantum regime . . . . .	61
4.1.1	Measurements . . . . .	62
4.2	Work and heat exchange between quantum systems . . . . .	63
4.3	Work and heat fluxes in an exciton-vibration dimer . . . . .	65
4.3.1	Electronically uncoupled chromophores: ( $J = 0$ ) . . . . .	65
4.3.2	Electronically coupled chromophores: ( $J \neq 0$ ). . . . .	66
4.3.3	Work source quality . . . . .	68
4.4	Work exchange with structured environments . . . . .	69
4.4.1	Calculating bath observables within the open systems approach	70
4.4.2	Work and heat fluxes in a tetrameric system . . . . .	70
4.5	Work exchange under continuous illumination . . . . .	74
4.6	Concluding remarks and outlook . . . . .	79
<b>5</b>	<b>Acclimation of energy transfer</b>	<b>82</b>
5.1	Spectral adaptation of the photosynthetic apparatus of purple bacteria	82
5.1.1	The light harvesting 2 (LH2) antenna complex . . . . .	84
5.2	Linear spectroscopy . . . . .	86
5.2.1	Comparison of perturbative theories . . . . .	88
5.2.2	Inhomogeneous line broadening . . . . .	90
5.3	Generalizations of Förster theory . . . . .	91
5.4	Acclimation of intra-complex energy transfer . . . . .	92
5.4.1	Electronic parameters . . . . .	92

## CONTENTS

---

5.4.2	Environmental parameters . . . . .	94
5.4.3	Calculated linear spectra . . . . .	94
5.4.4	B800-B850 energy transfer . . . . .	96
5.4.5	B800-B850 energy transfer dynamics . . . . .	98
5.5	Acclimation of inter-complex energy transfer . . . . .	100
5.5.1	B850-B850 transfer rates . . . . .	100
5.6	Concluding remarks and outlook . . . . .	102
5.A	LH2 structural data . . . . .	105
<b>6</b>	<b>Final Remarks and Outlook</b>	<b>107</b>
	<b>References</b>	<b>110</b>

# Introduction

Quantum biology is the emerging research field concerned with investigating the extent to which organisms may have exploited the laws of quantum mechanics to gain an evolutionary advantage [1–3]. Clearly, the dynamics of every physical system is inherently quantum mechanical and biological ones in particular, are decidedly reliant on the stability of chemical bonding and molecular structure. It is therefore important to make a distinction between this type of undisputed and quite apparent quantum phenomena, and the more controversial ‘non-trivial’ quantum effects posited to play a functional role in some biological systems. The majority of biology can be adequately described by classical laws, yet there are suggestions that a variety of organisms may harness non-trivial quantum phenomena to gain a biological advantage (Fig. 1).

This thesis is concerned with the light-induced dynamics in photosynthetic light harvesting antennae. The role of these antennae is to absorb photons as electronic excitations and rapidly transfer the associated energy to a reaction centre where charge separation takes place [4]. This charge separation enables a series of electron transport reactions which result in stable forms of chemical energy. Energy transfer in light harvesting antennae is efficient - nearly all absorbed photons reach a reaction centre because the transport takes place much faster than the lifetime of the excitation. Electronic energy transfer between the chromophores in antennae was thought to be incoherent, as described by Förster theory [5–7]. This incoherent mechanism was long debated [8, 9], but proved difficult to experimentally determine. The advent of two-dimensional electronic spectroscopy now means that quantum coherences which last for physiological time-scales have been repeatedly observed in a variety of species [10–17]. The persistence of these quantum coherent contributions to dynamics on the timescale of energy transfer has lead many to suggest that this quantum trait aids the efficiency of energy transfer and that the environment of antennae is delicately structured to optimize the energy transfer dynamics.

Photosynthesis is not the only example of non-trivial quantum phenomena in

nature. Avian magnetoreception - the ability of birds to orient themselves in the geomagnetic field has also been the centre of a debate. A mechanism based on the sensitivity of the yield of radical-pair reactions to the magnetic field orientation has been proposed [18–20]. It is thought that light-initiated electron transfer reactions within cryptochrome molecules results in the formation of radical-pairs which have anisotropic hyperfine interactions with nearby nuclei. The resulting inter-conversion of singlet and triplet spin states is sensitive to the orientation of the geomagnetic field. The precise nature of the radical pairs is unknown, although those within cryptochrome molecules are considered a possible candidate. Interestingly there is recent evidence that the expression of cryptochrome depends on the birds migratory status [21]. Although as yet there is no direct experimental verification of the radical pair mechanism, there are models [22–25] whose features are consistent with the results of behavioural experiments in animals [26–29]. Extraordinarily, in order to be consistent with such experiments some of these models require that long-lived superposition and entanglement are sustained for at least tens of microseconds. The sustenance of these non-trivial quantum phenomena in a biological system for so long - ‘*beyond that of any artificial molecular system*’ [23] would indeed be remarkable.

Recently it has been demonstrated that rod cells isolated from African clawed toads can be used to detect single photons [30]. The sensitivity of photoreceptors to a quantum state of light lends weight to suggestions that light-initiated dynamics in isomerisation of the retinal molecule in the ubiquitous rhodopsin pigment may involve quantum phenomena [31]. Although no experiment has yet to directly probe quantum phenomena in photoreceptors, coherent control of retinal isomerisation has been achieved [32, 33].

It may transpire that quantum phenomena are more widespread in biology than previously assumed. It is hoped that a greater understanding of the ways in which biology has utilized the advantages of quantum phenomena, can inspire the design of new technologies.

## Thesis overview

The main purpose of this thesis is to study light induced dynamics in photosynthetic light harvesting antennae. The observation of long-lived quantum coherences in photosynthetic light harvesting antennae ran contrary to the prevailing theories of energy transfer dynamics in these systems. Strong interactions with protein, solvent, intra and inter-molecular vibrational motions were thought to result in an

incoherent transfer between chromophores. In this case the rates of transfer are described by Förster theory [5–7], which assumes coupling between chromophores can be treated as a perturbation with respect to coupling to the environment. In fact, these coupling strengths are comparable in many light harvesting antennae, meaning that non-perturbative theories are needed to adequately describe energy transfer dynamics. An appropriately sophisticated theoretical description of such systems can elucidate the origin of long-lived coherences and capture other non-trivial quantum traits in dynamics. **Chapter 1** therefore presents a theoretical framework for the description of light-initiated excitation dynamics in biomolecular systems and details the potential non-trivial quantum features that might be observed.

A consensus has emerged that a delicate competition between electronic and vibrational interactions is responsible for prolonging coherences between electronic states of chromophores in light harvesting antenna. In particular, interactions with specific under-damped vibrational modes are thought to play a fundamental role. Nevertheless, criticism and scepticism are abound - classical models reproducing the same phenomena have been argued for. In **Chapter 2** the joint dynamics of electronic and vibrational modes in a prototype dimer present in a variety of photosynthetic antennae are shown to result in an *unambiguously* quantum mechanical (non-classical) state of the vibrational mode. Efficient energy transfer between chromophores is shown to be assisted by non-classical vibrational motion.

The proposition that quantum mechanics is required to fully appreciate the function of biological systems invites the question - what is lost when a classical description is imposed? Clearly many systems can be adequately described with classical models, while others feature quantum properties that cannot be neglected. In **Chapter 3** we compare the electronic excitation dynamics resulting from quantum mechanical and classical descriptions of vibrational motions. Larger systems are studied, which enables us to identify a number of features of electronic dynamics which can be enhanced by quantized vibrations. In the systems studied, the classical model of vibrations is less able to direct energy towards particular chromophores, does not predict the oscillatory transfer of energy between the electronic and vibrational components seen with quantized vibrations and cannot account correctly for storage of energy in vibrations.

Biomolecular systems operate far from thermal equilibrium in the presence of significant fluctuations. The continued survival of a biological system depends on its ability to efficiently sustain an ordered, non-equilibrium state whilst producing entropy [34]. Current understanding of non-equilibrium processes relies mainly

on equilibrium concepts. Modern theoretical developments in the area of non-equilibrium statistical mechanics such as the Jarzynski and Crooks relations [35, 36] have triggered a resurgence of interest in understanding the thermodynamics of small systems particularly quantum mechanical ones. An analogy can be made between some biological systems and traditional thermodynamic heat engines in that both exploit heat fluxes from thermal reservoirs to perform useful work. It is known that coherence can increase the power of a quantum heat engine. To what extent do biomolecular systems harness the laws of quantum thermodynamics? In **Chapter 4** we contribute towards this understanding, by partitioning the flux of energy between quantum systems into work-like and heat-like contributions. By adopting this formalism we are able to demonstrate that in light harvesting antennae, quantized vibrational modes can act as both a work source and heat source and that this is dependent on the topology of electronic couplings among chromophores.

Amongst species which perform photosynthetic light harvesting, there is a huge range of different antennae types. Although in each case the antenna serves the same functional role, environmental factors have caused nature to explore alternative structures to achieve the same outcome. For example, competition for photons at a certain energy may result in the production of antenna which absorbs in an alternative region of the spectrum. The different proteins and arrangements of chromophores in these systems results in a different set of electronic and vibrational interaction strengths. This requires an evaluation of the extent of quantum traits in each species. Even within the same species, different antenna are produced in response to altering environmental conditions. Such acclimation occurs in purple photosynthetic bacteria in low illumination conditions. The new antenna are assembled using a different set of proteins. This results in altered spectroscopic properties. In **Chapter 5**, the theory of linear spectroscopy is briefly reviewed and applied to antennae complexes from purple bacteria acclimated to different illumination conditions. Parameters consistent with the experimental absorption spectra are used to investigate energy transfer within and between antennae complexes from purple bacteria. This lays the groundwork for future study of the acclimation of quantum traits.

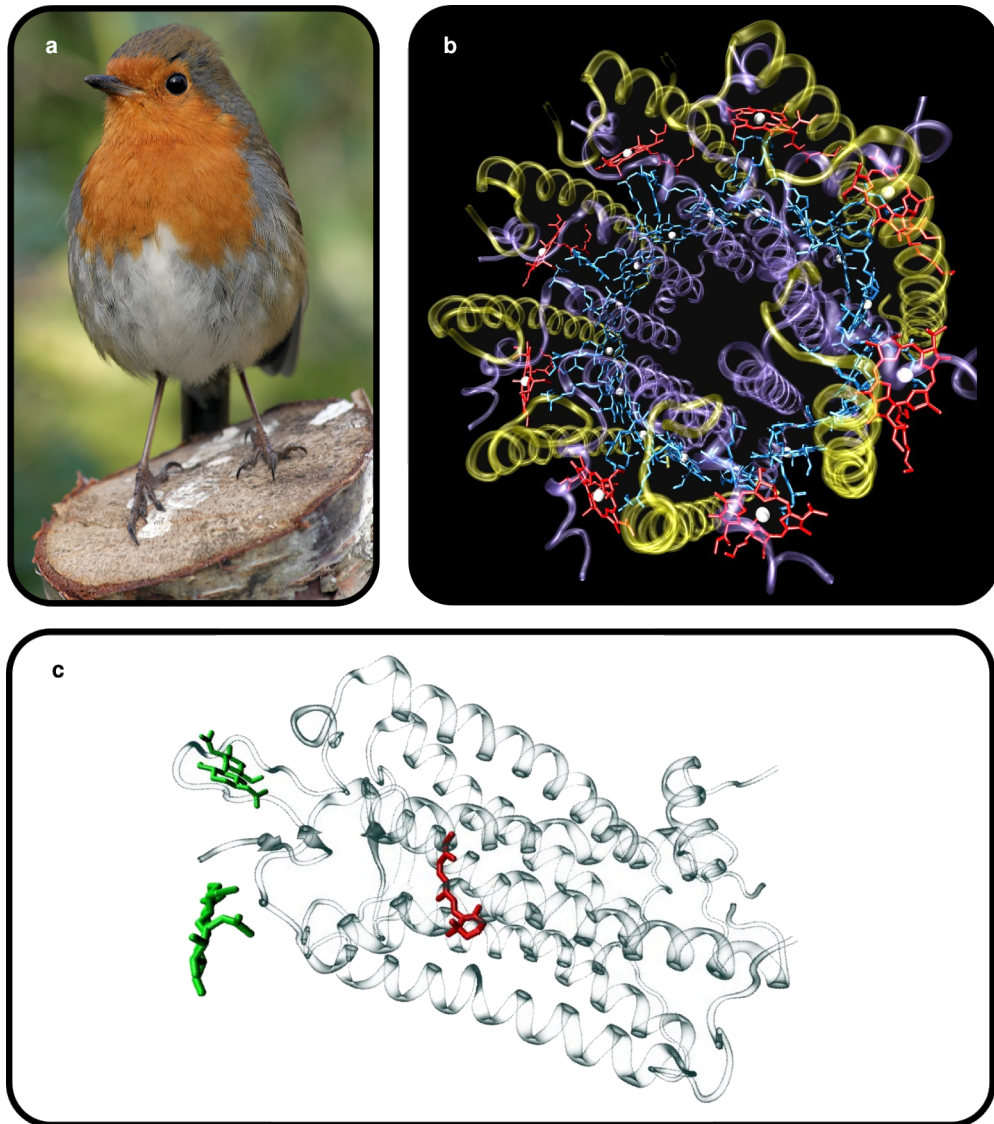


Figure 1: (a) European robin, (b) light harvesting 2 complex from purple bacteria (c) rhodopsin pigment



## Publications

The following publications are the result of work contributing to this thesis.

- [37] Kolli, A., O'Reilly, E. J., Scholes, G. D. & Olaya-Castro, A. The fundamental role of quantized vibrations in coherent light harvesting by cryptophyte algae. *J. Chem. Phys.* **137**, 174109 (2012).
- [38] O'Reilly, E. J. & Olaya-Castro, A. Non-classicality of the molecular vibrations assisting exciton energy transfer at room temperature *Nat. Commun.* **5**, (2014).
- [39] Hossein-Nejad, H., Albert, V. V., O'Reilly, E. J. & Scholes, G. D. Corrigendum: Energy transfer, entanglement and decoherence in a molecular dimer interacting with a phonon bath (2010 new j. phys. 12 065045). *New J. Phys.* **16**, 019502 (2014).
- [40] Viani, L., Corbella, M., Curutchet, C., O'Reilly, E. J., Olaya-Castro, A., & Mennucci, B. Molecular basis of the exciton-phonon interactions in the PE545 light-harvesting complex. *Phys. Chem. Chem. Phys.* **16**, 16302–16311 (2014).

# Chapter 1

## Theory of quantum dynamics in biomolecular systems

*This chapter presents a theoretical framework for the description of light-initiated excitation dynamics in biomolecular systems. The open quantum system approach is outlined and common perturbative treatments to describe quantum dynamics are reviewed. The non-perturbative hierarchical expansion of reduced system dynamics employed throughout this thesis is discussed, while other approaches are briefly reviewed. Finally, measures of the quantum traits of electronic and vibrational dynamics are described.*

### 1.1 Theoretical framework: open quantum systems

The dynamics of an isolated quantum system is described by the Liouville-von Neumann equation  $\dot{\rho}_S = -i[H_S, \rho_S]$ , where  $H_S$  is the Hamiltonian describing the system and  $\rho_S$  is the corresponding density matrix/operator [41]. Here and throughout this thesis  $\hbar = 1$ . The use of a density matrix enables the description of system dynamics where the state not known with certainty, for example, where imperfect experimental preparation results in a statistical mixture of states. The density operator also describes ensembles of many systems.

In reality no experimental system is truly isolated - there are always interactions with external degrees of freedom. If the number of relevant external degrees of freedom is small, the full Schrödinger equation can be propagated for an expanded system which includes these extra degrees of freedom explicitly which are then traced

Figure 1.1: **(a)** Schematic of the open quantum system approach to describing excitation dynamics in biomolecules. Protein (represented as ribbons) and solvent degrees of freedom constitute an environment which interacts with electronic excitations of individual chromophores. The  $Q_y$  transition for the chlorophyll molecule is indicated with a purple arrow. **(b)** Upon excitation of a chromophore, the system undergoes a vertical transition gaining energy  $\epsilon_i + \lambda_i$ . The nuclear potential energy surface is shifted by  $d_i$  and the vibrational state evolves to a new equilibrium position. If there is no coupling to other chromophores, the energy is emitted as photons of energy  $\epsilon_i - \lambda_i$  resulting in a Stokes shift  $2\lambda_i$  between absorption and fluorescence spectra [44].

away to yield the dynamics of the reduced system. For systems where many degrees of freedom are relevant (as is the case for biomolecular systems) this is not usually a practical approach, therefore the framework of open quantum systems [42, 43] is needed. This approach partitions the total system into a reduced system S and an environment or bath B,

$$H = H_S + H_B + H_{SB} . \quad (1.1)$$

The bath degrees of freedom are then formally traced away  $\rho_S = \text{Tr}_B[\rho]$  and only the influence of the bath on the system is described. Usually the system comprises experimentally relevant degrees of freedom so that the dynamics of  $\rho_S$  predicts the outcomes of measurements.

As a pertinent example, for a light harvesting complex the system would be the relevant excited states of each of the chromophores while the environment might be the quantized vibrational motion of the protein and solvent, as well as the inter and intra-molecular vibrational motions of the chromophores themselves. This is indicated schematically in Fig. 1.1(a).

### 1.1.1 Hamiltonian description of biomolecules

**Electronic Hamiltonian** For light harvesting antenna comprising  $N$  chromophores, the Hamiltonian describing the electronic excited states is given by [45]

$$H_S = \sum_i^N \epsilon_i \sigma_i^+ \sigma_i^- + \sum_{i,j \leq i}^N V_{ij} (\sigma_i^+ \sigma_j^- + \sigma_j^+ \sigma_i^-) , \quad (1.2)$$

where the operators  $\sigma_i^\pm$  create and annihilate an excitation of energy  $\epsilon_i$  at site  $i$ . The energies of individual pigment excited states  $\epsilon_i$  and the strengths of interaction between them  $V_{ij}$  are determined by the pigment structure and resulting charge distribution [45].

A comprehensive discussion of different photosynthetic pigment structures can be found in chapter 4 of ref. 4. Chromophores generally contain delocalized conjugated electron systems, typically aromatic rings. In *e.g.* chlorophyll (Chl), bacteriochlorophyll (BChl) and porphyrin pigments, these rings are arranged in a macrocyclic structure with four excited states labelled  $Q_x(S_1)$ ,  $Q_y(S_2)$ ,  $B_x$  and  $B_y$ . The  $Q_y$  transition has a large dipole strength which lies in the optical region and therefore dominates energy transfer. This transition corresponds to the dipole moment pointing between two rings of the macrocyclic system as in indicated in Fig. 1.1(a). Bilins are a class of pigment which have a linear structure, resembling a chlorophyll type structure which has been opened out. Examples include the allophycocyanin (APC) and C-phycocyanin (CPC) bilins found in cyanobacteria and the phycoerythrobilin (PEB) dihydrobiliverdin (DBV) bilins found in marine cryptophyte algae. There are also chain like light absorbing systems such as carotenoids and conjugated polymers. Light harvesting antennae often contain different types of chromophore, but even in homo-chromophoric complexes, interactions with the different local protein environments can distort the pigment structure and introduce a large degree of disorder in excited state energies  $\epsilon_i$ .

Doubly excited states are not accounted for within this model. Under natural illumination *in vivo*, absorption of a second photon within the time-scale of energy transfer and dissipation is improbable. However, non-linear spectroscopic experiments which probe energy transfer in biomolecules do populate doubly excited exciton states and these need to be correctly accounted for in a theoretical description of non-linear spectra.

There is a resonance Coulomb interaction between the charged, de-localized ex-

cited states of the chromophores given by [44]

$$V_{ij} = \frac{1}{4\pi\epsilon} \int d^3r_i d^3r_j \frac{n_{eg}^i(r_i) n_{ge}^j(r_j)}{|r_i - r_j|}, \quad (1.3)$$

where  $n_{eg}^i(r)$  denotes the transition charge density connecting ground and excited electronic states of molecule  $i$ . If inter-chromophore distances are large with respect to the spatial extent of transition densities, it is valid to keep the leading dipole-dipole interaction in a multipole expansion of the above which results in [44]

$$V_{ij}^{\text{dipole}} = C \frac{\hat{\mathbf{d}}_i \cdot \hat{\mathbf{d}}_j - 3(\hat{\mathbf{r}}_{ij} \cdot \hat{\mathbf{d}}_i)(\hat{\mathbf{r}}_{ij} \cdot \hat{\mathbf{d}}_j)}{|\mathbf{r}_{ij}|^3}, \quad (1.4)$$

where  $\hat{\mathbf{d}}_i$  denotes directions of the transition dipole moments and  $\mathbf{r}_{ij}$  the inter-chromophore distance vectors. The factor  $C$  accounts for the dipole strength as well as screening of the coupling due to the refractive index/electric permittivity of protein and solvent environment.

This ideal dipole approximation is not strictly valid if the spatial extent of transition charge densities is comparable with inter-chromophore distances. In this case numerical methods which are accurate to all orders can be employed. The transition density cubes (TDC) method [46] coarse-grains transition densities obtained from wavefunctions calculated within standard quantum chemistry packages (*e.g.* Gaussian) into finite volume elements and spatial integrals in (1.3) become a summation over TDC elements. For inter-chromophore distances  $< 1$  nm, there is an additional exchange type interaction arising from the overlap of wave functions. This decays exponentially with distances and is therefore often neglected for exciton energy transfer, but is important in the context of charge transfer [44].

These interactions mean that the electronic eigenstates  $|\alpha\rangle = \sigma_\alpha^+ |0\rangle = \sum_i C_i^\alpha |i\rangle$  (known as excitonic states), are linear combinations of the local excitations of chromophores. If electronic interactions are strong, excitonic states can be ‘delocalized’ meaning that many chromophores share the excitation.

**Bath Hamiltonian** The environment is modelled as a collection of quantized harmonic vibrational normal modes (phonons) with total Hamiltonian

$$H_B = \sum_{i,k} \left[ \frac{p_{i,k}^2}{2m_{i,k}} + \frac{1}{2} m_{i,k} \omega_{i,k}^2 q_{i,k}^2 \right] = \sum_{i,k} \omega_{i,k} \left( b_{i,k}^\dagger b_{i,k} + \frac{1}{2} \right), \quad (1.5)$$

where bosonic creation and annihilation operators  $[b_k, b_k^\dagger] = 1$ ,  $b_k^\dagger |0\rangle = |1_k\rangle$ . The oscillator coordinates are related by  $q_{i,k} = \sqrt{1/(2m_{i,k}\omega_{i,k})}(b_{i,k}^\dagger + b_{i,k})$  and  $p_{i,k} = i\sqrt{m_{i,k}\omega_{i,k}/2}(b_{i,k}^\dagger - b_{i,k})$ . The physical origin of these vibrational modes includes the motion of the protein and solvent, as well as the inter and intra-molecular vibrational motions of the chromophores themselves. The harmonicity of the vibrational motion is justified by the dominance of the leading expansion of potential energy surfaces (PES) for small displacements from an equilibrium position [47].

**System-bath Hamiltonian** The interaction of the vibrational modes with the excited electronic states of the chromophores is given by

$$H_{\text{SB}} = \sum_{i,k} g_{i,k} \sigma_i^+ \sigma_i^- \otimes (b_{i,k} + b_{i,k}^\dagger) = \sum_{i,k} g_{i,k} (\sigma_i^+ \sigma_i^- \otimes \sqrt{2m_{i,k}\omega_{i,k}} q_{i,k}) = \sum_{i,k} c_{i,k} (\sigma_i^+ \sigma_i^- \otimes q_{i,k}), \quad (1.6)$$

which describes the linear coupling of excited states of chromophores to vibrational coordinates and arises from an expansion of nuclear dependence of  $\epsilon_i(r)$  and keeping linear terms [47]. Off-diagonal couplings ( $\propto \sigma_i^+ \sigma_j^-$ ) are neglected. Molecular dynamics simulations of the types of systems studied in this thesis have shown that the influence of diagonal interactions are orders of magnitude larger than off-diagonal contributions [48]. This is generally true of excitation dynamics, however for the description of electron transfer dynamics off-diagonal interactions cannot be neglected [49–51].

This interaction in equation (1.6) describes potential energy surfaces which are displaced by  $d_{i,k} = \frac{c_{i,k}}{m_{i,k}\omega_{i,k}^2}$  in the electronic excited state. A counter term  $H_{\text{reorg}} = \sum_{i,k} \frac{c_{i,k}^2}{2m_{i,k}\omega_{i,k}^2} \sigma_i^+ \sigma_i^-$  is added to the total Hamiltonian to compensate for the renormalization of the potential which is induced by the coupling. This ensures that the only influence of the coupling term is to shift the potential energy surface in the excited state as shown in Fig. 1.1b. This term can be included as a shift in site energies of the system Hamiltonian  $\epsilon_i = \epsilon_i^0 + \lambda_i$ . This does not alter electronic dynamics when the local environments are identical.

### 1.1.2 Reduced system dynamics

The evolution of the reduced system  $\rho_S(t) = \text{Tr}_B [U(t, t_0) \rho(t_0)]$  can be expressed in terms of a dissipative propagator in Liouville space

$$\mathcal{U}(t, t_0) = \left\langle \overleftarrow{\mathcal{T}} \exp \left[ -i \int_0^t dt' \mathcal{L}_{\text{SB}}(t') \right] \right\rangle_B. \quad (1.7)$$

Assuming a seperable initial state  $\rho(t_i) = \rho_S(t_i) \otimes \rho_B(t_i)$ , the path integral representation  $\rho_S(t) = \mathcal{U}(t, t_0)\rho_S(t_i)$  becomes [44]

$$\rho_S(x^\pm, t) = \int dx_0^\pm \int \mathcal{D}x^\pm \exp \left\{ i(S_S[x^+] - S_S[x^-]) \right\} \mathcal{F}_{\text{FV}}[x^+, x^-] \rho_S(x_0^\pm, t_0), \quad (1.8)$$

where

$$\begin{aligned} \mathcal{F}^{\text{FV}}[x^+, x^-] &= \int dq_i^\pm dq \int \mathcal{D}q^\pm \rho_B(q_i^\pm, t) \\ &\quad \times \exp \left\{ i(S_B[q^+] - S_B[q^-]) \right\} \\ &\quad \times \exp \left\{ i(S_{\text{SB}}[x^+, q^+] - S_{\text{SB}}[x^-, q^-]) \right\}, \end{aligned} \quad (1.9)$$

is the Feynman-Vernon influence functional [52],  $S[r]$  is the classical action for path  $r(t)$  and the system and bath paths are subject to the boundary conditions  $x^\pm(t_i) = x_i$ ,  $x^\pm(t) = x$ ,  $q^\pm(t_i) = q_i$  and  $q^\pm(t) = q$ . In the above it is understood that bath paths  $q$  are a shorthand notation, for example  $\int dq$  means  $\prod_k \int dq_k$ . An interaction of the form  $H_{\text{SB}} = \sum_i Q_i \otimes B_i$  with linear bath operators  $B_i$ , yields path integrals which are Gaussian and the Feynman-Vernon influence functional can therefore be further evaluated resulting in

$$\mathcal{F}^{\text{FV}}[x^+, x^-] = \exp \left( - \sum_{ij} \int_{t_i}^t ds \int_{t_i}^t ds' \left\{ Q_i[x^+(s)] - Q_i[x^-(s)] \right\} \right) \quad (1.10)$$

$$\times \left\{ C_{ij}(s - s') Q_j[x^+(s')] - C_{ij}^*(s - s') Q_j[x^-(s')] \right\} \quad (1.11)$$

$$- i \sum_i \frac{\mu_i}{2} \int_{t_i}^t ds \left\{ Q_i^2[x^+(s)]^2 - Q_i^2[x^-(s)] \right\} \right). \quad (1.12)$$

Here  $C_{ij}(t) = \langle B_i(t) B_j(0) \rangle_B$  is the two time bath correlation function which fully specifies the influence of the bath. For the interaction (1.6), the corresponding counter term appears as  $\mu_i = 2\pi \sum \frac{g_{i,k}^2}{\omega_{i,k}}$  but cancels with path boundary conditions [43].

### 1.1.3 Bath correlation and spectral densities

As was demonstrated in the previous section, the influence of a bath of harmonic oscillators on the dynamics of a system with an interaction of the form  $H_I = \sum_i Q_i \otimes B_i$  is entirely determined by the two time correlation function of bath coupling operators  $C_{ij}(t) = \langle B_i(t) B_j(0) \rangle$ . In the present case we have  $B_i = \sum_k g_{i,k} (b_{i,k}^\dagger + b_{i,k})$ ,

and will assume that local environments are independent  $[b_{i,k}, b_{j,k'}^\dagger] = \delta_{ij}\delta_{k,k'}$  such that

$$\begin{aligned} C_{ij}(t) = C_i(t) &= \sum_k g_{i,k}^2 \left[ (1 + n(\omega_{i,k})) e^{-i\omega_{i,k}t} + n(\omega_{i,k}) e^{+i\omega_{i,k}t} \right] \\ &= \frac{1}{\pi} \int_0^\infty d\omega J_i(\omega) [\coth(\beta\omega/2) \cos(\omega t) - i \sin(\omega t)] , \end{aligned} \quad (1.13)$$

where  $n(\omega) = 1/(e^{\beta\omega} - 1)$  is the Bose-Einstein distribution for inverse temperature  $\beta = (K_B T)^{-1}$  and the function

$$J_i(\omega) = \pi \sum_k g_{i,k}^2 \delta(\omega - \omega_{i,k}) = \frac{\pi}{2} \sum_k \frac{c_{i,k}^2}{m_{i,k} \omega_{i,k}} \delta(\omega - \omega_{i,k}) \quad (1.14)$$

is known as the spectral density. Spectral densities defined in the literature can differ by factors of  $\pi$  or  $\omega^2$ , for this reason we emphasise the definition used throughout this thesis. Additionally it is common to extend the spectral density to negative frequencies  $J(-\omega) = -J(\omega)$ , so that for example  $C_i(t) = \frac{1}{\pi} \int_{-\infty}^\infty d\omega \frac{J_i(\omega) e^{-i\omega t}}{1 - e^{-\beta\omega}}$ , which takes the form of the fluctuation-dissipation theorem and  $J_i(\omega)$  is identified as the imaginary part of the response function [43, 53].

The quantity  $\lambda_i = \sum_k \frac{g_{i,k}^2}{\omega_{i,k}} = \pi^{-1} \int_0^\infty d\omega J_i(\omega)/\omega$  is known as the reorganisation energy and characterizes the strength of system-bath interactions. It represents the energy the bath must dissipate in order to relax to the new equilibrium position in the excited state. This is described by the counter term  $H^{\text{reorg}}$  defined in section 1.1.1 and is related to the Stokes shift observed between absorption and fluorescence spectra of a monomer [44].

The functional form of the spectral density depends on the system-bath interactions in the system under consideration. In the light harvesting systems studied in this thesis, there is a structureless continuous component which rises rapidly at low frequencies and is damped by a cut off function at high frequencies. This component generally arises from interactions with the damped motion of protein and solvent degrees of freedom [54]. Additionally, specific under-damped vibrational modes can interact strongly with the excited states of chromophores resulting in numerous narrow peaks in the spectral density. These peaks are generally a manifestation of strong coupling to harmonic intra-molecular motions of chromophores, the frequencies and coupling strengths of which can be determined from low temperature fluorescence line-narrowing experiments [55–58]. Different functional forms for the spectral density have been successfully applied in theoretical modelling of spectroscopic measurements. Renger and Marcus [59] reproduced low temperature fluorescence line



narrowing measurements of the B777 complex - a single chromophore-protein subunit isolated from a larger system. Various spectra of the seven chromophore FMO complex were calculated in the seminal work of Adolphs and Renger [60]. Information from mixed quantum-classical molecular dynamics simulations may also be used to construct spectral densities and can elucidate the physical origin of peaks appearing in spectral densities. This type of approach has also recently indicated that in systems containing different types of chromophore, or where some chromophores are more exposed to the solvent than others, the local environments can have significant differences which may impact electronic dynamics [40, 61–63].

The precise functional form of continuous component is difficult to determine and is subject of debate [64]. The exponent of the algebraic growth of the spectral density at small frequency results in qualitative differences in electronic dynamics [43, 65]. In particular, within Redfield theory (see section 1.2.1) the rate of pure dephasing vanishes for super-ohmic forms ( $J(\omega) \propto \omega^s$  with  $s > 1$ ). This has been proposed as a mechanism for prolonging the beating of inter-exciton coherences [66] however it has also been highlighted [67] that this arises from the Markovian approximation made within this model.

In this thesis we assume that local environments are identical, uncorrelated and may be characterized by  $J(\omega) = J_D(\omega) + \sum_q J_{BO}^q(\omega)$  where

$$J_D(\omega) = \theta(\omega) 2\lambda_D \Omega_c \frac{\omega}{\omega^2 + \Omega_c^2} \quad (1.15)$$

and

$$J_{BO}^q(\omega) = \theta(\omega) 2\lambda_q \omega_q^2 \gamma_q \frac{\omega}{(\omega^2 - \omega_q^2)^2 + \gamma_q^2 \omega^2} . \quad (1.16)$$

The Heaviside step function  $\theta(\omega)$  appears as a reminder that  $J(\omega) = 0$  for negative frequencies, unless the extension  $J(-\omega) = -J(\omega)$  is has been made for mathematical convenience. The Drude–Lorentz component  $J_D(\omega)$  is the over-damped limit ( $\gamma_q \gg \omega_q$ ) of the Brownian oscillator model with  $\Omega_c = \omega_q^2/\gamma_q$ . The corresponding correlation functions can be obtained by evaluating (1.1.3) via contour integration yielding a series representation of the form  $C(t) = \sum_k c_k e^{-\nu_k t}$ . For an under-damped Brownian oscillator this reads [68]

$$C^{BO}(t) = c_+^{BO} e^{-\nu^+ t} + c_-^{BO} e^{-\nu^- t} + \sum_{k=1}^{\infty} c_k^{BO} e^{-\nu_k t} , \quad (1.17)$$

with  $c_{\pm}^{BO} = \pm i \lambda_q \frac{\omega_q^2}{2\zeta_u} [\cot(\nu^{\pm} \beta/2) - i]$ ,  $c_k^{BO} = -\frac{4\lambda_q \gamma_q \omega_q^2}{\beta} \frac{\nu_k}{(\omega_q^2 + \nu_k^2)^2 - \gamma_q^2 \nu_k^2}$ ,  $\nu^{\pm} = \gamma_q/2 \pm i\zeta_q$ ,

Matsubara frequencies  $\nu_k = 2\pi k/\beta$  and shifted frequency  $\zeta_q = \sqrt{\omega_q^2 - \gamma_q^2/4}$ . In the over-damped limit ( $\gamma_q \gg 2\omega_q$ ) this reduces to the Drude form  $C^D(t) = c_0^D e^{-\Omega_D t} + \sum_{k=1}^{\infty} c_k^D e^{-\nu_k t}$  with  $c_0^D = \lambda\Omega_c [\cot(\beta\Omega_c/2) - i]$ ,  $c_k^D = \frac{4\lambda\Omega_c}{\beta} \frac{\nu_k}{\nu_k^2 - \Omega_c^2}$  and cut off frequency  $\Omega_c = \omega_q^2/\gamma_q$ .

The Matsubara summation can usually be truncated to some finite number of terms  $K$ , in particular at high temperatures it may be valid to retain only the first term in the expansion. At low temperatures where many Matsubara terms are required, the partial fraction decomposition schemes [69] is more efficient.

## 1.2 Perturbative approaches to quantum dynamics

### 1.2.1 Redfield theory

Redfield theory [44, 70, 71] describes the quantum coherent dynamics which result when the strength of the coupling to the environment is weak with respect to the electronic coupling ( $V \gg \lambda$ ). A second order Markovian master equation for populations and coherences of the reduced system density matrix is derived for a system-bath coupling of the general form  $H_{SB} = \sum_i Q_i \otimes B_i$ . For the case in hand,  $Q_i = \sigma_i^+ \sigma_i^-$  and  $B_i = \sum_k g_{ik} (b_{ik}^\dagger + b_{ik})$ . It is also necessary to assume that the states of the system  $\rho_S$  and bath  $\rho_B$  are initially uncorrelated *i.e.* that the total system is in the separable state  $\rho_S \otimes \rho_B$ . The resulting master equation for the reduced system density matrix is given in the basis of system energy eigenstates  $|\alpha\rangle, |\beta\rangle$  as

$$\dot{\rho}_{\alpha\beta}(t) = -i\omega_{\alpha\beta}\rho_{\alpha\beta}(t) - \sum_{\gamma,\delta} R_{\alpha\beta,\gamma\delta}(t)\rho_{\gamma\delta}(t), \quad (1.18)$$

where  $\omega_{\alpha\beta}$  is the difference in energies of the states  $|\alpha\rangle$  and  $|\beta\rangle$  and the Redfield tensor is given by

$$R_{\alpha\beta,\gamma\delta}(t) = \sum_{\epsilon} \left( \delta_{\delta\beta} \Gamma_{\alpha\epsilon,\epsilon\gamma}(\omega_{\gamma\epsilon}) + \delta_{\alpha\gamma} \Gamma_{\beta\epsilon,\epsilon\delta}^*(\omega_{\delta\epsilon}) \right) - (\Gamma_{\delta\beta,\alpha\gamma}(\omega_{\gamma\alpha}) + \Gamma_{\gamma\alpha,\beta\delta}^*(\omega_{\delta\beta})), \quad (1.19)$$

with

$$\Gamma_{\alpha\beta,\delta\gamma}(\omega, t) = \sum_{i,j} \langle \alpha | Q_i | \beta \rangle \langle \gamma | Q_j | \delta \rangle \int_0^t dt e^{i\omega t} C_{ij}(t). \quad (1.20)$$

Often, as part of a Markovian approximation, the integration limit in (1.20) is extended  $t \rightarrow \infty$  making the tensor time independent and therefore expediting the

integration of (1.18). In this case

$$\Gamma_{\alpha\beta,\delta\gamma}(\omega) = \sum_{i,j} Q_{\alpha\beta}^i Q_{\gamma\delta}^j \tilde{C}_{ij}(\omega) , \quad (1.21)$$

with  $Q_{\alpha\beta}^i = \langle \alpha | Q_i | \beta \rangle$  and where  $\tilde{C}_{ij}(\omega)$  denotes the half-sided Fourier (Fourier-Laplace) transform of the bath correlation function. Its real and imaginary parts can be expressed directly in terms of the spectral density of the environment as

$$\tilde{C}_{ij}^{(\Re)}(\omega) = (n(\omega) + 1) [J_{ij}(\omega) - J_{ij}(-\omega)] , \quad (1.22)$$

and

$$\tilde{C}_{ij}^{(\Im)}(\omega) = \frac{1}{\pi} \mathcal{P} \int_{-\infty}^{\infty} d\omega' \frac{\tilde{C}_{ij}^{(\Re)}(\omega')}{\omega - \omega'} \quad (1.23)$$

respectively, where  $\mathcal{P}$  denotes the principal part integral. In (1.22) the fact that  $n(-\omega) = -(n(\omega) + 1)$  is exploited. The imaginary parts of this correlation function are often neglected, with the rationale that they only alter the transition frequencies (Lamb shifts) and therefore do not affect the dynamics. However it has been pointed out [72] that notable differences in dynamics can be observed if imaginary parts are included. Transfer rates between excitons are given by  $R_{\alpha\alpha\beta\beta} = 2 \sum_i |C_i^\alpha|^2 |C_i^\beta|^2 \tilde{C}_i^{(\Re)}(\omega_{\alpha\beta})$ , which illustrates that a (spatial) overlap of exciton states is required for rapid transfer. The pure dephasing rate  $R_{\alpha\alpha,\alpha\alpha} = 2 \sum_i |C_i^\alpha|^4 \lim_{\omega \rightarrow 0} \tilde{C}_i^{(\Re)}(\omega)$  is dependent on the extent of exciton delocalization and the slope of the spectral density as  $\omega \rightarrow 0$ .

If Redfield theory is applied to systems where the parameters do not merit a perturbative expansion, the theory can predict negative or diverging populations. The so-called secular approximation brings this master equation into Lindblad form ensuring complete positivity which allows for extrapolation outside the regime of validity of the theory without unphysical results. This is achieved by neglecting elements of the tensor  $R_{\alpha\beta\gamma\delta}$  which satisfy  $|\omega_{\alpha\beta} - \omega_{\delta\gamma}| \neq 0$  since these oscillatory terms do not contribute upon integration of the equations of motion. This has the effect of decoupling the evolution of populations and coherences reducing the computational complexity of the problem.

A modified version of Redfield theory [73–75] separates the system-bath interaction into diagonal and off-diagonal parts in the system eigenbasis,

$$H_{\text{SB}} = \left( \sum_{\alpha} |\alpha\rangle \langle \alpha| \otimes \sum_i Q_{\alpha\beta}^i B_i \right) + \left( \sum_{\alpha, \beta \neq \alpha} |\alpha\rangle \langle \beta| \otimes \sum_i Q_{\alpha\beta}^i B_i \right) \quad (1.24)$$

and treats only the off-diagonal coupling perturbatively. To second order this approach yields population transfer rates between eigenstates given by

$$\begin{aligned}
 k_{\alpha\beta}^{\text{MR}} = & 2\Re \int_0^\infty dt \exp(-i\omega_{\alpha\beta}t - i(\lambda_{\alpha\alpha,\alpha\alpha} + \lambda_{\beta\beta,\beta\beta})t - g_{\alpha\alpha,\alpha\alpha}(t) - g_{\beta\beta,\beta\beta}(t)) \\
 & \times \exp(2g_{\beta\beta,\alpha\alpha}(t) + 2i\lambda_{\beta\beta,\alpha\alpha}) \\
 & \times \left[ \ddot{g}_{\beta\alpha,\beta\alpha}(t) - (\dot{g}_{\beta\alpha,\beta\beta}(t) - \dot{g}_{\beta\alpha,\alpha\alpha}(t) + 2i\lambda_{\beta\alpha,\beta\beta})^2 \right], \quad (1.25)
 \end{aligned}$$

where  $g_{\alpha\beta,\gamma\delta}(t) = \sum_i Q_{\alpha\beta}^i Q_{\gamma\delta}^i g_i(t)$ ,  $g_i(t) = \int_0^t ds \int_0^s ds' C_i(s')$  and  $\lambda_{\alpha\beta,\gamma\delta} = \sum_i Q_{\alpha\beta}^i Q_{\gamma\delta}^i \lambda_i$ . Modified Redfield theory (MRT) predicts exciton transfer rates only. This deficiency of this theory is being addressed via the development of a ‘coherent modified Redfield theory’ (CMRT) which describes the dynamics of both populations and coherences in the exciton basis [76].

### 1.2.2 Förster theory

Förster theory [5, 6] predicts the incoherent hopping of excitation energy between two sites  $a$  and  $b$ . Conversely to Redfield theory, it derives from second order perturbative expansion in the electronic coupling  $V_{ab}$  which is assumed to be weak with respect to environmental coupling ( $V \ll \lambda$ ). By assuming that the environments local to each site are independent and in thermal equilibrium, a Fermi golden rule type expression is obtained which includes a summation over the thermally weighted initial and final states of the donor and acceptor environments. This expression can then be recast in terms of the correlation function of the perturbation in the interaction picture:

$$k_{ab} = 2\pi \sum_{i,f} \frac{e^{-\beta E_i}}{\sum_k e^{-\beta E_k}} |\langle i|V|f \rangle|^2 \delta(E_i - E_f) = 2\Re \int_0^\infty dt \langle V_{ab}(t)V_{ba}(0) \rangle_{\text{B}}. \quad (1.26)$$

For the present case of bosonic baths this correlation function can be evaluated by utilizing a canonical transformation to the polaron frame [47] yielding the expression in terms of the overlap of the absorption and fluorescence lineshapes of the individual sites,

$$k_{ab}^{\text{F}} = \frac{|V_{ab}|^2}{2\pi} \int_{-\infty}^\infty d\omega \bar{D}_a(\omega) D_b(\omega). \quad (1.27)$$

Expressions for these lineshapes are given in Chapter 5, equations (5.4) and (5.5).

If electronic couplings are reliably calculated within the point dipole-dipole approximation, the transfer rate between sites separated by  $r$  decays as  $r^{-6}$ . This is a key aspect of Förster theory and is used as a measure of distances [77].

Given transfer rates between every site of a complex, the dynamics of the site populations  $P_m$  can be described as incoherent hopping via the Pauli master equation,

$$\frac{dP_a}{dt} = \sum_b [W_{ab}P_a(t) - W_{ba}P_b(t)] . \quad (1.28)$$

## 1.3 Interpolating approaches to quantum dynamics

Biomolecular systems often feature electronic couplings which are of the same order as the system-bath coupling strengths. In this case a theory is needed which is valid for the regime between the Förster and Redfield limits of weak electronic and weak system-bath coupling strengths respectively. Furthermore coupling strengths may vary considerably within the same complex, therefore requiring a theory which encapsulates both the Förster and Redfield limits whilst accurately interpolating between them.

### 1.3.1 Hierarchical expansion of dynamics

The hierarchical equations of motion (HEOM) technique [78–80] is a popular non-perturbative method which can yield accurate reduced system dynamics for arbitrary system-bath coupling strength. A decomposition of the bath correlation function into an exponential series  $C_j(t) = \sum_k^K c_{jk} e^{-\nu_{jk}t}$ , enables the derivative of the influence function (1.12) (which is required to solve  $\rho_S(t) = \mathcal{U}(t, t_i)\rho_S(t_i)$ ) to be expressed somewhat compactly in terms of auxiliary influence functionals given by

$$\begin{aligned} \mathcal{F}_n^{\text{FV}}[x^+, x^-] &= \prod_{jk} \left[ (-i) \int_{t_i}^t ds' \left\{ C_j(s-s') Q_j[x^+(s')] - C_j^*(s-s') Q_j[x^-(s')] \right\} \right]^{n_{jk}} \\ &\times \mathcal{F}^{\text{FV}}[x^+, x^-] , \end{aligned} \quad (1.29)$$

corresponding auxiliary operators defined by

$$\partial_t \rho_n(t) = -i[H_S, \rho_n(t)] + \int \mathcal{D}x^\pm e^{iS[x^\pm]} \partial_t \mathcal{F}_n^{\text{FV}}[x^+, x^-] e^{-iS[x^-]} , \quad (1.30)$$

and  $\mathbf{n}$  denotes the multi-index  $\{\{n_{10}, n_{11}, \dots, n_{1K}\}, \dots, \{n_{N0}, n_{N1}, \dots, n_{NK}\}\}$ . By definition the auxiliary operator  $\rho_0(t)$  with multi-index elements  $n_{jk} = 0$ , for all  $j, k$  corresponds to the reduced system density matrix. For all  $\nu_{jk} \in \mathbb{R}_{>0}$  this defines a

hierarchy of coupled differential equations of the form

$$\begin{aligned} \partial_t \rho_{\mathbf{n}}(t) = & -i[H_S(t), \rho_{\mathbf{n}}(t)] - \sum_j^N \sum_k^K n_{jk} v_{jk} \rho_{\mathbf{n}}(t) \\ & - i \sum_j^N \left[ Q_j, \sum_k^K \rho_{\mathbf{n}_{jk}^+}(t) \right] - i \sum_j^N \sum_k^K n_{jk} \left( c_{jk} Q_j \rho_{\mathbf{n}_{jk}^-}(t) - c_{jk}^* \rho_{\mathbf{n}_{jk}^-}(t) Q_j \right), \end{aligned} \quad (1.31)$$

where  $\mathbf{n}_{jk}^\pm$  refers to the multi-index with element  $n_{jk}$  changed to  $n_{jk} \pm 1$ . Equations where multi-index elements  $\sum_{jk} n_{jk} = n$  are referred to as belonging to the  $n$ -th tier of the hierarchy and describe effects up to at least  $2n$ -th order in system-bath coupling. Formally the hierarchy extends to infinity, however for numerical treatment equations up to a maximum of tier  $N_{\text{trunc}}$  are included. Substituting delta functions for terms  $\propto C(s - s')$  in the equations for tiers above  $N_{\text{trunc}}$  invokes a Markovian approximation for their propagation which can then be accounted for with a single ‘temperature correction’ term added to the evolution of every auxiliary operator in the tiers below  $N_{\text{trunc}}$  [81]. The equations in (1.31) can be rescaled by a redefinition of auxiliary influence functional or corresponding auxiliary operators [80]. The rescaling  $\tilde{\rho}_{\mathbf{n}}(t) = \left( \prod_{jk} n_{jk}! \sqrt{|c_{jk} c_{jk}^*|} \right)^{-1/2} \rho_{\mathbf{n}}(t)$  results in the equations

$$\begin{aligned} \partial_t \tilde{\rho}_{\mathbf{n}}(t) = & -i[H_S(t), \tilde{\rho}_{\mathbf{n}}(t)] - \sum_{jk} n_{jk} v_{jk} \tilde{\rho}_{\mathbf{n}}(t) \\ & - \sum_j \left( \sum_{k=1}^{\infty} \frac{c_{jk}}{\nu_{jk}} - \sum_{k=1}^K \frac{c_{jk}}{\nu_{jk}} \right) [Q_j, [Q_j, \tilde{\rho}_{\mathbf{n}}(t)]] \\ & - i \sum_{jk} \sqrt{(n_{jk} + 1) |c_{jk} c_{jk}^*|} \left[ Q_j, \tilde{\rho}_{\mathbf{n}_{jk}^+}(t) \right] \\ & - i \sum_{jk} \sqrt{n_{jk} / |c_{jk} c_{jk}^*|} \left( c_{jk} Q_j \tilde{\rho}_{\mathbf{n}_{jk}^-}(t) - c_{jk}^* \tilde{\rho}_{\mathbf{n}_{jk}^-}(t) Q_j \right). \end{aligned} \quad (1.32)$$

which are now extended to the case of complex  $\nu_{jk}$  appearing in complex-conjugate pairs in  $C_j(t)$ . Here  $c_{i\bar{k}}$  labels the coefficient of the corresponding term with complex-conjugate exponent. This enables the treatment of a correlation function composed of both  $C^{\text{BO}}(t)$  and  $C^{\text{D}}(t)$  forms, namely if  $c_k = c_{\pm}^{\text{BO}}$ , then  $c_{\bar{k}} = c_{\mp}^{\text{BO}}$  and  $c_k^{\text{D}} = c_k^{\text{D}}$ . The scaling ensures that the magnitude of auxiliary operators decays to zero for high hierarchical orders. This enables the system of equations to be propagated with an adaptive time-step algorithm which expedites calculations and may also reduce the tier at which the hierarchy can be truncated for results to particular level of conver-

gence [82]. Additional speed-up can be achieved with parallelization by assigning the propagation of groups of auxiliary operators to available processors. This partitioning must be done so as to minimize communication costs after each time-step [83]. The large number of processors available on modern graphics processing units has allowed calculations to be accelerated by factors of up to  $\times 458$  [84]. It should be noted that the number of auxiliary operators contained within a hierarchy truncated at tier  $\mathcal{N}$ , for an  $N$ -site system with Matsubara series truncated at the  $K$ -th term is given by  $\frac{(\mathcal{N}+N(K+1))!}{\mathcal{N}!(N(K+1))!}$  and that therefore computational and memory requirements scale drastically with increasing system size.

### 1.3.2 Other approaches

The model of Haken and Strobl [85] phenomenologically captures the transition from coherent to incoherent system dynamics. The dynamics of the environment are assumed to be infinitely fast (Markovian) and modelled as a classical noise process which induces Gaussian fluctuations of site energies. In the infinite temperature limit this corresponds to pure dephasing in the site basis as described by  $\dot{\rho}_{ab}(t) = \sum_{cd} \{-i(H_{ac}\delta_{db} - \delta_{ca}H_{bd}) - \gamma(1 - \delta_{ab})\delta_{ca}\delta_{db}\} \rho_{cd}$  which can be solved exactly and predicts the exponential decay of initial system coherences. Note that due to the infinite temperature assumption this model incorrectly results in equally populated final states.

Polaron representation master equations [86, 87] represent a modified perturbative approach which can quantitatively capture the transition from coherent to incoherent dynamics. Since they are perturbative with respect to a redefined system-environment interaction in the polaron frame, the corresponding lab frame dynamics can be accurate where conventional perturbative approaches fail. Importantly the theory is also accurate in the Förster and Redfield limits. More recently a related variational approach which attempts to use an optimal amount of polaron transformation has been applied to energy transfer [88].

The influence of an environment of independent oscillators which interacts linearly with a system has alternative representations [89, 90]. Given an arbitrary spectral density, it is possible to construct one-dimensional chains of interacting oscillators (effective modes) which describe the same system dynamics [91–95]. These effective mode chain representations have been used in conjunction with the multi-configurational time-dependent Hartree approach (MCTDH) [96] to describe excited state dynamics at conical intersections [92]. The theory of orthogonal polynomials has provided an exact mapping [94] to these chain systems and due to short range

interactions, the transformed problem is amenable to efficient simulation [93] with the time dependent density matrix renormalization group (t-DMRG) technique [97]. This numerical method has been well developed and is widely used for example in the study of spin chain dynamics [98]. The application of this approach has been dubbed the Time Evolving Density with Orthogonal Polynomial Algorithm (TEDOPA) and has been successfully applied in biological systems at room temperatures [67].

The iterative quasi-adiabatic propagator path integral (QUAPI) scheme [99–101] is numerically exact, but the computational effort scales very unfavourable with system size. This is a general characteristic of non-perturbative techniques.

## 1.4 Quantum traits in electronic and vibrational dynamics

### 1.4.1 Quantum coherence

Since the Schrödinger equation has the form of a wave equation, physical solutions obey the superposition principle. The density matrix description of the coherent superposition such as  $|\psi\rangle = a|\phi_1\rangle + b|\phi_2\rangle$ , has off-diagonal elements  $a^*b$  in the  $\{|\phi_1\rangle, |\phi_2\rangle\}$  basis. These terms are referred to as quantum coherences and the fixed phase relation between elements of superpositions like this is at the root of quantum interference effects (quantum beats).

The interaction of an open system with its environment causes these phases be destroyed as the environment ‘measures’ the state of the system. The process by which this information is lost (becomes inaccessible correlations between system and environment) is known as decoherence. The process of decoherence causes the decay of off-diagonal density matrix elements causing the state to become diagonal a basis determined by the interaction with the environment. Thus, once all accessible quantum correlations in a state have been destroyed by interaction with an environment, a state can be described as a classical statistical mixture.

In a noisy environment such as that of a biomolecular system at room temperatures, quantum coherences would be expected to decay rapidly. Nevertheless, laser induced coherences can persist on the timescale of energy transfer events. The initial observation of long-lived quantum coherences in the Fenna-Matthews-Olsen (FMO) complex led to speculation that coherences are utilized in a quantum search algorithm for the most efficient path to an exit site [10]. No such mechanism has yet to be substantiated, but this conjecture triggered a fascination with the role of quan-



tum coherence in photosynthetic systems and has inspired the design of ‘biomimetic’ devices which claim to utilize coherence [102–104]. Quantum process tomography [105] of dynamics in light harvesting systems has been proposed [106] and performed in nanotubular aggregates [107]. This approach allows a more stringent assessment of the coherence in the evolution than the direct interpretation of spectroscopic signals. The introduction of ref. 108 outlines the current status of assessing coherence in a particular physical evolution. It should be noted that relevance *in-vivo*, of the experimentally observed long-lived quantum coherences is a matter of some strong debate [109–111]. Quantum coherence is also intimately related to entanglement, a quintessentially quantum phenomena. Numerous studies have quantified coherence in biomolecular systems using the concept of entanglement [112–115].

### 1.4.2 Exciton delocalization

The clustering of chromophores observed in light harvesting systems means that the resulting electronic coupling leads to delocalized (excitonic) states  $|\alpha\rangle = \sum_i C_i^\alpha |i\rangle$ . The extent of delocalization can be characterized by many measures [116–118], and is a crucial quantity in determining energy transfer dynamics. The participation [119]  $\text{PR}_\alpha = \sum_i |C_i^\alpha|^4$ , is a quantity often used to indicate of the number of chromophores which participate in a given excitonic state and its inverse is considered a measure of ‘delocalization length’. If a state  $|\alpha\rangle = \sum_i^N C_i^\alpha |i\rangle$  is completely delocalized,  $C_i^\alpha = 1/\sqrt{N}$  and therefore  $(\text{PR}_\alpha)^{-1} = N$ . For an exciton entirely localized on one chromophore  $|\alpha\rangle = |i\rangle$  and therefore  $(\text{PR}_\alpha)^{-1} = 1$ .

For weak interactions with an environment, the reduced system dynamics are closer to the regime of fully coherent dynamics. Within Redfield and modified Redfield theories, the influence of delocalization appears explicitly, wherein the participation ratio determines that exciton states which shared more chromophores experience a reduced rate of pure dephasing. When interaction with the environment is strong, such as within the limits of Förster theory, dynamics can be described as an incoherent hopping between localized states of the chromophores and thus delocalization plays no role. Between these limits an initially delocalized excitation undergoes a process of dynamical localization which can be captured within the hierarchical expansion of reduced system dynamics.

### 1.4.3 Quasiprobabilities

The field of quantum optics has developed a solid framework to quantify the quantum properties of bosonic fields [120]. It therefore provides excellent conceptual and quantitative tools to investigate non-classicality of harmonic vibrational degrees of freedom.

From the perspective of quantum optics, quantum behaviour with no classical counterpart, *i.e.* non-classicality, arises if the state of the system of interest cannot be expressed as a statistical mixture of coherent states defining a valid probability measure [121]. This then leads to non-positive values of  $s$ -parametrised phase-space quasiprobability distributions [122]

$$W(\alpha, s) = \frac{1}{\pi^2} \int_{-\infty}^{\infty} d^2\xi \chi(\xi, s) e^{\alpha\xi^* - \alpha^*\xi}, \quad (1.33)$$

defined as the Fourier transform of  $s$ -ordered characteristic functions  $\chi(\xi, s) = \text{Tr} \left[ \rho e^{\xi^* b^\dagger - \xi b} e^{s|\xi|^2/2} \right]$  of the bosonic quantum state. The characteristic function  $\chi(\xi, s)$  generates expectation values of  $s$ -ordered combinations of  $b^\dagger$  and  $b$  through

$$\langle b^{\dagger m} b^n \rangle_s = \left. \frac{\partial^m}{\partial^m \xi} \frac{\partial^n}{\partial^n \xi^*} \chi(\xi, s) \right|_{\xi=0}. \quad (1.34)$$

Normal order is given by  $s = 1$ , anti-normal order by  $s = -1$  and  $s = 0$  results in symmetrized expectation values. These quasiprobability distributions are in general not well behaved like classical probability distributions, for example they may take negative values or be highly singular (more so than a delta function). Special cases  $s = 1$  corresponds to the Glauber-Sudarshan  $P$ -representation,  $s = 0$  the Wigner representation and  $s = -1$  the Husimi  $Q$ -representation. Of this family, only the  $P$ -representation displays negative or highly singular regions for *every* non-classical state. The  $Q$ -representation is always positive while the Wigner distribution can be positive for non-classical states (*e.g.* a squeezed state).

However, highly singular behaviour of  $W(\alpha, 1) = P(\alpha)$  can make its characterisation challenging both theoretically and experimentally. To overcome this, a verification of the non-classicality of a quantum state can be achieved by constructing a regularised distribution [123, 124]

$$P_w(\alpha) = \frac{1}{\pi^2} \int d^2\xi \chi(\xi) \Omega_w(\xi) e^{\alpha\xi^* - \alpha^*\xi}. \quad (1.35)$$

A filter  $\Omega_w(\xi)$  is applied to the quantum characteristic function which satisfies the

following three conditions

**C1**  $\Omega_w(\xi)e^{|\xi|^2/2}$  is integrable for all positive  $w$ .

**C2**  $\Omega_w(\xi)$  has non-negative Fourier transform.

**C3**  $\Omega_w(0) = 1$  and  $\lim_{w \rightarrow \infty} = 1$  for all  $\xi$ .

Negativities in the resulting regularised distribution for a particular filter width  $w$  are a necessary and sufficient condition of quantum behaviour with no classical analogue [123]. The filter  $\Omega_s(\xi) = e^{(s-1)|\xi|^2/2}$  recovers the  $s$ -parametrised quasiprobabilities of equation (1.33) but for  $s \geq 1$  condition **C1** is not satisfied. Hence quasiprobability distributions with  $s > 0$  can be positive for non-classical states. Sampling  $\chi(\xi)$  only in a region  $|\xi| < w/2$  is equivalent to applying a rectangular non-classicality filter  $\Omega_w(\xi) = \text{rect}(\xi/w)$  with  $\text{rect}(x) = 1$  for  $|x| < 1$  and  $\text{rect}(x) = 0$  elsewhere. The Fourier transform of the rectangular function is sinc function which demonstrates that this filter violates condition **C2**. Within this thesis, we employ a simple a two-dimensional triangular filter,  $\Omega_w(\xi' + i\xi'') = \text{tri}(\xi'/w)\text{tri}(\xi''/w)$  with  $\text{tri}(x) = 1 - |x|$  for  $|x| < 1$  and  $\text{tri}(x) = 0$  otherwise. If the state  $\rho$  is expanded in the Fock basis up to level  $M$ , the filtered quasi-probability can be calculated from

$$P_w(\alpha) = \frac{1}{\pi^2} \sum_{m,n}^M \rho_{mn} \left( \int \int d\xi_r d\xi_i D_{nm}(\xi) e^{|\xi|^2/2} \Omega_w(\xi) e^{-2i(\alpha_r \xi_i - \alpha_i \xi_r)} \right) \quad (1.36)$$

where  $\rho_{mn} = \langle m | \rho | n \rangle$ , the integrals can be efficiently computed by discrete Fourier transform and elements of the displacement operator in the Fock basis  $D_{nm}(\xi) = \langle n | e^{\xi b^\dagger - \xi^* b} | m \rangle$  are given by

$$D_{mn}(\alpha) = \begin{cases} \sqrt{\frac{n!}{m!}} (\alpha)^{m-n} e^{-|\alpha|^2/2} L_n^{m-n}(|\alpha|^2) & m \geq n \\ \sqrt{\frac{m!}{n!}} (-\alpha^*)^{n-m} e^{-|\alpha|^2/2} L_m^{n-m}(|\alpha|^2) & n \geq m \end{cases}, \quad (1.37)$$

where  $L_n^m(x)$  are the generalized Laguerre polynomials.

#### 1.4.4 Non-classical statistics

Signatures of non-classicality can be observed in the fluctuations of the bosonic field. For a single-mode, negative values of the Mandel's  $Q$ -parameter [125] are a signature of non-classical behaviour and guarantee a non-positive P-representation. The Mandel  $Q$ -parameter characterises the departure of the occupation number

distribution  $P_n = \text{Tr} [|n\rangle \langle n| \rho]$  from Poissonian statistics through the inequality

$$Q = \frac{\langle n^2 \rangle - \langle n \rangle^2}{\langle n \rangle} - 1 < 0 \quad (1.38)$$

where  $\langle n^m \rangle$  denotes the  $m$ -th moment of the bosonic number operator  $n$ . Vanishing  $Q$  indicates Poissonian number statistics where the mean of  $n$  equals its variance, as is characteristic of classical wave-like behaviour *i.e.* a coherent state of light. For a chaotic thermal state one finds that  $Q = \langle n \rangle > 0$  indicating that particles are ‘bunched’. A Fock state is characterised by  $Q < 0$  indicating that particle occupation is restricted to a particular level.

Characterising the full phonon number distribution function  $P_n$  is not necessary to verify the non-classicality of vibrational modes. Inequalities involving occupation probabilities of nearest number states can similarly witness non-classical occupation fluctuations [126]. Modulations of adjacent phonon number occupation as quantified by negative  $B_n = (n+1)P_{n-1}P_{n+1} - nP_n^2$ , a criteria introduced by Klyshko [126], also guarantees negative regions of a quasi-probability distribution and is a potentially an experimentally accessible quantity.

## Chapter 2

# Non-classicality of molecular vibrations

*Advancing the debate on quantum effects in light-initiated reactions in biology requires clear identification of non-classical features that these processes can exhibit and utilise. Here it is shown that in prototype dimers present in a variety of photosynthetic antennae, efficient vibration-assisted energy transfer in the subpicosecond timescale and at room temperature can manifest and benefit from non-classical fluctuations of collective pigment motions. Non-classicality of initially thermalised vibrations is induced via coherent exciton-vibration interactions and is unambiguously indicated by negativities in the phase-space quasi-probability distribution of the effective collective mode coupled to the electronic dynamics. These quantum effects can be prompted upon incoherent input of excitation. The results therefore suggest that investigation of the non-classical properties of vibrational motions assisting excitation and charge transport, photoreception and chemical sensing processes could be a touchstone for revealing a role for non-trivial quantum phenomena in biology.*

The experimental demonstration of oscillatory electronic dynamics in light-harvesting complexes [10, 12–15] has triggered wide-spread interest in uncovering quantum phenomena that may impact the function of the molecular components of living organisms. In general, however, oscillatory patterns in dynamics is not sufficient argument to rule out classical descriptions of the same behaviour. Indeed, recent works have discussed how classical coherence models can predict electronic coherence beating [127, 128]. Therefore, an important challenge for the growing field of quantum effects in biomolecules is to clearly identify which quantum features with

no classical counterpart may manifest in these systems and how they may influence the process of interest.

The question of non-classicality of the dynamics of electronic excitations in light-harvesting systems has been addressed by investigating Leggett-Garg inequalities [129]. This work concludes that, under Markovian evolution, temporal correlations of individual pigments observables should violate classical bounds, and in consequence certain classical theories are unsuitable to describe electronic dynamics. Other works have investigated the quantumness of the electronic degrees of freedom [112–115, 130]. Despite these efforts, it is still far from understood which non-classical phenomena are directly correlated with efficient energy distribution in a prototype light-harvesting system.

What is clear is that exciton energy transport depends not only on the topology of electronic couplings among pigments but is critically determined by exciton-phonon interactions: molecular motions [45] and environmental fluctuations [45, 131, 132] drive efficient transport processes in light-harvesting antennae. In fact, it is well known that exciton-phonon interactions in these complexes have a rich structure as a function of energy and generally include coupling to both continuous and discrete modes associated to low-energy solvated protein fluctuations and under-damped intramolecular vibrations, respectively [45]. Moreover, evidence is mounting that the interaction between excitons and under-damped vibrations whose energies commensurate exciton splittings may be at the heart of the coherence beating probed in two-dimensional photon echo spectroscopy [37, 67, 133–137]. Although some insights into the importance of such resonances can be gained from Förster theory [7], the wider implications for optimal spatio-temporal distribution of energy [37, 138, 139], for modulation of exciton coherences [37, 67, 135, 136] and for collective pigment motion dynamics [137] have just recently started to be clarified.

The current state of the debate then suggests that a conceptual advance in understanding non-trivial quantum phenomena assisting electronic transport could emerge precisely from investigating non-classical features of the molecular motions and phonon environments that play such a key role. Techniques able to manipulate vibrational states [140, 141] and probe their quantum properties [142, 143] may indeed provide the experimental platform to address this issue.

In this chapter this question is investigated in a prototype dimer ubiquitous in light-harvesting antennae of cyanobacteria [144], cryptophyte algae [145, 146] and higher plants [147–149] and show that commensurate energies of exciton splitting and under-damped high-energy vibrations allows exciton-vibration dynamics to in-

duce and harness non-classical fluctuations of collective pigment motions for efficient energy transfer. Negative values of the Mandel  $Q$ -parameter [125] indicating sub-Poissonian phonon occupation fluctuations and, correspondingly, negative regions in a regularised quasi-probability  $P$  distribution in phase space [123, 124], unambiguously preclude any classical description of such fluctuations or its correlations with transport. Our results show a potential functional relevance of non-classicality of molecular fluctuations for exciton transport and therefore provide a framework to investigate similar non-trivial quantum phenomena in the large variety of biomolecular transport [150, 151], photoreception [152] and chemical sensing processes [153–155] that are known (or hypothesised) to be assisted by unequilibrated vibrational motion.

## 2.1 Prototype dimers and collective vibrations

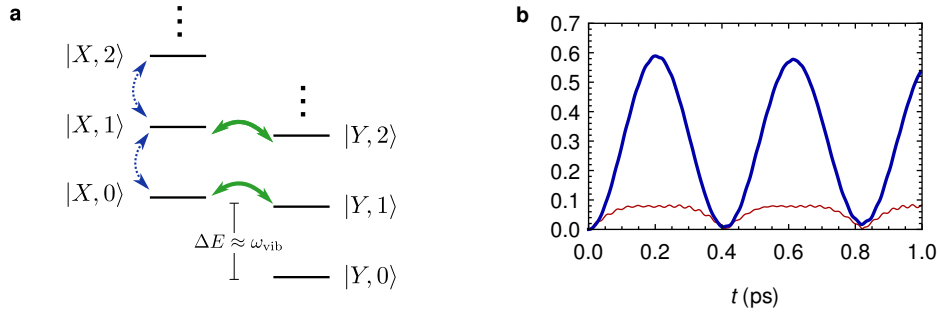


Figure 2.1: (a) The energy levels of the exciton-collective mode states used to describe energy transfer  $|X, n\rangle$ . The dashed blue arrows denote vibrational dynamics on the same exciton state while the green arrows denote exciton population (energy) transfer from  $|X, 0\rangle$  to  $|Y, 1\rangle$ . (b) Quantum coherent dynamics of the PEB<sub>50</sub> dimer in PE545 illustrating population of the lowest exciton  $\rho_{YY}(t)$  (thick blue curve) and the inter-exciton coherence in the ground-state of the collective mode  $|\rho_{X0-Y0}(t)|$  (thin red curve).

In this chapter we focus on a prototype dimer where each chromophore is strongly coupled to a quantized vibrational mode of frequency  $\omega_{\text{vib}}$  which is much larger than the thermal energy scale  $K_{\text{B}}T$ . If the vibration frequency and electronic-vibration coupling strength  $g$  are identical at each site, it is convenient to consider a representation of excited states of the sites as a two level system  $\sigma_z = (\sigma_2^+ \sigma_2^- - \sigma_1^+ \sigma_1^-)$ . We also introduce new operators  $b_{\pm}^\dagger = (b_1^\dagger \pm b_2^\dagger)/\sqrt{2}$  and  $b_{\pm} = (b_1 \pm b_2)/\sqrt{2}$  corresponding to centre of mass and relative displacement coordinates of the modes.

The Hamiltonian for the exciton-vibration dimer then reads as

$$H_{\text{ex-vib}} = \frac{\Delta\epsilon}{2}\sigma_z + V\sigma_x + \omega_{\text{vib}}b_-^\dagger b_- - \frac{g}{\sqrt{2}}\sigma_z(b_-^\dagger + b_-), \quad (2.1)$$

with  $\Delta\epsilon = \epsilon_1 - \epsilon_2$  and dependence on the centre of mass mode dropped as it does not couple to the electronic system. Tiwary and co-authors [137] pointed out that two-dimensional spectroscopy can probe the involvement of these anti-correlated, relative displacement motions in electronic dynamics. From now on and for simplicity we denominate this relative displacement mode as the collective mode.

For a dimer, the delocalised electronic (excitonic) eigenstates  $|X\rangle$  and  $|Y\rangle$  are symmetric and anti-symmetric linear combinations of the localised excited states

$$\begin{pmatrix} |X\rangle \\ |Y\rangle \end{pmatrix} = \begin{pmatrix} \cos\theta & \sin\theta \\ -\sin\theta & \cos\theta \end{pmatrix} \begin{pmatrix} |1\rangle \\ |2\rangle \end{pmatrix} \quad (2.2)$$

with mixing angle  $\theta = 1/2 \arctan(2|V|/\Delta\epsilon)$  ( $0 < \theta < \pi/4$ ) and energy difference  $\Delta E = \sqrt{\Delta\epsilon^2 + 4V^2}$ . Expanded into the basis of exciton-vibration states  $|X, n\rangle = \sigma_X^\pm \otimes (b_-^\dagger)^n / \sqrt{n!} |0, 0\rangle$ , the full exciton-vibration Hamiltonian reads

$$H_{\text{ex-vib}} = \begin{pmatrix} \frac{\Delta E}{2} & -\frac{g \cos 2\theta}{\sqrt{2}} & 0 & \dots & 0 & \frac{g \sin 2\theta}{\sqrt{2}} & 0 \\ -\frac{g \cos 2\theta}{\sqrt{2}} & \frac{\Delta E}{2} + \omega_{\text{vib}} & -g \cos 2\theta & \dots & \frac{g \sin 2\theta}{\sqrt{2}} & 0 & g \sin 2\theta \\ 0 & -g \cos 2\theta & \frac{\Delta E}{2} + 2\omega_{\text{vib}} & \dots & 0 & g \sin 2\theta & 0 \\ \vdots & \vdots & \vdots & \ddots & \vdots & \vdots & \vdots \\ 0 & \frac{g \sin 2\theta}{\sqrt{2}} & 0 & \dots & -\frac{\Delta E}{2} & \frac{g \cos 2\theta}{\sqrt{2}} & 0 \\ \frac{g \sin 2\theta}{\sqrt{2}} & 0 & g \sin 2\theta & \dots & \frac{g \cos 2\theta}{\sqrt{2}} & -\frac{\Delta E}{2} + \omega_{\text{vib}} & g \cos 2\theta \\ 0 & g \sin 2\theta & 0 & \dots & 0 & g \cos 2\theta & -\frac{\Delta E}{2} + 2\omega_{\text{vib}} \end{pmatrix}. \quad (2.3)$$

The couplings  $g \cos(2\theta)\sqrt{(n+1)/2}$  are responsible for transitions between vibrational states with the same excitonic state:  $|X, n\rangle$  to  $|X, n+1\rangle$ , whereas the couplings  $g \sin(2\theta)\sqrt{(n+1)/2}$  cause transitions between states  $|X, n\rangle$  to  $|Y, n+1\rangle$  - denoted by blue dashed and solid green arrows respectively in Figure 2.1 a.

We are interested in dimers that satisfy  $\Delta E \sim \omega_{\text{vib}} > g > V$  where the effects of under-damped high-energy vibrational motions are expected to be most important [37, 144, 149]. Several natural light-harvesting antennae include pairs of chromophores that clearly fall in this regime. Two important examples of such dimers are illustrated in Figure 2.2 and correspond to the central PEB<sub>50c</sub>-PEB<sub>50d</sub> dimer in the cryptophyte antennae PE545 [146] and a Chl<sub>b601</sub>-Chl<sub>a602</sub> pair in the LHCII



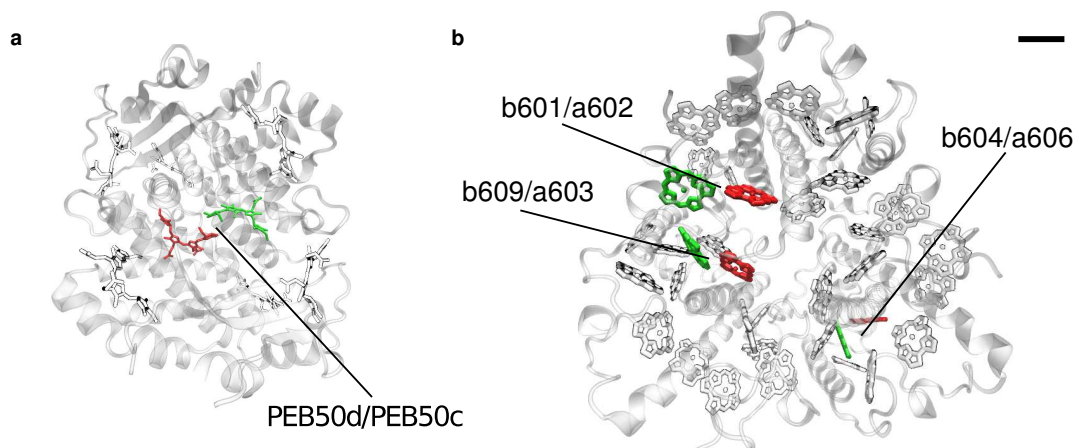


Figure 2.2: (a) Representation of the pigments and protein environment of a phycoerythrin 545 (PE545) antenna complex from Cryptophyte *Rhodomonas* CS24 (Protein Data Bank ID code 1XG0 (ref. 145)). The central phycoeritrobin (PEB) dimer pigments PEB<sub>50c</sub> and PEB<sub>50d</sub> are highlighted red and green respectively. (b) Representation of the light harvesting complex II (LHCII) present in higher plants. In this case *Spinacia oleracea* (Protein Data Bank ID code 1RWT (ref. 147)). Several pairs of close Chl<sub>b</sub>-Chl<sub>a</sub> (red-green) chlorophylls are highlighted. Scale bar: 1 nm.

complex of higher plants [149]; both corresponding to systems which have exhibited coherence beating in two-dimensional spectroscopy [12, 13, 156]. For the PEB<sub>50</sub> dimer from PE545,  $\Delta\varepsilon = 1042 \text{ cm}^{-1}$  and  $V = 92 \text{ cm}^{-1}$  such that  $\Delta E = 1058.2 \text{ cm}^{-1}$  being quasis resonant with an intramolecular mode of frequency  $\omega_{\text{vib}} = 1111 \text{ cm}^{-1}$ . The strength of linear coupling to this mode is  $g = \omega_{\text{vib}}\sqrt{0.0578} = 267.1 \text{ cm}^{-1}$ . Parameters have been obtained from [145, 146]. The Chl<sub>(b601)</sub>-Chl<sub>(a602)</sub> pair from LHCII has electronic parameters [157]  $\varepsilon_{(b601)} = 15764 \text{ cm}^{-1}$ ,  $\varepsilon_{(a602)} = 15103 \text{ cm}^{-1}$ ,  $V = -47.1 \text{ cm}^{-1}$  and resulting  $\Delta E = 667.7 \text{ cm}^{-1}$ . A vibrational mode of frequency  $\omega_{\text{vib}} = 742.0 \text{ cm}^{-1}$  is close to this energy gap and each chromophore couples to this mode with strength  $g = \omega_{\text{vib}}\sqrt{0.03942} = 147.3 \text{ cm}^{-1}$ , as obtained from [149].

Importantly, in each of these systems, the dimer considered contributes to an dominant energy transfer pathway towards exit sites [12, 146] suggesting that the phenomena we discuss will have an effect in the performance of the whole complex. Moreover, synthetic versions of such prototype dimers could be available [158]. Most remarkably, LHCII is likely the most abundant light-harvesting complex on Earth [148], while cryptophyte antennae like PE545 are ecologically important as they support photosynthesis under extreme low-light conditions [159, 160]. From this perspective, the dimers of interest are exceptionally relevant biomolecular prototypes. Spectroscopy studies indicate that these dimers are subject to a structured

exciton-phonon interaction as considered in our model. For the PEB<sub>50</sub> dimer, the intramolecular mode of interest has frequency around 1111 cm<sup>-1</sup> [146] which compares with the frequency of the breathing mode of the tetrapyrrole [161] (Carles Curutchet, personal communication). In the case of Chl<sub>b-a</sub> pair it has been shown that a mode around 750 cm<sup>-1</sup> is coupled to the electronic dynamics [149] and this energy is close to the frequency of in-plane deformations of the pyrrole [162]. Furthermore, vibrational dephasing in chromophores [163] and in other systems such as photoreceptors [164] is known to be of the order of picoseconds. Some aspects of the influence of non-equilibrium vibrational motion in these specific dimers have been considered before [37, 165], but none of these works have addressed the question of interest: can vibration-assisted transport exploit quantum phenomena that has no classical analogue?

## 2.2 Non-classicality via coherent exciton-vibrational dynamics

We first consider the quantum coherent dynamics of the exciton-vibration dimer in the absence of a thermal background to illustrate how non-classical behaviour of the collective motion emerges out of an initial thermal phonon distribution and an excitonic state with no initial superpositions:  $\rho(t_0) = |X\rangle\langle X| \otimes \varrho_{\text{vib}}^{\text{th}}$  which written in the basis of exciton-vibration states of the form  $|X, n\rangle$  becomes  $\rho(t_0) = \sum_n P_n^{\text{th}} |X, n\rangle\langle X, n|$ . Here  $n$  denotes the phonon occupation number of the relative displacement mode coupled to exciton dynamics while  $P_n^{\text{th}}$  denotes the thermal occupation of such level. For the purposes of calculations, the Fock space of vibration is truncated at level  $n = 9$ , which results in converged dynamics of the exciton-vibration systems considered here. The observables of interest are the population of the lowest excitonic state  $\rho_{YY}(t) = \sum_n \langle Y, n | \rho(t) | Y, n \rangle$ , the absolute value of the coherence  $\rho_{X0-Y0}(t) = \langle X, 0 | \rho(t) | Y, 0 \rangle$  which denotes the inter-exciton coherence in the ground-state of the collective vibrational mode, and the non-classicality given by negative values  $Q(t)$  and corresponding negativities in the regularised quasiprobability distribution  $P_w(\alpha)$ . Hamiltonian evolution generates coherent transitions from states  $|X, n\rangle$  to  $|Y, n+1\rangle$  with a rate  $f$  that depends on the exciton delocalisation ( $|V|/\Delta\epsilon$ ), the coupling to the mode  $g$ , and the phonon occupation  $n$  i.e.  $f \simeq g(2|V|/\Delta\epsilon)\sqrt{(n+1)/2}$ . Since  $\omega_{\text{vib}} \gg K_{\text{B}}T$  the ground state of the collective mode is largely populated, such that the Hamiltonian evolution of the initial state is dominated by the evolution of the state  $|X, 0\rangle$ . This implies that the ener-

getically close exciton-vibration state  $|Y, 1\rangle$  becomes coherently populated at a rate  $f \simeq g(2|V|/\Delta\epsilon)$ , leading to the oscillatory pattern observed in the probability of occupation  $\rho_{YY}(t)$  as illustrated in Fig. 2.1b.

The low-frequency oscillations of the dynamics of  $\rho_{YY}(t)$  cannot be assigned to the exciton or the vibrational degrees of freedom alone as expected from quantum-coherent evolution of the exciton-plus-effective mode system. For instance, if the mode occupation is restricted to at most  $n = 1$ , the period of the amplitude of  $\rho_{YY}(t)$  is approximately given by the inverse of

$$\frac{1}{2} \left( \sqrt{(\Delta E - \alpha)^2 + \frac{2g^2 4V^2}{\alpha \Delta E}} - (\Delta E + \alpha) \right), \quad (2.4)$$

with  $\alpha^2 = 2g^2 + \omega_{\text{vib}}^2$  and  $(2g^2 4V^2/\alpha^2 \Delta E^2) \ll 1$ . Further analytic expressions for the dynamics of an exciton-vibration dimer which are valid in the current regime of interest are derived in [166, 166]. Coherent exciton population transfer is accompanied by beating of the inter-exciton coherence  $|\rho_{X0-Y0}(t)|$  with the main amplitude modulated by the same low-frequency oscillations of  $\rho_{YY}(t)$  and a superimposed fast oscillatory component of frequency close to  $\omega_{\text{vib}}$  (see Fig. 2.1b). This fast driving component arises from local oscillatory displacements: when  $V \simeq 0$  the time evolution of each local mode is determined by the displacement operator with amplitude  $\alpha(t) = g(1 - \exp(-i\omega_{\text{vib}}t))/\omega_{\text{vib}}$  [167].

As the state  $|Y, 1\rangle$  is coherently populated, the collective quantised mode is driven out of equilibrium towards a non-classical state in which selective occupation of the first vibrational level takes place thereby modulating occupation of higher levels. This manifests itself in sub-Poissonian phonon statistics as indicated by negative values of  $Q(t)$  shown in Fig. 2.3a. Similar phenomena have been described in the context of electron transport in a nanoelectromechanical system [168, 169]. Moreover, Fig. 2.3b shows that at times when  $Q(t)$  is negative i.e.  $t = 0.2$  ps the regularized quasiprobability distribution  $P_w(\alpha)$  at this time exhibits negativities thereby ruling out any classical description of the same phenomena. Interestingly, the non-classical properties of the collective vibrational motion resemble non-classicality of bosonic thermal states (completely incoherent states) that are excited by a single quanta [124, 170]. Importantly, such non-classical behaviour of the vibrational motion arises only when the electronic interaction between pigments is finite. For comparison, Fig. 2.3c shows that if  $V = 0$ , an electronic excitation drives the local under-damped vibration towards a thermal displaced state with super-Poissonian statistics ( $Q(t) > 0$ ) which has an associated positive probability

distribution in phase space as illustrated in Fig. 2.3d. In short, non-classicality of the collective mode quasi-resonant with the excitonic transition arises through the transient formation of exciton-vibration states.

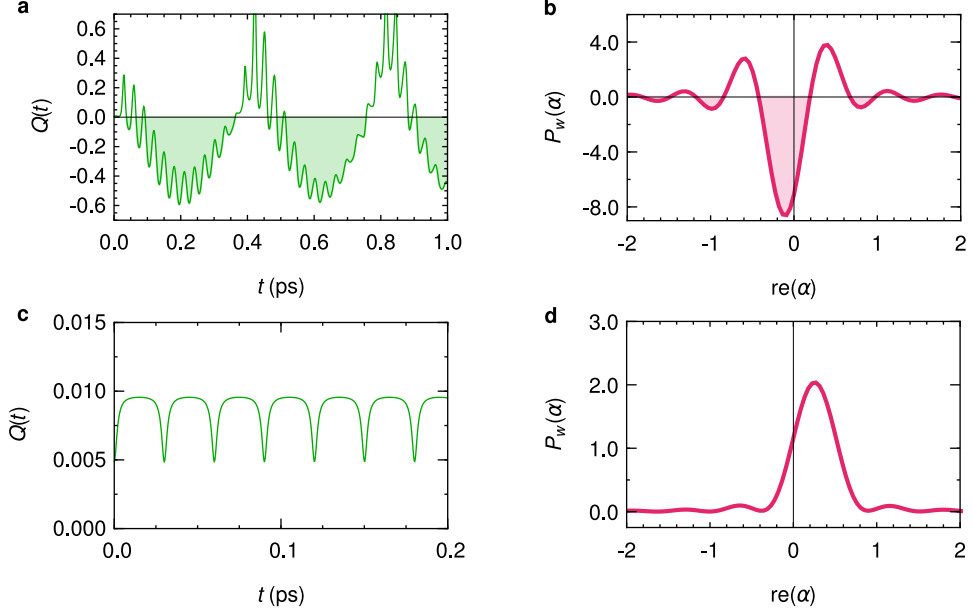


Figure 2.3: (a) Mandel  $Q$ -parameter of the relative displacement mode of the considered  $\text{PEB}_{50}$  dimer from PE545 when a biological electronic coupling is considered. Shaded regions denote times of non-classicality. (b) The associated regularised quasiprobability distribution  $P_w(\alpha)$  at  $t = 0.2$  ps. Shaded regions denote areas of negative probability. (c) Mandel  $Q$ -parameter of the intramolecular high-energy vibration when dipole coupling is zero and (d) the associated regularised quasiprobability distributions  $P_w(\alpha)$  at  $t = 0.2$  ps.

## 2.3 Dynamics under thermal relaxation

We now investigate the dynamics of the exciton-vibration dimer when each local electronic excitation additionally interacts with a low-energy thermal bath described by a continuous distribution of harmonic modes. The strength of this interaction is described by a Drude–Lorentz spectral density  $J_D(\omega)$ , with associated reorganisation energy  $\lambda$  and cut-off frequency  $\Omega_c < K_B T$ . The dynamics of the full exciton-vibration system are computed exactly using the HEOM approach described in section 1.3.1. We consider the exciton and vibration parameters of the  $\text{PEB}_{50}$  dimer and investigate the trends as functions of the reorganisation energy. As expected, the interplay between vibration-activated dynamics and thermal fluctuations leads

to two distinct regimes of energy transport as a function of  $\lambda$ . For our consideration of weak electronic coupling, the coherent transport regime is determined approximately by  $\sqrt{\lambda\Omega_c} \leq 2g|V|/\Delta\epsilon$ . Population of the low-lying exciton state is dominated by coherent transitions between exciton-collective mode states and the rapid, non-exponential growth of  $\rho_{YY}(t)$  in this regime can be traced back to coherent evolution from  $|X, 0\rangle$  to  $|Y, 1\rangle$ . At longer time scales thermal fluctuations induce incoherent transitions from  $|X, 0\rangle$  to  $|Y, 0\rangle$  with a rate proportional to  $\sqrt{\lambda\Omega_c}$ , thereby stabilising population of  $\rho_{YY}(t)$  to a particular value as can be seen in Fig. 2.4d. This behaviour is illustrative of what is expected in the dimer Chl<sub>b-a</sub> for which  $\lambda = 37 \text{ cm}^{-1}$  as obtained from ref. 149. To confirm this we have computed the exciton-vibration dynamics with parameters of the Chl<sub>b-a</sub> dimer, the results of which are shown in Fig. 2.A.1. In contrast, for  $\sqrt{\lambda\Omega_c} > 2g|V|/\Delta\epsilon$  population transfer to  $\rho_{YY}(t)$  is incoherent. For the PEB<sub>50</sub> dimer  $\lambda \sim 110 \text{ cm}^{-1}$  which places this dimer in this incoherent regime where  $\rho_{YY}(t)$  has a slow but continuous exponential rise reflecting the fact that thermal fluctuations inducing transitions from  $|X, n\rangle$  to  $|Y, n\rangle$  now have a large contribution to exciton transport. However, even in this regime, transfer to  $\rho_{YY}(t)$  is always more efficient with the quasi-resonant mode than in the situations where only thermal-bath induced transitions are considered (see dashed lines in Fig. 2.4a-c). The underlying reason is that before vibrational relaxation takes place (around  $t = 1 \text{ ps}$ ), the system is transiently evolving towards a thermal configuration of exciton-collective mode states. Hence, in both coherent and incoherent population transfer regimes transfer to the lowest exciton state involves a transient, selective population of first vibrational level of the collective mode.

For completeness, we present in Fig. 2.4d, e and f how the beating patterns of the coherence  $\rho_{X0-Y0}(t)$  reveal the structured nature of the exciton-phonon interaction and witnesses whether there is coherent exciton-vibration evolution as it has been pointed out by recent studies [67, 136]. The frequency components of such oscillatory exciton coherences vary depending of the coupling to the thermal bath. In the coherent regime, as  $\rho_{X0-Y0}(t)$  follows exciton populations, the main amplitude is modulated by the same relevant energy difference between exciton-vibration states (see Fig. 2.4b and e). This behaviour is relevant for the parameter regime of the Chl<sub>b-a</sub> dimer (see Fig 2.A.1). In contrast, for the PEB<sub>50</sub> dimer, the short-time oscillations of  $\rho_{X0-Y0}(t)$  (between  $t = 0$  and  $t = 0.1 \text{ ps}$ ) arise from purely electronic correlations due to bath-induced renormalization of the electronic Hamiltonian [171]. This exciton coherence retains the superimposed driving at a frequency  $\omega_{\text{vib}}$  and is

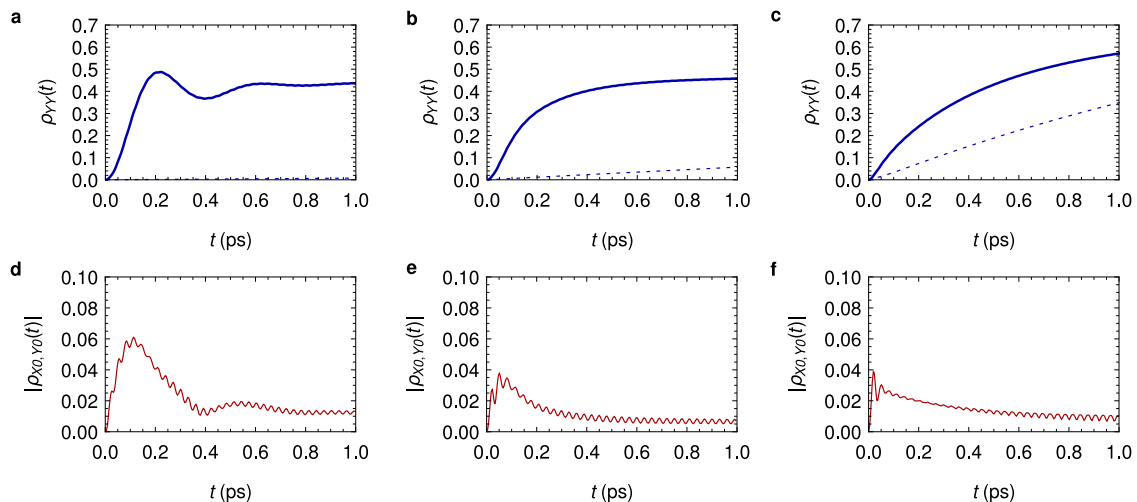


Figure 2.4: (a-c) The dynamics of  $\rho_{YY}(t)$  with (thick blue curve) and without (dashed curve) coupling to vibration and (d-f)  $|\rho_{X0,Y0}(t)|$  for the exciton-vibration parameters of the PEB<sub>50</sub> dimer with three interaction strengths to the low-energy thermal bath, left to right  $\lambda = 6 \text{ cm}^{-1}$ ,  $\lambda = 35 \text{ cm}^{-1}$  and  $\lambda = 110 \text{ cm}^{-1}$ .

accompanied by non-classicality as it will be described shortly, indicating that vibrational motion is still out of thermal equilibrium. The dynamical features presented in Fig. 2.4c and f agree with previous findings based on a perturbative approach [37] and with the time-scales of the exciton coherence beating reported for cryptophyte algae [13, 134]. The transition from coherent to incoherent exciton population dynamics is then marked by the onset of energy dissipation of the exciton-vibration system as shown in Fig. 2.5a, b and c where  $E(t) = \text{Tr}\{H_{\text{ex-vib}}\rho(t)\}$  has been depicted for different values of  $\lambda$ . While exciton population growth is non-exponential, energy dissipation into the thermal bath is transiently prevented as indicated by periods of positive slope of  $E(t)$  as happens in Fig. 2.4c and 2.4f. Quantification of the energy that is transiently “extracted” from the low-energy thermal bath can provide an interesting physical interpretation of the advantages of non-exponential exciton transfer in the framework of non-equilibrium thermodynamics [172]. This is further explored in Chapter 4.

### 2.3.1 Non-classicality

Interaction with the thermal environment would eventually lead to the emergence of classicality at long times. However, in the picosecond time scale of interest, the collective mode exhibits periods of non-classicality across a wide range of thermal bath couplings  $\lambda$  as indicated by sub-Poissonian fluctuations with  $Q(t) < 0$  in Figure

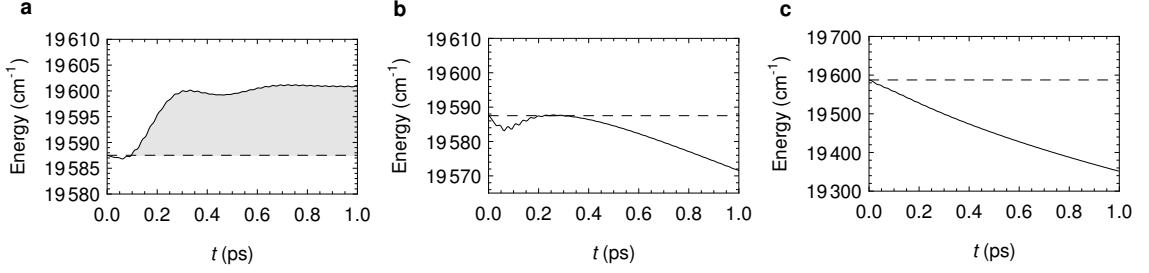


Figure 2.5: (a-c) The energy of the exciton vibration system  $E(t) = \text{Tr}\{H_{\text{ex-vib}}\rho(t)\}$  Initial energy  $E(0)$ , displayed as dashed line and times where  $E(t) > E(0)$  are shaded.

2.6a-c and the corresponding negativities in the distributions  $P_w(\alpha)$  shown in Figure 2.6d-f. This survival of non-classicality is concomitant with a slow decay of the exciton-vibration coherence  $\rho_{X0,Y1}(t)$  as displayed in Figure 2.7.

Non-classical behaviour of collective fluctuations are then expected for the parameters of both the PEB<sub>50</sub> dimer for which  $\lambda = 110 \text{ cm}^{-1}$  and the Chl<sub>b-a</sub> dimer for which  $\lambda = 37 \text{ cm}^{-1}$ . The non-classical fluctuations predicted by  $Q(t)$  also agree with the non-classicality witnessed by the Klyshko parameter as displayed in Figure. 2.8. The selective population of the  $n = 1$  level of the relative displacement vibrational mode results in non-classical modulations of the nearest-neighbour populations and thus  $B_1 = 2P(0)P(2) - P(1)^2$  displays negative regions.

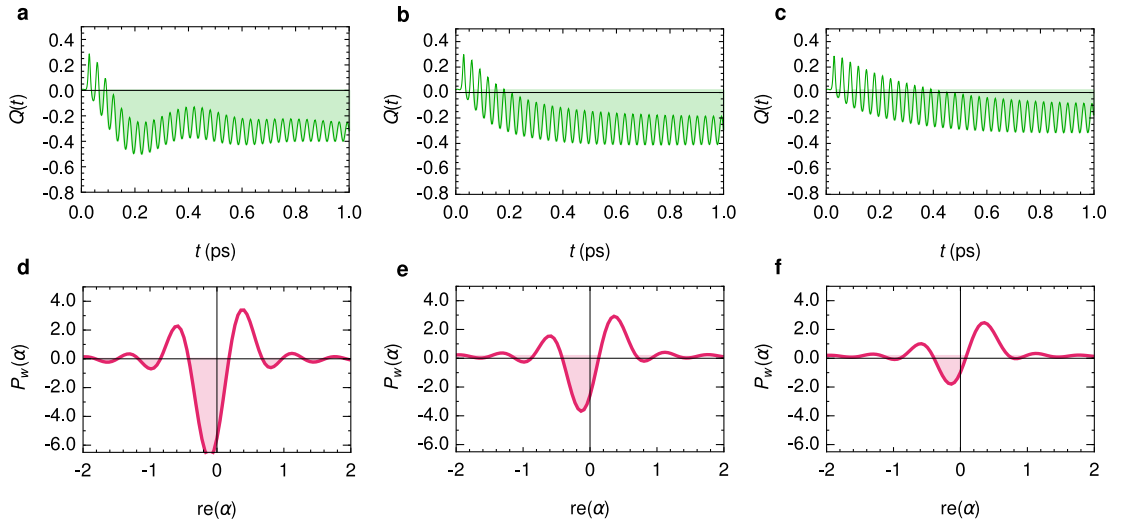
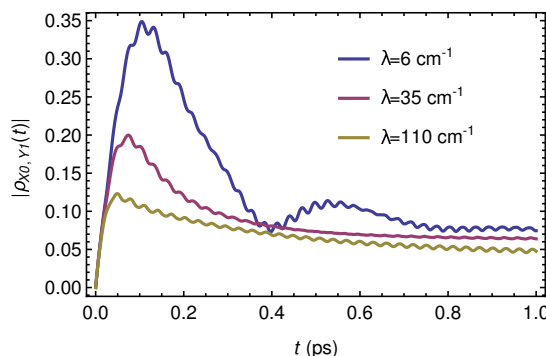
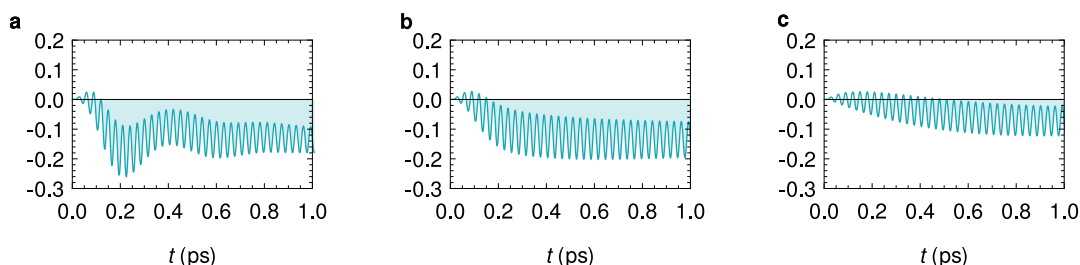


Figure 2.6: (a-c) Dynamics of the Mandel  $Q$ -parameter for  $\lambda = 6, 35, 110 \text{ cm}^{-1}$  respectively. Shaded regions denote times of non-classicality. (d-f) Regularised distribution  $P_w(\alpha)$  at  $t = 0.2 \text{ ps}$  for each corresponding value of  $\lambda$ . Shaded regions denote areas of negative probability.




 Figure 2.7: Exciton-vibration coherence  $\rho_{X0,Y1}$ 

As expected, the maximum non-classicality indicated by the most negative value of  $Q(t)$  decreases for larger reorganisation energies. Nonetheless, the time average of these non-classicality is not a monotonic function of  $\lambda$ . For moderate values of  $\lambda$ , the collective mode spends longer periods in states with non-classical fluctuations i.e. periods for which  $Q(t) < 0$  as seen in Fig. 2.6b thereby stabilising non-classicality at a particular level. This sub-picosecond stabilisation of non-classicality is expected in the regime of the  $\text{Chl}_{b-a}$  dimers as illustrated Fig. 2.A.1.


 Figure 2.8: Klyshko criterion  $B_1$  displays negative periods

## 2.4 The functional role of non-classicality

Non-classical fluctuations of collective motions correlate with exciton population transfer. In order to demonstrate this, we investigate quantitative relations between non-classicality and exciton energy transport by considering relevant integrated averages in the time scale of the Hamiltonian evolution of the exciton-vibration system denoted by  $\tau$ . For the parameters of the  $\text{PEB}_{50}$ , this time scale is about half a picosecond and is comparable to the time scale in which excitation energy would be distributed away to other chromophores or to a trapping state. The time integrated



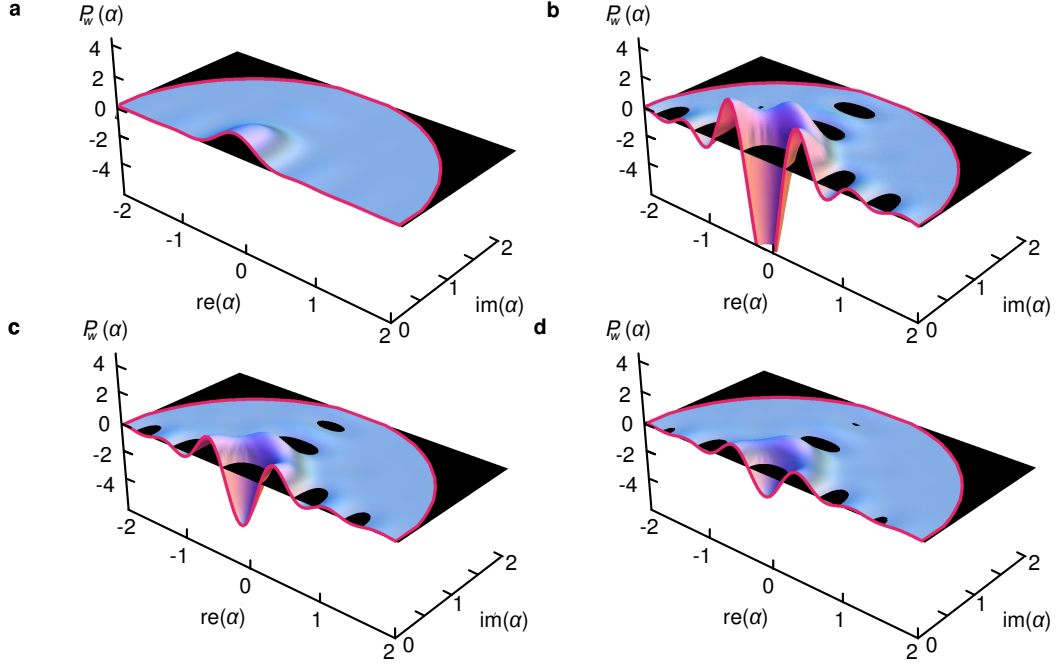


Figure 2.9:  $P_{5.0}(\alpha)$  at  $t = 0.2$  ps using a triangular non-classicality filter. (a) with  $V = 0$ , (b)  $\lambda = 0 \text{ cm}^{-1}$ , (c)  $\lambda = 35 \text{ cm}^{-1}$  and (d)  $\lambda = 110 \text{ cm}^{-1}$

averages over  $\tau$  are defined as:

$$\langle F[\rho(t)] \rangle_\tau = \frac{1}{\tau} \int_0^\tau dt F[\rho(t)] , \quad (2.5)$$

where  $F[\rho(t)]$  corresponds to the exciton population  $\rho_{YY}(t)$  and the non-classicality of the under-damped collective mode through periods of sub-Poissonian statistics  $Q(t)\Theta[-Q(t)]$  as functions of the coupling to the bath  $\lambda$ . As shown in Fig. 2.10 the average exciton population and non-classicality follow a similar non-monotonic trend as a function of the coupling to the thermal bath, indicating a direct quantitative relation between efficient energy transfer in the time scale  $\tau$  and the degree of non-classicality. The appearance of a maximal point in the average non-classicality as a function of the system-bath coupling indicates that the average quantum response of the collective anti-correlated motion to the impulsive electronic excitation, is optimal for a small amount of thermal noise.

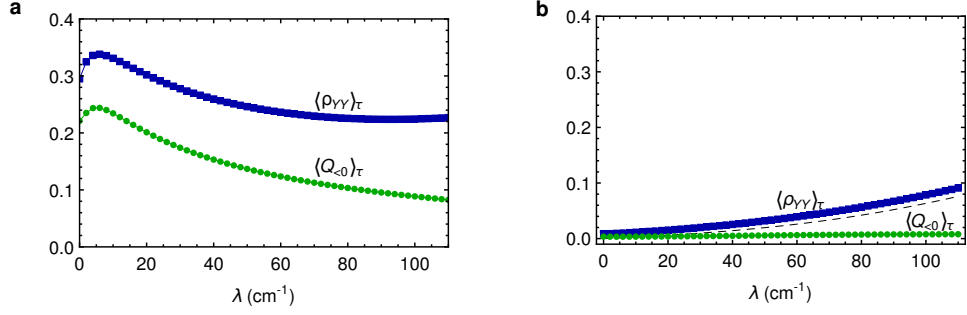


Figure 2.10: Time integrated averages of exciton population  $\rho_{YY}(t)$  and non-classicality as quantified by  $Q(t)\Theta[-Q(t)]$  (blue and green respectively) as functions of coupling to the thermal background by fixing environment cut-off frequency  $\Omega_c = 100 \text{ cm}^{-1}$  and varying reorganization energy  $\lambda$  with exciton-vibration parameters corresponding to the PEB<sub>50</sub> dimer. **(a)**  $\omega_{\text{vib}} = 1111 \text{ cm}^{-1}$  **(b)**  $\omega_{\text{vib}} = 1520 \text{ cm}^{-1}$

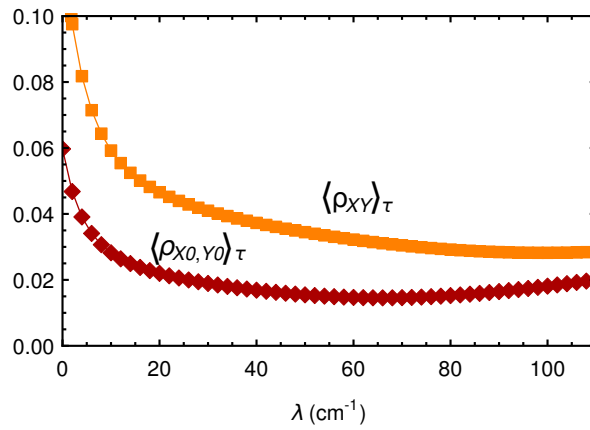


Figure 2.11: Time averages of excitonic coherences

## 2.5 Concluding remarks and outlook

The prototype exciton-vibration dimers here investigated are representative of interband-like transfer pathways present in the majority of light-harvesting complexes. For instance in the LHCII complex, the considered dimer contributes to the fastest component of the  $\text{Chl}_b \rightarrow \text{Chl}_a$  inter-band transfer pathway that directs excitation energy towards exit sites [157]. The demonstration that non-classicality is concomitant with efficient vibration-assisted transfer in these dimers therefore suggests that non-classical phenomena will have a contribution to the efficiency of the whole complex. A rigorous quantitative estimation of such contribution requires both a careful extension of our formalism to quantify these features in a multi-modal system (as likely other non-equilibrated vibrational motion will be involved) and a careful weighting of the vibration-assisted processes in the overall spatio-temporal distribution of energy.

The framework we propose can also be applied to gain insights into the non-classical response of vibrational motion in a variety of transport [150, 151] and sensing processes in biomolecules [152, 153]. Of particular interest are charge transfer in reaction centres [150] and isomerisation of photoreceptors [152] where specific intramolecular vibrational motions are known to be driven out of thermal equilibrium during the light-initiated electronic dynamics. It will also be interesting to use this framework to understand possible non-trivial quantum behaviour of molecular motions in chemical sensors [153] that are conjectured to operate through weak electronic interactions to sense molecular vibrations of the order of a thousand wavenumbers [154, 155].

Future work might address the quantification of non-classicality in a larger system. Efficient vibration-assisted transport within a dimer only contributes to the efficiency of a larger system if it lies in a relevant transfer pathway. Expanding the system Hilbert space to include many vibrational modes rapidly becomes computationally intractable. Further studies could explicitly consider the exciton-vibration dynamics due to selected localised vibrational modes of particular chromophores and treat the vibrational modes of remaining chromophores as part of the bath. The HEOM approach including under-damped Brownian oscillator spectral density components can accurately account for these vibrations. This would enable one to theoretically probe the non-classicality of vibrational motions local to particular chromophores of the system by retaining their full state, whilst efficiently but accurately accounting for the influence of the vibrational modes of the remaining chromophores whose state is not retained.

We have also illustrated how in our prototype dimer with biologically relevant parameters, exciton-vibration dynamics can lead to non-exponential excitonic energy distribution whereby dissipation into a low-energy thermal bath can be transiently prevented. From this view, coherent vibrational motions that do not relax quickly and whose fluctuations cannot be described classically may be seen as an internal quantum mechanism controlling energy distribution and storage. Further insights into the advantage of these non-trivial quantum behaviour may therefore be gained in a thermodynamic framework [172, 173].

In conclusion, we have provided theoretical evidence that vibration-assisted exciton transport in prototype dimers, representative of interband-like transitions in a variety of photosynthetic light-harvesting antennae, can exploit non-trivial quantum phenomena which cannot be reproduced by any classical counterpart, namely, non-classical fluctuations of collective pigment motions. Given that a variety of transport [150, 151] and sensing phenomena [152] in biomolecules are known to involve non-equilibrium vibrational motion, our findings have broad implications for the field of quantum effects in biology as they suggest that investigating the non-classical nature of molecular fluctuations harnessed in these processes could be key to reveal a role for truly non-trivial quantum features.

## 2.A LHCII Chl<sub>(b601)</sub>-Chl<sub>(a602)</sub> dimer

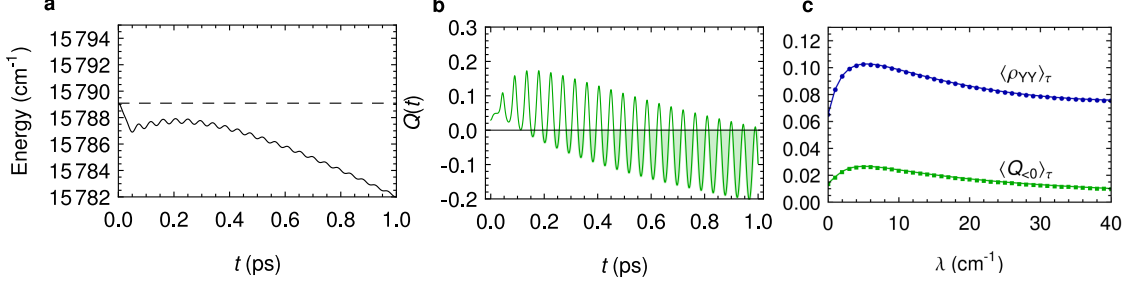


Figure 2.A.1: The LHCII complex of green plants contains weakly electronically coupled dimers whose energy gaps are resonant with vibrational modes. Here we present results from the Chl<sub>(b601)</sub>-Chl<sub>(a602)</sub> pair with electronic parameters [157]  $\varepsilon_{(b601)} = 15764 \text{ cm}^{-1}$ ,  $\varepsilon_{(a602)} = 15103 \text{ cm}^{-1}$ ,  $V = -47.1 \text{ cm}^{-1}$  and resulting  $\Delta E = 667.7 \text{ cm}^{-1}$ . A vibrational mode of frequency  $\omega_{\text{vib}} = 742.0 \text{ cm}^{-1}$  is close to this energy gap and each chromophore couples to this mode with strength  $g = \omega_{\text{vib}} \sqrt{0.03942} = 147.3 \text{ cm}^{-1}$ , as obtained from ref. 149. The thermal background is characterized by  $\lambda = 37 \text{ cm}^{-1}$ ,  $\Omega_c = 30 \text{ cm}^{-1}$  as in ref. 149. The strength of system-bath interactions  $\sqrt{\lambda \Omega_c}$  is smaller than in PE545 and therefore this dimer lies closer to the regime of coherent evolution of the exciton-vibration system, where the dissipation energy into the bath is transiently prevented. Shown here are (a) the energy of the exciton-vibration system and (b) the Mandel  $Q$  parameter of the vibrational mode for  $\lambda = 37 \text{ cm}^{-1}$  (shaded regions denote times of non-classicality) and (c) averages over timescale  $\tau \approx 0.4 \text{ ps}$  as a function of reorganisation energy.

## Chapter 3

# Quantum enhanced features of vibration-assisted excitation energy transport

*We provide a systematic comparison of electronic dynamics assisted by quantized vibrations and the corresponding dynamics if a classical description of vibrational motions is imposed. We identify features of the excitation energy transport which are enhanced when quantum fluctuations of molecular motions are properly accounted for. We find that the classical model of vibrations employed is less able to direct energy towards particular chromophores, does not correctly predict the oscillatory transfer of energy between the electronic and vibrational components and cannot account correctly for storage of energy in vibrations. The enhancement of these traits of dynamics when quantized vibrations are present suggests the inadequacy of a classical description of vibrations.*

The preceding chapter demonstrated that the transport of energy between the electronic degrees of freedom of an exciton-vibration dimer is enhanced by non-classical vibrational motions. It is therefore pertinent to consider what other features of electronic dynamics are enabled by a non-classical vibrational state. In this chapter we address this issue by considering a four site system and enforcing a *classical* description of the vibrations. By contrasting the resulting electronic dynamics with those resulting when a non-classical vibrational state is allowed, we identify quantum enhanced features of vibration-assisted excitation energy transport.

Models of excitonic transport where vibrational degrees of freedom are treated

classically have been formulated [67, 127, 128, 174, 175]. In fact in the high temperature limit where Matsubara correction terms are neglected, the non-perturbative hierarchical expansion method for an over-damped Brownian oscillator spectral density has been demonstrated [176] to be equivalent to the Zusman equation, a theory in which vibrations are described classically. In ref. 177 it was illustrated that such a classical model can reproduce the efficient noise assisted transport observed in the pure dephasing model of Haken and Strobl [85]. Yet, as discussed in section 1.3.2 this model supposes that the influence of the environment is to introduce fast fluctuations of site energies described by classical Gaussian noise process. Chin *et al.* [67] employed a quasi-classical model of vibrations to elucidate that the underlying mechanism behind the dynamical generation of excitonic coherences is the effective driving of the system introduced by strong interaction with vibrational modes. This model is the analogue of semi-classical descriptions of light widely applied in the field of quantum optics [121, 178]. In this chapter we demonstrate that while this model may account for certain features of the electronic dynamics, it neglects the aspects that result in a quantum-enhanced performance. We therefore highlight features of electronic dynamics which are enhanced when a fully quantum description of the vibration is used instead.

### 3.1 Quasiclassical description of molecular vibrations

We identify a small number of modes of interest and separate them from the bath Hamiltonian (1.5). We denominate these as ‘system modes’ and the remaining modes as ‘bath modes’. A classical description of the system modes is obtained by replacing displacement operators with their expectation value  $X_{i,k}(t) = \text{Tr} [(b_{i,k} + b_{i,k}^\dagger) \rho_{\text{vib}}(t)]$ , in the corresponding the interaction term (1.6). The time dependence of the expectation values is determined in the Heisenberg picture. This interaction with system modes results a time dependent effective electronic Hamiltonian,

$$H_{\text{ex}}^{\text{cl}}(t) = H_{\text{ex}} + \sum_{i,k} \sigma_i^+ \sigma_i^- g_{i,k}^{\text{vib}} X_{i,k}(t), \quad (3.1)$$

wherein site energies are modulated by the displacement of a classical harmonic oscillator whose evolution is governed by

$$\ddot{X}_{i,k}(t) + \Gamma_{i,k} \dot{X}_{i,k}(t) + (\omega_{i,k}^{\text{vib}})^2 X_{i,k}(t) = -2\omega_{i,k}^{\text{vib}} g_{i,k}^{\text{vib}} \rho_{ii}(t). \quad (3.2)$$

This is the equation of motion for a classical harmonic oscillator which is forced by chromophore occupation probabilities  $\rho_{ii}(t) = \text{Tr} [\sigma_i^+ \sigma_i^- \rho_{\text{ex}}(t)]$ . Phenomenological damping of the classical oscillator has been included at rate  $\Gamma_{i,k}$ . The evolution of the excitonic system under the influence of both classical system and quantized bath modes is given by

$$\dot{\rho}_{\text{ex}}(t) = -i[H_{\text{ex}}^{\text{cl}}(t), \rho_{\text{ex}}(t)] + \mathcal{D}_t \rho_{\text{ex}}(t) , \quad (3.3)$$

where the time dependence of  $H_{\text{ex}}^{\text{cl}}(t)$  is determined by simultaneously solving the equations of motion for system modes (3.2). The influence of bath modes is accounted for by the time dependent super-operator  $\mathcal{D}_t$ . In the present case the influence of the bath modes is described using the truncated hierarchical expansion for a Drude–Lorentz spectral density  $J_{\text{D}}(\omega)$  and therefore the time dependence of  $\mathcal{D}_t$  is determined by the hierarchy of equations (1.32), now also subject to the effective system Hamiltonian  $H_{\text{ex}}^{\text{cl}}(t)$ . To describe an initially thermal state for the system modes,  $X_{i,k}(0)$  and  $\dot{X}_{i,k}(0) = P_{i,k}/\omega_{i,k}^{\text{vib}}$  are sampled from the Wigner distribution of a thermal state [179], namely  $X_{i,k}$  and  $P_{i,k}(0) \sim \mathcal{N}(0, \coth(\frac{\beta\omega_{i,k}^{\text{vib}}}{2}))$ . Here  $X \sim \mathcal{N}(\mu, \sigma^2)$  denotes that the random variable  $X$  is normally distributed with mean  $\mu$  and variance  $\sigma^2$ . A sufficiently large ensemble ( $\sim 5000$ ) of the electronic dynamics resulting from these initial conditions is averaged until converged. The distribution function  $p(X_{i,k}, P_{i,k})$ , for the conjugate coordinates of the classical vibrations describes the ensemble of trajectories of  $X_{i,k}$  and  $P_{i,k}$  and is evidently positive at all times. In the preceding chapter it was demonstrated that vibrations can transiently display negative regions of quasi-probability distribution which cannot be captured by this description.

A fully quantum mechanical description of the system modes can be achieved by following the approach of chapter 2 and extending the Hilbert space of the system to include the quantized vibrations. However this approach does not scale well for application to systems with many chromophores or modes. Since the emphasis of this chapter is on the features of *electronic* dynamics which classical vibrational modes cannot reproduce, it suffices to discard the information contained in the full state of the vibrational mode and only calculate the reduced dynamics of the electronic system. To achieve this under-damped Brownian oscillator components  $J_{\text{BO}}^q(\omega)$  (equation (1.16)) with broadening equal to  $\Gamma_{i,q}$  are added to the spectral density described within the dissipator  $\mathcal{D}_t$  and the un-driven system Hamiltonian  $H_{\text{ex}}$  is considered. The hierarchical expansion in equation (1.32) then yields converged



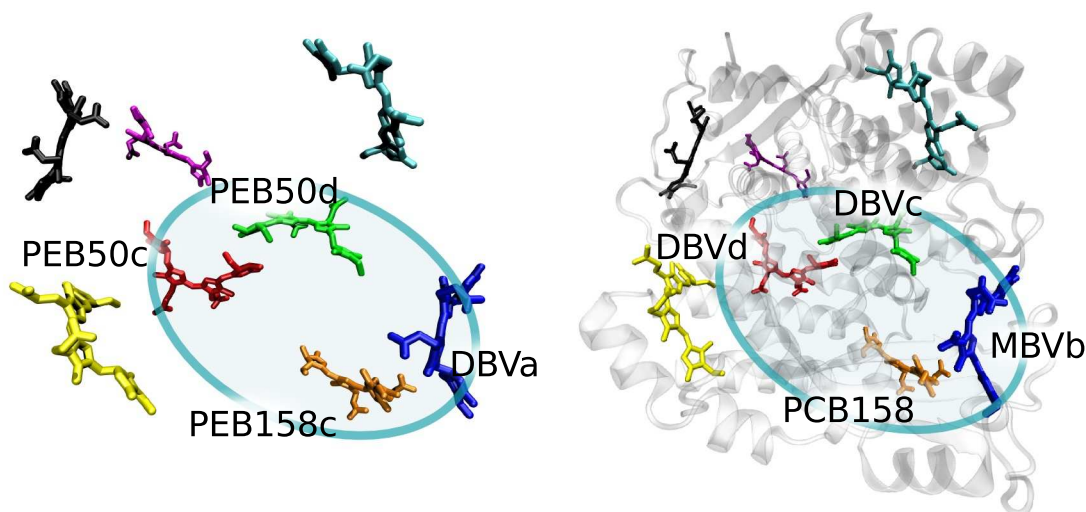


Figure 3.1: (a) Representation of the arrangement of chromophores in the phycoerythrin 545 antenna complex from the cryptophyte *Rhodomonas* CS24. Protein Data Bank ID code 1XG0 [145](#) (b) The chromophores and protein scaffold of the phycocyanin 645 antenna complex from the cryptophyte *Chroomonas* CCMP270. Crystal structure courtesy of G. D. Scholes.

reduced dynamics of the electronic system under the influence of both quantized system modes and bath modes  $J_D(\omega) + \sum_q J_{BO}^q(\omega)$  given that the hierarchy is truncated at a sufficiently high tier.

## 3.2 Cryptophyte antennae proteins

To illustrate the differences in electronic dynamics resulting from quantum and classical vibrations, we study relevant units from the structurally similar light harvesting antenna types found in two different species of cryptophyte marine algae - PE545 and PC645. Whilst in PE545 all pigments are comparatively weakly coupled due to large inter-pigment distances, the PC645 species, which evolved around 30 million years later [\[180\]](#), contains a pair of strongly electronically coupled dihydrobiliverdin (DBV) bilins at its centre. This difference allows us to explore the role of electronic coupling strength in otherwise similar systems. We extend the study of the previous chapter to a tetrameric (four site) system and consider the energy transfer dynamics between analogous sites of the two species as illustrated in Fig. [3.1](#).

In the previous chapter the central PEB<sub>50</sub> dimer of the PE545 complex was studied using electronic parameters which were determined from a combination of

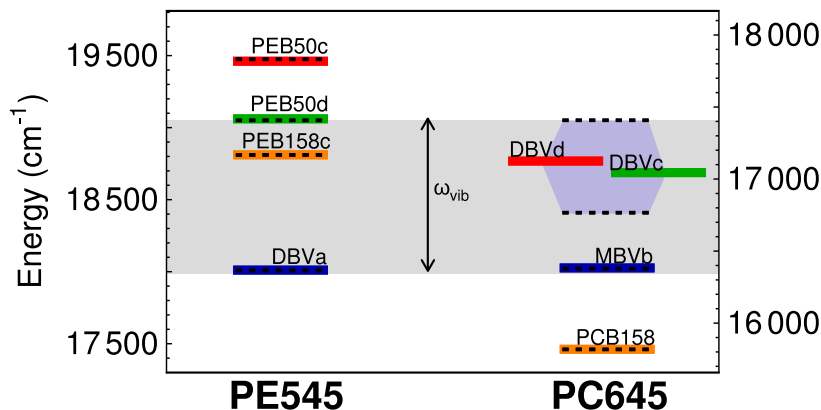


Figure 3.2: Exciton energies in PE545 and PC645. The strongly coupled DBV dimer in PC645 has delocalised exciton states. Both systems feature a vibrational mode closely resonant with the energy difference between high energy state and an exit chromophore.

configuration interaction singles (CIS) calculations and an evolutionary based search to fit linear spectra [146]. Subsequent calculations using a combined quantum mechanics and molecular mechanics model which accounts for solvent electronic polarization (QM/MMPol) [181], have predicted a smaller site energy difference for this dimer [182]. The revised energy gap of around  $400\text{ cm}^{-1}$  may lie close to low energy vibrational modes, but otherwise places the dimer close to the regime of incoherent Förster transfer which already predicts a rapid (incoherent) transfer of energy between these two sites due to the smaller energy gap. However, with these revised parameters the energy difference between excitons primarily localised on the the lower energy central dimer chromophore and an outermost DBV chromophore matches closely matches the  $1111\text{ cm}^{-1}$  mode. We therefore consider a subunit indicated in Fig. 3.1a, which comprises the ‘donating’ PEB<sub>50</sub> dimer, an intermediate chromophore (PEB<sub>158c</sub>) and a low energy ‘accepting’ chromophore (DBV<sub>a</sub>). The electronic parameters for this subunit are provided in Table 3.A.1 and were taken from the results of QM/MMPol calculations including the adjusted site energies which reproduce linear spectra [182]. For the PC645 complex, we consider the analogous tetramer subunit as shown in Fig. 3.1b. The main difference is that the central dimer comprises strongly electronically coupled DBV chromophores. The electronic parameters are given in Table 3.A.2 and are taken from references 13, 58. The continuous thermal background is assumed to be identical for PE545 and PC645 units and characterized by Drude–Lorentz spectral density with  $\lambda = 100\text{ cm}^{-1}$  and  $\Omega_c = 100\text{ cm}^{-1}$ . The PC645 system also features strong coupling to vibrational

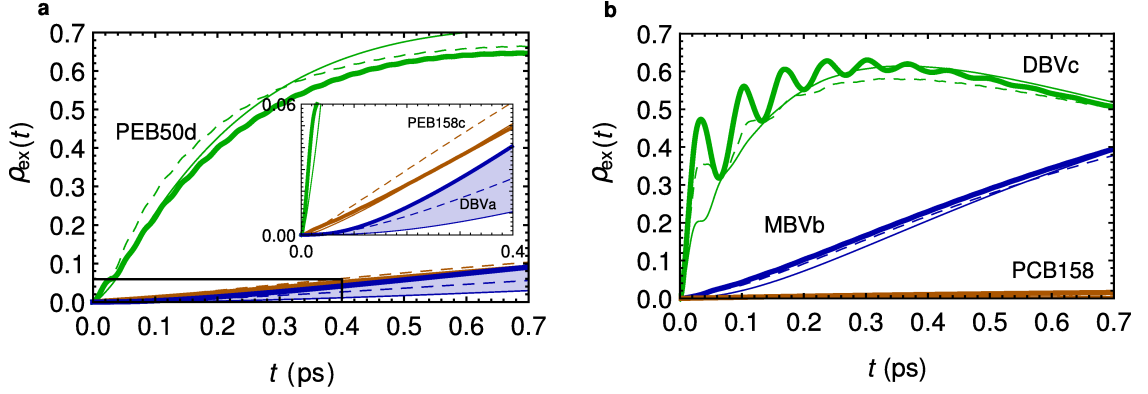


Figure 3.3: Exciton population dynamics in (a) PE545 and (b) PC645. Dynamics when a quantized vibration is present are thick curves. Dashed curves are dynamics when the classical vibration is present. Thin curves are exciton dynamics when the vibration is absent. The inset panel of (a) displays the detail of the boxed region in the main panel.

modes with  $\omega^{\text{vib}} = 1108 \text{ cm}^{-1}$  and  $g^{\text{vib}} = 221.6 \text{ cm}^{-1}$  [58]. We hypothesise a correspondence of this mode to the one in PE545 with  $\omega^{\text{vib}} = 1111 \text{ cm}^{-1}$  and  $g^{\text{vib}} = 267.1 \text{ cm}^{-1}$ . These modes may share a similar physical origin, particularly given that mixed quantum-classical molecular dynamics simulations in PE545 have determined that particular bilin intra-molecular motions are responsible for such high energy modes [40]. The energy levels of the two subunits and their resonance with the identified vibration are illustrated in Fig. 3.2.

We consider the electronic dynamics which results when the electronic degrees of freedom are initially in the highest energy excitonic state. In PE545 this state is approximately localised on the PEB<sub>50c</sub> bilin chromophore whereas in PC645 this state corresponds to the delocalised DBV<sub>+</sub> state of the DBV<sub>d-c</sub> dimer. Figure 3.3 displays the dynamics of exciton populations in the presence of quantum and classical vibration as well as the dynamics where the vibrational mode is completely absent. In the proceeding sections we highlight the features of these dynamics which are enhanced by the quantized vibration.

### 3.3 Quantum enhanced transport and directionality

In PE545 the resonant vibrational mode enhances the energy transported to the the accepting DBV<sub>a</sub> state (see shaded regions of Fig. 3.3a and inset). This is in

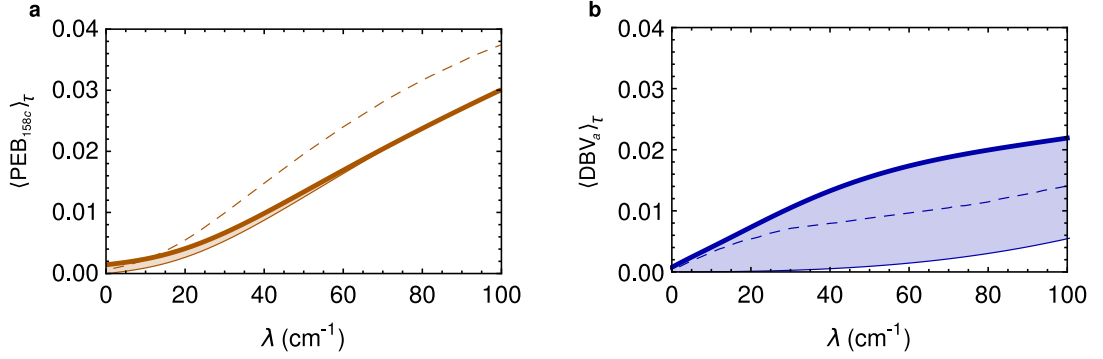


Figure 3.4: Integrated averages in PE545 for (a)  $\text{PEB}_{158c}$  and (b)  $\text{DBV}_a$  sites. The classical model predicts an enhancement of transport to *both* sites for all  $\lambda$ .

accordance with the principles identified in Chapter 2. The close resonance of the energy difference between PEB and DBV excitonic states with the frequency of the vibrational mode enables the transfer between exciton-vibration states with different phonon numbers. However, the classical model fails to predict the extent of this enhancement by half. In fact the classical model incorrectly predicts enhancement of transport to both  $\text{DBV}_a$  and  $\text{PEB}_{158c}$  exciton states. Therefore, in this system the ability of a vibrational mode to direct transport to a particular state is enhanced if the vibration is quantized. The enhanced directionality of transport is due to selective enhancement of transport between particular exciton states which the classical model for the vibration does not capture.

This is further illustrated by considering average exciton populations  $\langle \rho_{\alpha\alpha} \rangle_\tau = \frac{1}{\tau} \int_0^\tau \rho_{\alpha\alpha}(t) dt$ . As in Chapter 2 we consider averages over a timescale of  $\tau = 0.5$  ps. In Fig. 3.4a-b these averages are displayed for the  $\text{PEB}_{158c}$  and  $\text{DBV}_a$  exciton states of the PE545 subunit as a function of the strength of coupling to the thermal background  $\lambda$  with fixed  $\Omega_c = 100 \text{ cm}^{-1}$ . Without a vibrational mode present, transport due to the thermal background alone is predominantly to the energetically closer  $\text{PEB}_{158c}$  state. A quantum vibration enhances transport to the  $\text{DBV}_a$  state for all  $\lambda$  with little to no additional transport to the intermediate  $\text{PEB}_{158c}$ . In contrast the classical vibration predicts enhanced transport to both  $\text{PEB}_{158c}$  and  $\text{DBV}_a$  states. Therefore a quantized vibrational mode has an enhanced ability to direct transport to energetically distant states for a wide range of coupling to a thermal background  $\lambda$ . This additional ‘directionality’ of transport can be illustrated by considering vibration enhanced exciton transport  $\langle \overline{\rho_{\alpha\alpha}} \rangle_\tau = \langle \rho_{\alpha\alpha}^{\text{mode}} \rangle_\tau - \langle \rho_{\alpha\alpha}^{\text{no mode}} \rangle_\tau$  and the quantity

$$D = \frac{\langle \overline{\text{DBV}_a} \rangle_\tau}{\langle \overline{\text{DBV}_a} \rangle_\tau + \langle \overline{\text{PEB}_{158c}} \rangle_\tau}, \quad (3.4)$$

which measures the proportion of the total vibration enhanced transport to both  $\text{DBV}_a$  and  $\text{PEB}_{158c}$  sites, which is directed to the  $\text{DBV}_a$  exit bilin. Fig. 3.5 displays this quantity as a function of  $\lambda$  for both quantum and classical modes. The quantum and classical models for the mode both predict a similar degree of directionality for  $\lambda < 10 \text{ cm}^{-1}$ , but at larger  $\lambda$  while the quantized vibration continues to enhance transport towards the DBV state ( $D \rightarrow 1$ ) the classical vibration enhances transport more uniformly towards both sites ( $D \rightarrow 1/2$ ). In fact for the quantum vibration at biological noise strength  $\lambda = 100 \text{ cm}^{-1}$ ,  $D$  slightly exceeds unity because the transport to  $\text{DBV}_a$  is so great it suppresses the  $\text{PEB}_{158c}$  transport to below that observed when no vibrational mode is present *i.e.*  $\langle \overline{\text{PEB}_{158c}} \rangle_\tau < 0$ .

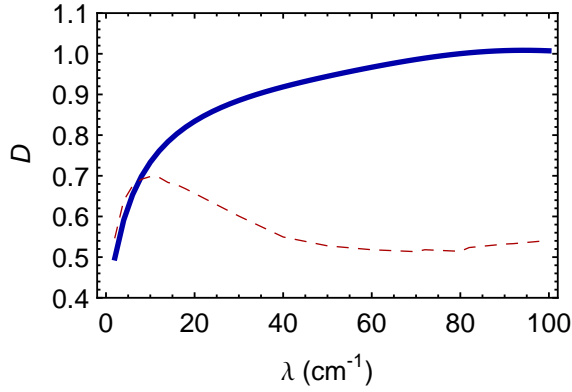


Figure 3.5: The directionality of exciton transport is enhanced with quantized vibrations. The quantity  $D$  in equation (3.4) is shown for quantized (solid) and classical (dashed) vibrational mode as a function of reorganisation energy  $\lambda$ .

### 3.4 Exciton population oscillations

In PC645 the resonant vibrational mode does not enhance transport to the accepting MBV state despite being close in energy to the  $\text{DBV}_+ \text{-MBV}_b$  exciton state energy difference. Instead, both quantized and classical vibrations result in population oscillations of the central DBV dimer exciton states (see Fig. 3.3b), an energy difference from which the vibration is seemingly far detuned. With classical vibrations the amplitude of these oscillations decays more rapidly than when a quantized vibration is used

Here a dimer model is utilized to demonstrate that it is the strong electronic

coupling of the DBV dimer which enables the detuned vibration to cause exciton population oscillations despite the detuning. This oscillatory energy transport cannot be predicted by incoherent (classical) transport models. The ‘wavelike’ transport of energy has been posited as a mechanism to enhance transport efficiency in photosynthetic complexes. Yet in the present system the transport to the accepting MBV state is not enhanced by these oscillations. In section 3.5 we propose an advantage of these oscillations in terms of the transient storage of energy within the vibrations. Since with a classical vibration these oscillations decay more rapidly this suggests another quantum enhanced feature of exciton dynamics: the transient energy storage in vibrational modes. These ideas are further explored in Chapter 4 where the energy exchange between vibrational and electronic degrees of freedom is investigated within a thermodynamical framework.

### 3.4.1 Quantum coherent exciton-vibration dynamics

For the high energy modes, the influence of electronic interaction strength  $V$  on the amplitude of exciton population oscillations can be predicted by considering a dimer system in the excitonic basis

$$H = \frac{\Delta E}{2} \tilde{\sigma}_z + \omega^{\text{vib}} b^\dagger b + \frac{g}{\sqrt{2}} [\tilde{\sigma}_z \cos(2\theta) - \tilde{\sigma}_x \sin(2\theta)] (b + b^\dagger), \quad (3.5)$$

where coupling between the exciton states with energies  $\pm\Delta E$  and the relative displacement (anti-correlated) vibrational mode is determined by the mixing angle  $\theta = (1/2) \arctan(2|V|/\Delta\epsilon)$ . The tilde over Pauli matrices serves to denote the exciton basis. The interaction  $\propto \tilde{\sigma}_z(b + b^\dagger)$  displaces the vibrational mode, but does not cause any transitions between exciton states. The interaction  $\propto \tilde{\sigma}_x(b + b^\dagger)$  is of Rabi type and if initially in the upper exciton state  $|+\rangle$ , (with energy  $+\Delta E/2$ ) the occupation probability of the state is well approximated by  $\rho_{++}(t) = \sum_n P(n) \frac{1}{\Omega_n^2} [\Delta^2 + 4g_0^2(n+1) \cos(\Omega_n t)]$ , where  $\Delta = \Delta E - \omega^{\text{vib}}$  denotes the detuning of the dimer exciton gap from the vibrational mode and  $\Omega_n = \sqrt{\Delta^2 + 4g_0^2(n+1)}$ .  $g_0 = g \sin(2\theta)/\sqrt{2}$ . Here the rotating wave approximation has been made, restricting this analysis to high energy modes. For a sufficiently high energy mode, the initial thermal distribution of phonons  $P_{\text{th}}(n) = (1 - \exp(-\beta\omega^{\text{vib}})) \exp(-\beta\omega^{\text{vib}}n)$  can be approximated by the  $n = 0$  term alone. There is then only one frequency  $\Omega_0$ , corresponding to the coherent exchange of one phonon between states  $|X, 0\rangle$  and

$|Y, 1\rangle$ . The amplitude  $A$  of oscillations between  $|X\rangle$  and  $|Y\rangle$  is given by

$$A = \frac{1}{1 + \left(\frac{\Delta}{2g \sin(2\theta)}\right)^2}. \quad (3.6)$$

Thus, a vibrational mode with detuning  $\sqrt{2}g \sin(2\theta)\sqrt{A^{-1} - 1}$  will produce exciton populations of amplitude  $A$ . Fig 3.6 shows this approximation as a function of

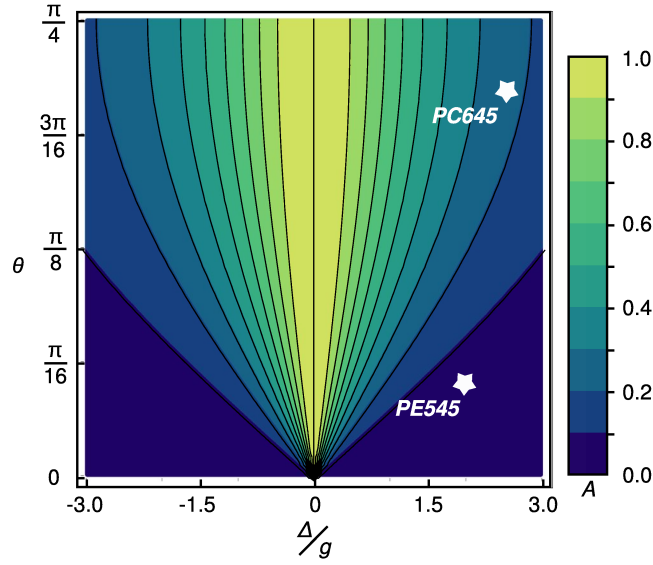


Figure 3.6: Amplitude  $A$  of exciton population oscillations in a exciton-vibration dimer as a function of mixing angle  $\theta$  and detuning of the mode  $\Delta$ . The parameters of the central dimers from PE545 and PC645 are marked.

mixing angle  $\theta$  and detuning  $\Delta$ . The parameters for the PEB<sub>50</sub> and DBV dimers from PE545 and PC645 respectively are marked. This approximation correctly anticipates that larger exciton population oscillations appear in the central dimer of the PC645 complex. Energy transport is not enhanced between the DBV and MBV<sub>b</sub> in PC645 despite a ‘close’ resonance of the vibrational mode of  $\Delta/g \approx 1.6$ . This can be understood in terms of the weak electronic coupling ( $V = 7.6 \text{ cm}^{-1}$ ), between the two sites which is one of the weakest in the subunit. In combination with the large site energy difference, the resulting small mixing angle results in no population transfer between the two states.

This insight will be convenient when attempting to identify features in the high energy region of a spectral density which may influence the energy transfer dynamics in a given system. The exclusion of irrelevant vibrational modes may allow for the study of larger, more complex systems. Other analytic expressions for the evolution

of a dimer interacting with a finite number of high energy modes [39, 183] may also be useful in this endeavour.

### 3.4.2 Classical exciton-vibration dynamics

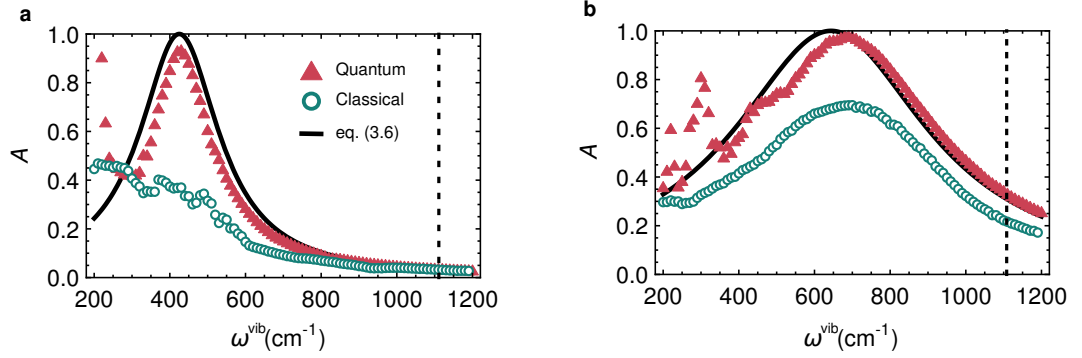


Figure 3.7: The amplitude of coherent exciton population oscillations as a function of the frequency of the vibrational mode for (a) the weakly electronically coupled ( $\theta \approx .22\pi/4$ )  $\text{PEB}_{50}$  dimer in PE545 and (b) the strongly electronically coupled ( $\theta \approx .92\pi/4$ ) DBV dimer in PC645.

High energy classical vibrations do not predict the correct amplitude of coherent exciton population oscillations. Fig. 3.7 shows the maximum population of  $\rho_{YY}(t)$  over 0.7 ps for the  $\text{PEB}_{50}$  and DBV dimers as a function of the mode frequency for both the quantum and classical models of the vibration. No thermal background or damping of the vibrations is included here. The approximation given by equation 3.6 is also displayed and agrees well with the quantum result for high energy vibrations ( $\omega^{\text{vib}} \gg 200 \text{ cm}^{-1}$ ).

The quantum results predict additional resonances when the frequency is an integer divisor of the energy gap. This corresponds to transitions between states like  $|X, 0\rangle$  and  $|X, n\rangle$ . Not only does the classical model underestimate the amplitude of the main resonance, these other resonances are absent.

In fact the coherent electronic dynamics predicted by the classical vibration are qualitatively different to the classical model. Fig. 3.8a shows the coherent exciton-vibration dynamics of the  $\text{PEB}_{50}$  dimer from PE545 for  $\omega^{\text{vib}} = 1110 \text{ cm}^{-1}$ . Although both classical and quantum models for the vibration predict the same maximum population of  $\rho_{YY}$  of about 0.03, the quantum exciton oscillations are dominated by one frequency corresponding to the energy difference between exciton-vibration eigenstates with character of  $|X, 0\rangle$  and  $|Y, 1\rangle$  as approximated by equation (2.4).



In contrast the classical vibrations predict many frequencies which display beating. Fig. 3.8b shows the exciton dynamics for the DBV dimer from PC645 with a lower energy mode of  $\omega^{\text{vib}} = 400 \text{ cm}^{-1}$ , for which a classical model for vibrations might be expected to be more accurate. With classical vibrations the oscillations rapidly collapse with a small revival  $\sim 0.5 \text{ ps}$ . The collapse in the classical model arises from the ensemble average over realizations. Each realization has exciton population oscillations of a slightly different frequency. When averaged these interfere and result in a collapse of oscillations. For lower energy vibrations, the initial distribution of  $X_{i,k}$  and  $P_{i,k}$  is broader and thus a wide variety of realizations contribute to the average which causes a more evident collapse. This illustrates that quantized vibrations enhance the duration of exciton populations.

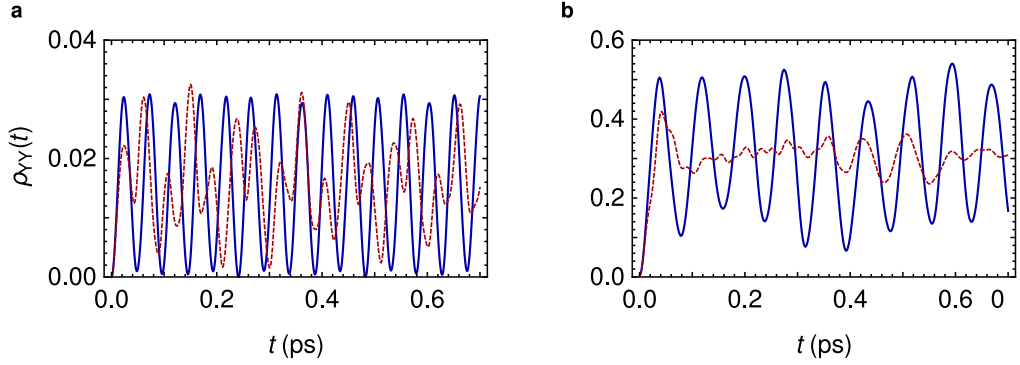


Figure 3.8: Evolution of exciton populations under coherent exciton-vibration dynamics with quantum (solid curve) and classical (dashed curve) vibrations. (a) PEB<sub>50</sub> dimer in PE545 with  $\omega^{\text{vib}} = 1110 \text{ cm}^{-1}$ , (b) DBV dimer in PC645 with  $\omega^{\text{vib}} = 400 \text{ cm}^{-1}$ .

### 3.4.3 Thermalisation of classical vibrations

The phenomenological damping of the classical mode does not produce the correct steady state for vibrations. The equation of motion of the expectation value  $\langle \ddot{X} \rangle$  for a quantum harmonic oscillator damped by the dissipator

$$\mathcal{D}\varrho = \Gamma(\bar{N} + 1) \left( b\varrho b^\dagger - \frac{1}{2} \{b^\dagger b, \varrho\} \right) + \Gamma\bar{N} \left( b^\dagger \varrho b - \frac{1}{2} \{bb^\dagger, \varrho\} \right), \quad (3.7)$$

where  $\bar{N} = (e^{\beta\omega^{\text{vib}}} - 1)^{-1}$  is given by  $\langle \ddot{X} \rangle = -((\omega^{\text{vib}})^2 + \Gamma^2/4)\langle X \rangle - \Gamma\langle \dot{X} \rangle$ . For weak damping ( $\Gamma \ll 2\omega$ ) this is identical to the equation of motion for the unforced classical oscillator given by equation (3.2) with  $g_{i,k}^{\text{vib}} = 0$ . The steady state energy ( $\omega\bar{N}$ ) of the quantum vibration is determined by the Heisenberg equa-

tion  $\langle \dot{E}_{\text{vib}} \rangle = -\Gamma(\langle E_{\text{vib}} \rangle - \omega \bar{N})$ . In the classical model, initial values for  $X$  and  $\dot{X}$  are drawn from a thermal distribution and the resulting trajectories averaged. This provides a consistent description of the initial thermal energy,  $\langle E_{\text{vib}} \rangle_{\text{ensemble}} = \langle (X^2 + \dot{X}^2/\omega^2)/4 \rangle_{\text{ensemble}}$  but as the damping acts, the system evolves towards a steady state

$$\langle \dot{E}_{\text{vib}} \rangle_{\text{ensemble}} = \left\langle -\frac{\Gamma}{2} \left( E_{\text{vib}} - \frac{X^2}{4} \right) \right\rangle_{\text{ensemble}} = 0 \quad (3.8)$$

which has zero energy and zero displacement. When forced by chromophore populations the steady state of the classical oscillator will be displaced and have non-zero energy but will still not account for thermal fluctuations. To reduce this effect we consider undamped vibrational modes  $\Gamma = 0$  for the calculations of energy storage in the next section.

### 3.5 Energy storage

Although exciton populations are present in PC645, they do not result in enhanced transport to acceptor states. However, quantized vibrations can support longer lasting oscillations than their classical counterpart and such oscillations are an indication that energy is exchanged and shared with vibrational degrees of freedom. Cyclical exchanges of energy with a vibrational mode, enables additional control on how absorbed energy is regulated, managed and distributed in a biomolecular system. While this does not necessarily influence the transport efficiency of excitons it may nevertheless be an important aspect of their function. In Chapter 2, it was noted that the dissipation of energy from an exciton-vibration system is transiently prevented whilst exciton population transfer is non-exponential. Here, we further explore the connection between oscillatory exciton transport and the transient storage of energy in vibrational modes and show that quantized vibrations have an enhanced ability to transiently store energy over classical vibrations.

We focus on the energy dynamics of the PC645 DBV dimer system and the vibrational mode with  $\omega^{\text{vib}} = 1108 \text{ cm}^{-1}$ . For a quantum description of vibrational modes we utilize the extended exciton-vibration system description of Chapter 2. This enables the calculation of the expectation values  $E_{\text{vib}}(t) = \text{Tr} [H_{\text{vib}} \rho_{\text{tot}}(t)]$  and  $E_{\text{ex-vib}}(t) = \text{Tr} [H_{\text{ex-vib}}(t) \rho_{\text{tot}}(t)]$  which are not accessible with a reduced description of electronic dynamics. The corresponding energies for the classical description of vibrations are the ensemble averages  $E_{\text{vib}}(t) = \langle (X^2 + \dot{X}^2/\omega^{\text{vib}})/4 \rangle_{\text{ensemble}}$  and  $E_{\text{ex}}(t) + E_{\text{ex-vib}}(t) = \langle \text{Tr} [H_{\text{ex}}^{\text{cl}}(t) \rho_{\text{ex}}(t)] \rangle_{\text{ensemble}}$ .

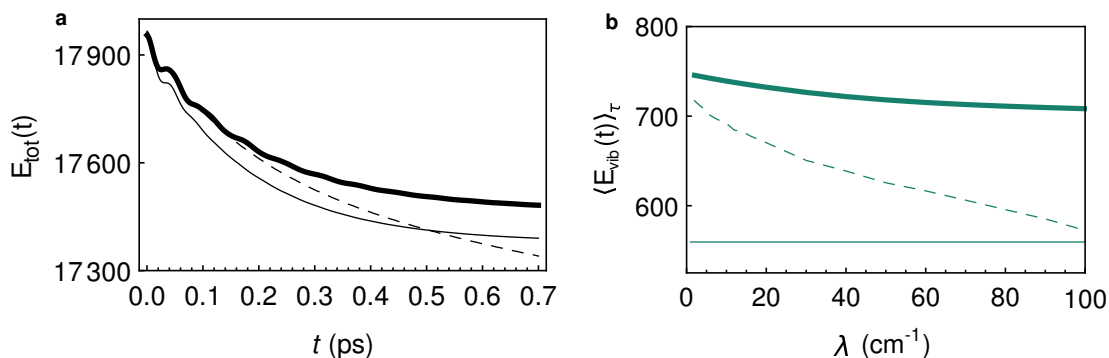


Figure 3.9: Energy storage in the DBV exciton-vibration dimer from PC645. **(a)** Dynamics of the total energy at  $\lambda = 100 \text{ cm}^{-1}$  and **(b)** Average energy stored in the vibrational mode over the time  $\tau = 0.5 \text{ ps}$  as a function of  $\lambda$ . Thick curves quantized vibrations dashed curves are classical vibrations. The thin curves indicate the case where the vibrations are not coupled to the electronic degrees of freedom and therefore remain in equilibrium.

Fig. 3.9a displays  $H_{\text{tot}}(t)$ , the dynamics of the energy of the total exciton-vibration system when the strength of interaction with the thermal background takes its biological value of  $\lambda = 100 \text{ cm}^{-1}$ . The quantized vibration (thick curve) delays the dissipation into the thermal background with respect to the case where coupling to the mode is zero (thin curve). The total energy is more oscillatory with the vibration present, implying more periods in which energy is extracted from the thermal background. This is more prominent when examining the derivative  $\langle \dot{H}_{\text{tot}} \rangle$  (not shown). These periods of increasing energy indicate that either work or heat is being extracted from the thermal background. In Chapter 4 a thermodynamical framework is applied to quantify the energy exchange change into heat and work-like components.

The classical vibration (dashed curve) quite accurately describes the energy dynamics for the first 0.2 ps, however at longer times the dissipation of energy is severely overestimated, even dropping below the energy of the case when the vibration remains in equilibrium. Fig. 3.9b displays the average energy stored in the vibration over the timescale  $\tau = 0.5 \text{ ps}$ ,  $\langle H_{\text{vib}} \rangle_{\tau}$  as a function of  $\lambda$ . The energy transiently stored in quantized vibrations is enhanced above the corresponding classical vibration. In particular for  $\lambda = 100 \text{ cm}^{-1}$  the average energy of the classical vibration is close to the case when the vibrations remain in equilibrium. This is related to the failure of the the classical model for vibrations to account for thermal fluctuations as discussed in section 3.4.3. Damping of vibrations  $\Gamma$  was neglected here, justified by the short 0.5 ps timescales which have been considered, Despite

this, indirect damping of the vibration from the thermal background causes the relaxation towards the incorrect steady state. The classical model for vibrations we have employed here does not adequately describe the exchange of energy with vibrations.

### 3.6 Concluding remarks and outlook

The quantum and classical models of vibrations investigated here have allowed us to identify features of the exciton dynamics in light harvesting systems which are enhanced by quantized vibrations. The use of classical models for vibrations are widespread. For example, the force fields entering molecular dynamics calculations are often calculated from molecular mechanics, which treats vibrations classically. Together, the results of this and the previous chapter highlight the breakdown of such an approximation. Classical physics is not adequate to describe the dynamics of energy transfer in these systems. The classical model employed here is not able to describe the influence of high or low energy vibrational modes. Quantized vibrations are more able to selectively enhance transport between exciton states, directing energy towards particular exit chromophores. The classical model also does not correctly predict the dependence of exciton population oscillations on electronic coupling strength and can spuriously predict the collapse of exciton population oscillations. Exciton population oscillations arise from the exchange of energy with vibrations and the storage of energy in vibrational motions is therefore enhanced when a quantized vibration is considered. Future work must utilize a classical model which properly accounts for thermal fluctuations. A classical description of vibrations supposes that the interaction drives a time dependence of electronic site energies. In the next chapter we find that this type of driving implies a work-like energy flux. It would seem that the degree to which a classical description of vibrations is appropriate also dictates the thermodynamic nature of energy fluxes in biomolecular systems.

Here we assumed that exciton-phonon interactions are the same for each chromophore. Recent studies which combine classical molecular dynamics and methods from quantum chemistry [40, 61–63] have revealed differences between chromophores for the continuous over-damped component as well as the under-damped vibrations of the spectral density. The influence of chromophore-dependent reorganisation energy in the continuous component on energy transfer dynamics has been investigated in dimer using the QUAPI method [184]. In ref. 40 we explored the impact of differ-

ences in both the continuous thermal bath and quantized vibrations for two relevant trimer subunits from PE545. We applied the quantum description of vibrational modes utilized in this chapter. In PEB chromophores, the reorganisation energy of the over-damped component of the spectral density is found to be smaller than in DBV chromophores. This reduces the transport to DBV exit chromophores, whilst increasing the effects of coherent exciton-vibration dynamics due to coupling of individual chromophores to vibrational modes of different frequencies. Such differences should be taken into account in future studies of exciton dynamics in light harvesting antenna as they will alter the spatio-temporal distribution of energy and may increase the relevance of coherent exciton-vibration dynamics for particular vibrations. A classical description of these vibrations may neglect quantum enhanced features of vibration-assisted excitation energy transport

### 3.A Electronic parameters of PE545 and PC645 subunits

	PEB <sub>50c</sub>	PEB <sub>50d</sub>	PEB158 <sub>c</sub>	DBV <sub>a</sub>
PEB <sub>50c</sub>	19450	71.7	-21.5	2.2
PEB <sub>50d</sub>	71.7	19050	-15.2	-39.3
PEB158 <sub>c</sub>	-21.5	-15.2	18800	-27.3
DBV <sub>a</sub>	2.2	-39.3	-27.3	18000

Table 3.A.1: Site energies (diagonals) and electronic couplings in the PE545 subunit [182].

	DBV <sub>d</sub>	DBV <sub>d</sub>	PCB <sub>158c</sub>	MBV <sub>b</sub>
DBV <sub>d</sub>	17113.9	319.374	30.4857	7.5811
DBV <sub>d</sub>	319.374	17033.3	20.3238	-43.8736
PCB <sub>158c</sub>	30.4857	20.3238	15807.4	3.3873
MBV <sub>b</sub>	7.5811	-43.8736	3.3873	16372.0

Table 3.A.2: Site energies (diagonals) and electronic couplings in the PC645 subunit [13, 58].

## Chapter 4

# Work exchange and the thermodynamic implications of non-equilibrium vibrations

*We study the exchange of energy between electronic and vibrational degrees of freedom in the light-harvesting antennae of cryptophyte algae. Inspired by recent work in the field of quantum thermodynamics, we utilize a formalism which defines heat and work fluxes between partitions of a quantum system which is out of thermal equilibrium. We find that the relative contribution of work-like and heat-like energy fluxes between chromophores and vibrational modes is dependent on the strength of electronic coupling between chromophores. With weak electronic coupling, the non-equilibrium dynamics of vibrations is a source of work whilst for strong electronic coupling vibrations act as a heat source. The structure of antenna thus determines the nature of energy exchange with vibrations. We also show that work fluxes persist even under continuous illumination, since vibrations are in non-equilibrium steady state. We envisage that these insights may guide the design of quantum technologies which exploit structured environments for their function.*

In Chapter 2 we illustrated that the exciton-vibration dynamics of a biologically relevant dimer prototype lead to non-exponential excitonic energy distribution whereby dissipation into a low-energy thermal bath can be transiently prevented. In Chapter 3 we showed that a particular classical model of vibrational motion does not describe the storage of energy in vibrations correctly. From this view, coherent vibrational motions that do not relax quickly and whose fluctuations cannot

be described classically may be seen as an internal quantum mechanism controlling energy distribution and storage. Further insights into the advantage of these non-trivial quantum behaviour may therefore be gained in a thermodynamic framework.

Quantum thermodynamics investigates concepts such as heat, work and entropy in quantum mechanical systems. A key objective within this nascent field is to extend ideas from equilibrium thermodynamics to the quantum regime with the necessary alterations or generalisations to avoid paradoxes or a violation of fundamental laws [185–187]. Advances in quantum technologies are such that it is feasible that experiments can now be performed to test these concepts [188]. Indeed the design of nano-mechanical devices may be guided by considerations arising from the study of quantum thermodynamics. Perhaps a greater understanding of the operation biomolecular systems can be gained from the perspective of quantum thermodynamics. Some species of purple bacteria are known to sacrifice photosynthetic efficiency in order to heat their local surroundings [189]. Quantum mechanical engines have been proposed which exploit quantum coherence to boost efficiency [190]. This has lead some to suggest that photosynthetic reaction centre operates as a quantum heat engine [104, 173]. Biomolecular systems operate far from equilibrium in the presence of significant thermal fluctuations. In this chapter we explore how work and heat can be defined when quantum mechanical systems are not in equilibrium and if this can provide new insight into the dynamics of biomolecular systems.

## 4.1 Energy fluxes in the quantum regime

The first law of thermodynamics states that the change of internal energy of a system in a time interval  $t \in [0, \tau]$  is the sum of the work done on, and heat added to the system in the same interval,

$$\Delta U = \Delta W + \Delta Q . \quad (4.1)$$

For a quantum system driven out of equilibrium by an external force, the mean change in internal energy is given by [191]

$$\Delta U = \langle H(\tau) \rangle - \langle H(0) \rangle \quad (4.2)$$

$$= \int_0^\tau dt \left\{ \text{Tr} \left[ \frac{dH(t)}{dt} \rho(t) \right] + \text{Tr} \left[ H(t) \frac{d\rho(t)}{dt} \right] \right\} . \quad (4.3)$$



The first energy flux appearing under the integral is defined as work flux  $\dot{W}(t) = \text{Tr}[\dot{H}(t)\rho(t)]$  and quantifies an external influence on the unitary dynamics of the system. If the system is autonomous (the Hamiltonian is time independent) then there is no work flux. The second energy flux  $\dot{Q}(t) = \text{Tr}[H(t)\dot{\rho}(t)]$ , is identified as a heat flux since it results in changes to the (von-Neumann) entropy of the system. If the system is closed but not autonomous (the Hamiltonian is time dependent), the change in internal energy results entirely from work flux and heat flux is absent. Clearly if the system is closed and autonomous there are no energy fluxes. In a general open, non-autonomous system both work and heat fluxes contribute to rate of internal energy changes of the system  $\dot{U} = \dot{W} + \dot{Q}$ .

### 4.1.1 Measurements

Measurement of the work done on a system in the time interval  $[0, \tau]$  requires experimental apparatus capable of measuring the energy at  $t = 0$  and  $t = \tau$ . If the driven Hamiltonian does not commute with itself at later times ( $[H(0), H(\tau)] \neq 0$ ) then the two observables are not compatible and cannot be measured with the same apparatus. Therefore, energy changes should be defined with respect to a local effective measurement basis (LEMBAS) which is determined by this apparatus. In what follows we will consider a LEMBAS comprising eigenstates of the undriven system. This is since the arbitrary division between system and environment is often guided by experimental accessibility. In the case of light harvesting complexes, despite overlapping signals, spectroscopic techniques can probe the dynamics of electronic eigenstates.

In practice, the influence of the two measurements at  $t = 0$  and  $t = \tau$  should be properly accounted for. The work must therefore be treated as a statistical quantity, which accounts for the back action of the measurements and not as a quantum observable [192]. For projective measurements of a system initially in thermal equilibrium, the statistics of a two time-measurement of work are determined by the two time correlation function  $G_\tau(u) = \langle e^{iuH(\tau)} e^{-iH(0)} \rangle$  which corresponds to the characteristic function of work. The  $n$ -th moment of work is given by  $(-i)^n \frac{d^n}{du^n} G_\tau(u)|_{u=0}$  and the corresponding probability distribution of work is obtained from

$$p(w) = \sum_{\alpha\beta} \delta[w - (E_{\beta\tau} - E_{\alpha 0})] \times |\langle \beta_\tau | U(\tau) | \alpha_0 \rangle|^2 \langle \alpha_0 | \rho(0) | \alpha_0 \rangle, \quad (4.4)$$

where  $|\alpha_t\rangle$  denotes the eigenstates of  $H(t)$  with corresponding eigenvalue  $E_{\alpha_t}$ . This distribution is of central importance in determining fluctuation relationships such

as the Jarzynski equality [35, 193]. The Jarzynski equality relates the mean exponentiated work  $\overline{e^{\beta w}} = \int p(w) e^{-\beta w} dw$  measured when a system initially in thermal equilibrium at temperature  $\beta$  is driven to an arbitrary non-equilibrium state to the free energy difference between the corresponding equilibrium states:

$$\overline{e^{\beta w}} = e^{-\beta \Delta F} . \quad (4.5)$$

In the remainder of this chapter the back-action of measurements has not been considered. This neglects an additional complexity which requires the specification of a precise experimental set-up. The issue of measurements in quantum mechanics is rarely straightforward and the discussion and debate surrounding the measurement of work statistics is spirited and ongoing [192, 194–197]. The outcome of these discussions will impact the direction of research into the function of biomolecular systems and may guide the design of quantum devices. Even if measurements do not take place, the division of the energy fluxes into heat and work is still meaningful and the exploration of these quantities adds a new dimension to the study of the dynamics of biomolecular systems, and open quantum systems in general.

## 4.2 Work and heat exchange between quantum systems

The time dependence of a Hamiltonian describes the effect of external forces on the system at hand. If the source of these forces is described quantum mechanically, with a total Hamiltonian  $H_T = H_S + H_D + H_{S-D}$ , which is partitioned into a reduced system S, a driving system D and the interaction between them S-D, then each part is time independent. This incorrectly suggests the system S is autonomous and therefore that there is no work flux between the system and its drive. Following [198], the effective master equation describing the local dynamics of the reduced system S is given by

$$\dot{\rho}_S(t) = -i [H_S + H_S^{\text{eff}}(t), \rho_S(t)] + \mathcal{L}_S^{\text{eff}} \rho_S(t) . \quad (4.6)$$

This identifies an effective driving of the reduced system which given by the effective Hamiltonian  $H_S^{\text{eff}}(t) = \text{Tr}_D [H_{S-D}(\mathbb{1}_S \otimes \varrho_D(t))]$  and an effective dissipator  $\mathcal{L}_S^{\text{eff}} \rho_S(t) = -i \text{Tr}_D [H_{S-D}, C_{S,D}(t)]$ . The effective Hamiltonian  $H_S^{\text{eff}}(t)$  determines the unitary contribution to the dynamics of the reduced system S due to the driving

system D. This effective time dependence results in a work flux into the system. For the general form of interaction  $H_{S-D} = \sum_{\alpha} A_{\alpha} \otimes B_{\alpha}$ ,  $H_S^{\text{eff}}(t) = \sum_{\alpha} A_{\alpha} \langle B_{\alpha}(t) \rangle$  and is therefore determined by the dynamics of observables of the driving system appearing in the interaction. The effective dissipator  $\mathcal{L}_S^{\text{eff}}$  arises from the build up of correlations between S and D ( $C_{S,D}(t) = \rho_T(t) - \rho_S(t) \otimes \varrho_D(t)$ ). This alters then (von-Neumann) entropy ( $\dot{S}_S = \text{Tr} [\dot{\rho}_S \log \rho_S] \neq 0$ ) and is thus associated with heat flows. Note that although equation (4.6) only explicitly replies on  $\rho_S$ , except in the very restricted case where the system and its drive remain approximately uncorrelated (the ‘factorisation approximation’ is valid [199]), the calculation of the effective dissipator  $\mathcal{L}_S^{\text{eff}}$  requires some knowledge of the dynamics of the driving system D.

The issue of measurement can be addressed by identifying the local effective measurement basis (LEMBAS) of system S. As discussed this depends on details of an experimental set-up. Here we assume the system and drive are defined such that there is an experimental set-up to measure in the eigenbasis of  $H_S$ . This implies the internal energy  $U_S(t) = H_S + H_S^{\text{eff},A}(t)$  is experimentally accessible. Here  $H_S^{\text{eff},A}(t)$  is the part of the effective time dependence  $H_S^{\text{eff}}(t)$  which commutes with  $H_S$  and can therefore be measured simultaneously. The associated work flux is given by

$$\dot{W}_S(t) = \text{Tr}_S [\dot{U}_S(t) \rho_S(t) - i[U_S(t), H_S^{\text{eff},B}(t)] \rho_S(t)] \quad (4.7)$$

where  $H_S^{\text{eff},B}(t)$  is the part of  $H_S^{\text{eff}}(t)$  which does not commute with  $H_S$ . The second term appears due to a unitary contribution from the  $\text{Tr} [U_S(t) \dot{\rho}(t)]$  ‘heat’ term in (4.3). It appears (to the experimenter) as work-like contribution to energy changes of S because it is not associated with changes in the von-Neumann entropy of the defined system S and therefore cannot be associated with heat flux. The heat flux is given by

$$\dot{Q}_S(t) = \text{Tr}_S [U_S(t) \mathcal{L}_S^{\text{eff}} \rho_S(t)]. \quad (4.8)$$

These definitions provide a classification of energy fluxes between the constituents of an autonomous quantum system which is undergoing non-equilibrium dynamics. Even if the total system is closed, one part of the system drives the other which manifests as a non-autonomous reduced system which features both heat and work energy fluxes. In the quantum regime the definitions of heat and work are dependent on the measurement basis. This is quite different to a dependence on the somewhat arbitrary division of the total autonomous system into its constituents. Of course, classically a different division will alter the measured heat and work but the nature of the energy changes will not be affected by measurement because there is no

restriction on what can be measured simultaneously. In the next section these definitions are applied to a dimeric system driven by a single vibrational mode.

### 4.3 Work and heat fluxes in an exciton-vibration dimer

To investigate the heat and work fluxes in a minimal model for a biomolecular system we consider an electronically coupled dimer system driven by a single vibrational mode. The total system is described by the Hamiltonian

$$H_T = \frac{\Delta\epsilon}{2}\sigma_z + J\sigma_x + \omega_{\text{vib}}b^\dagger b + g\sigma_z(b^\dagger + b), \quad (4.9)$$

which is equivalent to the exciton-vibration dimer (equation 2.1) considered in Chapter 2. We denote the electronic degrees of freedom as the reduced system S and the vibration as the driver D.

#### 4.3.1 Electronically uncoupled chromophores: ( $J = 0$ )

If the electronic coupling  $J$  is negligible, the effective system Hamiltonian is given by  $H_S^{\text{eff}}(t) = g\sigma_z\langle x(t) \rangle$ , which commutes with  $H_S = \frac{\Delta\epsilon}{2}\sigma_z$ . Thus all of the resulting energy changes of the system are accessible with measurements in the eigenbasis of  $H_S$ . The effective Hamiltonian of the vibrational mode is given by  $H_D^{\text{eff}}(t) = g\langle\sigma_z(t)\rangle(b + b^\dagger)$  and cannot be measured simultaneously with  $H_D = \omega_{\text{vib}}b^\dagger b$  (*i.e.*  $H_D^{\text{eff},A}(t) = 0$ ). For a system in the initially separable state  $\rho_T = \rho_S \otimes \varrho_D$  with  $\rho_S = c|X\rangle\langle X| + (1 - c)|Y\rangle\langle Y|$  and the vibrational mode in an arbitrary state with initial displacement  $x_0 = \text{Tr}[(b^\dagger + b)\varrho_D(0)]$ , the dynamics of the mode coordinate are given by

$$\langle x(t) \rangle = x_0 + \left( \frac{2g}{\omega_{\text{vib}}} (2c - 1) + x_0 \right) (\cos(\omega_{\text{vib}}t) - 1), \quad (4.10)$$

and the spin populations are conserved,  $\langle\sigma_z\rangle = (2c - 1)$ . Since  $H_S^{\text{eff},B}(t) = 0$ , the work flux into the reduced system is given entirely by the first part of equation (4.7)

$$\begin{aligned} \dot{W}_S &= \text{Tr}_S [\dot{H}_S^{\text{eff},A}(t)\rho_S(t)] = g\langle\sigma_z\rangle\langle\dot{x}(t)\rangle \\ &= -g(2g(2c - 1) + x_0\omega_{\text{vib}})\sin(\omega_{\text{vib}}t)(2c - 1). \end{aligned} \quad (4.11)$$

Conversely, for the vibration  $H_D^{\text{eff,A}}(t) = 0$  and thus the work flux into the vibration is given entirely by the second part of equation (4.7)

$$\dot{W}_D = -i\text{Tr}_D \left[ [H_D, H_D^{\text{eff,B}}(t)] \varrho_D \right] = -i\text{Tr}_D \left[ [H_D, g\langle\sigma_z\rangle(b^\dagger + b)] \varrho_D \right]. \quad (4.12)$$

By inserting the equation of motion for the displacement of the oscillator  $\langle\dot{x}(t)\rangle = i\langle[H_D, (b + b^\dagger)]\rangle$  we see that  $\dot{W}_S = -\dot{W}_D$ . This conservation of work flux is not a general feature and is only true if  $H_S^{\text{eff,B}}(t) = H_D^{\text{eff,A}}(t) = 0$ , *i.e.* the entire effective interaction of the driver with the system can be measured simultaneously with the system energy, while the effective interaction of the system with the driver *cannot* be measured simultaneously with the driver energy.

The heat flux into the system  $\dot{Q}_S = 0$ , since  $[H_S + H_S^{\text{eff,A}}(t), H_{S-D}] = 0$ . Therefore with zero electronic coupling, the vibrational mode acts as a perfect work source. Since  $[H_D, H_{S-D}] \neq 0$ , heat flux into the vibration is not necessarily zero. For a general mixed initial state of the system, the systems do not remain separable ( $C_{S-D} \neq 0$ ) thus there is a heat flux into the vibrational mode given by  $\dot{Q}_D = 8c(1-c)g^2 \sin(\omega_{\text{vib}}t)$ . So, from the perspective of the vibrational mode the system may act as both heat and work source simultaneously.

### 4.3.2 Electronically coupled chromophores: ( $J \neq 0$ ).

With finite electronic coupling there is in general no analytic solution for the heat and work fluxes therefore this case must be explored numerically. We have identified LEMBAS of electronic degrees of freedom as the excitonic states. Therefore there are two contributions to work flux in equation (4.7) which depend on the extent of exciton delocalisation. Expressed in the eigenstate basis of the electronic Hamiltonian defined by equation (2.2), the effective electronic Hamiltonian is  $H_{\text{el}}^{\text{eff}}(t) = g\langle x(t)\rangle U\sigma_z U^\dagger = g\langle x(t)\rangle [\tilde{\sigma}_z \cos(2\theta) - \tilde{\sigma}_x \sin(2\theta)]$ . This defines the commuting and non-commuting parts  $H_{\text{el}}^{\text{eff,A}}(t) = g\cos(2\theta)\langle x(t)\rangle\tilde{\sigma}_z$  and  $H_{\text{el}}^{\text{eff,B}}(t) = -g\sin(2\theta)\langle x(t)\rangle\tilde{\sigma}_x$  respectively. The work flux is given by

$$\dot{W}_{\text{el}} = g\cos(2\theta)\langle\dot{x}\rangle\langle\tilde{\sigma}_z\rangle - 2g\sin(2\theta)\langle x\rangle \left( \frac{\Delta E}{2} + g\cos(2\theta)\langle x\rangle \right) \langle\tilde{\sigma}_y\rangle \quad (4.13)$$

where the first term arises from  $\langle\dot{H}_{\text{el}}^{\text{eff,A}}\rangle$  and is proportional to the exciton population difference while the second contribution arises from the commutator of the measurable and unmeasurable effective system Hamiltonian and is proportional to

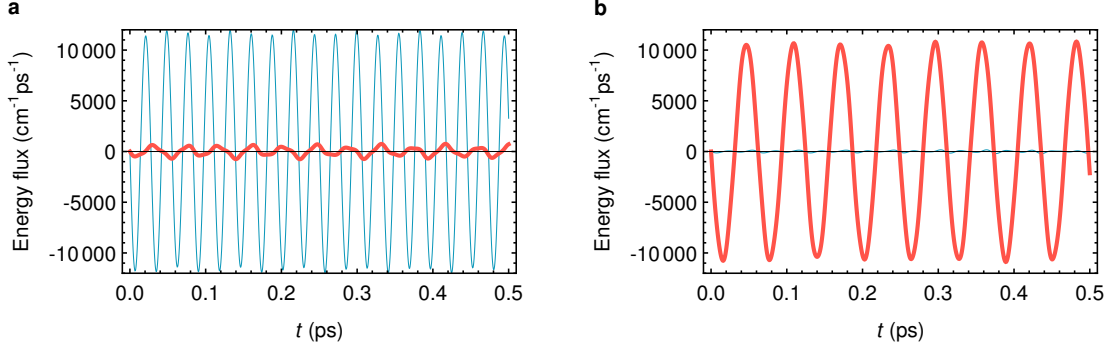


Figure 4.1: Work (thin blue curve) and heat (thick red curve) fluxes in isolated exciton-vibration dimers. (a) the weakly electronically coupled PEB<sub>50</sub> dimer in PE545 and (b) the strongly electronically coupled DBV dimer in PC645.

inter-exciton coherences. The heat flux

$$\dot{Q}_{\text{el}} = -2g \sin(2\theta) \left( \frac{\Delta E}{2} + g \cos(2\theta) \langle x \rangle \right) [\langle \tilde{\sigma}_y x \rangle - \langle \tilde{\sigma}_y \rangle \langle x \rangle] \quad (4.14)$$

requires a degree of correlation (co-variance) between exciton coherences and displacement of the vibration.

In the limit of strong electronic coupling  $\theta \rightarrow \pi/4$ , the effective energy changes due to the interaction with the vibration cannot be measured ( $H_{\text{el}}^{\text{eff},A} = 0$ ) so that the first term contributing to the work flux vanishes. The second term also vanishes if there is no displacement of the vibration or inter-exciton coherences. In the limit where the interaction is fully  $g\tilde{\sigma}_x(b + b^\dagger)$ , an initial state without a displacement or excitonic coherences will not gain either at later times. Although the vibration does not perform work on the electronic degrees of freedom, there is a heat flux due to the coherent transitions between the  $|X, n\rangle$  and  $|Y, n + 1\rangle$  exciton-vibration states. In this limit it is possible for the vibration to act as a perfect heat source or sink.

For general coupling strengths  $J$ ,  $g$  and mode frequency  $\omega_{\text{vib}}$ , analytic expressions for dynamics of *e.g.*  $\langle x(t) \rangle$  are unknown but quite apparently the vibration can act as work and heat source simultaneously. Fig. 4.1 displays the numerically calculated heat and work fluxes into the electronic degrees of freedom for central dimers from PE545 and PC645 respectively. The initial state is as usual, a thermal state for the vibration and the highest energy exciton state for the chromophores. Since the dynamics of these isolated exciton-vibration dimers is periodic, over any cycle the net fluxes are zero. This is not representative of an important qualitative difference between the two prototypes. Quite apparently, the vibration behaves as a work source for the weakly coupled PEB<sub>50</sub> dimer, and almost entirely a heat source for the

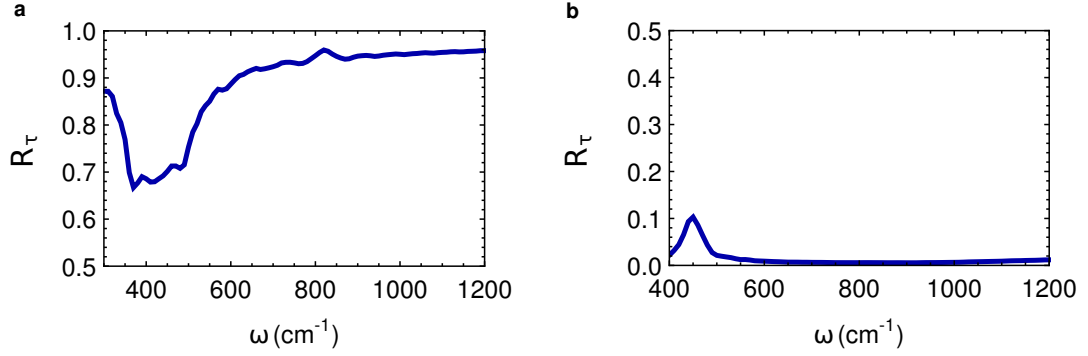


Figure 4.2: Work source quality  $\mathcal{R}_\tau$  as a function of the vibration frequency for (a) the weakly electronically coupled PEB<sub>50</sub> dimer in PE545 and (b) the strongly electronically coupled DBV dimer in PC645.

strongly coupled DBV dimer. This is consistent with the dependence on electronic coupling identified from expressions (4.13) and (4.14).

### 4.3.3 Work source quality

If the net heat or work flux through a system in a time interval  $\tau$  is zero, this does not exclude the possibility that large amounts of heat and work have passed through the system during that period. To evaluate work source quality, rather than compute net fluxes like  $\int_0^\tau \dot{W}(t) dt$  we utilize the measure introduced by Schöder et al [198]

$$\mathcal{R}_\tau = \frac{\int_0^\tau |\dot{W}(t)| dt}{\int_0^\tau |\dot{W}(t)| dt + \int_0^\tau |\dot{Q}(t)| dt} . \quad (4.15)$$

Since this measure is based on the absolute values of fluxes, it allows a stronger quantification of work source quality. Values approaching  $\mathcal{R} = 1$  imply that energy changes during time  $\tau$ , are dominated by work like fluxes. Conversely values approaching  $\mathcal{R} = 0$  imply heat fluxes dominate and that the driving system acts more as a heat source or sink.

Fig. 4.2 displays the work source quality measure  $\mathcal{R}_\tau$  for the PE545 and PC645 dimers as a function of  $\omega_{\text{vib}}$ . The noisy features in both curves arise due to the fixed time window of consideration  $\tau = 0.5$  ps. As  $\omega_{\text{vib}}$  is altered the number of oscillations of heat and work fluxes lying within the window does not change smoothly resulting jumps in the work source quality in this time interval.

The weakly electronically coupled PE545 dimer acts as a work source except near  $\omega_{\text{vib}} = 400 \text{ cm}^{-1}$  which corresponds to the exciton energy gap. As has been discussed in previous chapters, transfer between exciton states due to quasi-

resonance with a vibrational mode is accompanied by the generation of inter-exciton coherences  $\rho_{Xn,Yn}$  which contribute to  $\langle \tilde{\sigma}_y \rangle$  as well as exciton-vibration coherences  $\rho_{Xn,Ym}$  which contribute to  $\langle \tilde{\sigma}_y x \rangle$ . Therefore the reduction in work source quality which occurs on resonance arises due to the additional heat flux as excitonic and vibrational degrees of freedom become correlated.

In the strongly coupled DBV dimer from PC645 the vibration acts as a heat source over a wide range of frequencies. The correlations between excitonic and vibration degrees of freedom dominate except near  $\omega_{\text{vib}} = 450 \text{ cm}^{-1}$ . This does not correspond to an integer divisor of exciton energy gap but was identified in the amplitude of exciton populations in Fig. 3.7b and attributed to a resonance between exciton-vibration states. The details of this resonance have not been fully explored but at this frequency excitonic coherences are enhanced with a concomitant reduction of exciton-vibration correlations. The heat flux is therefore decreased and the the work flux term proportional to excitonic coherences increased.

## 4.4 Work exchange with structured environments

For an electronic system coupled to a structured environment, there are work and heat fluxes due to localised modes as well as the continuous thermal background. The previous section considered a minimal system of two chromophores subject to a single vibrational mode. Here this model is extended to the tetrameric units from PE545 and PC645 considered in Chapter 3, considering a structured vibrational environment consisting of a Drude continuum and an underdamped vibrational mode. The effective Hamiltonian for an  $N$  chromophore complex is given by

$$H_{\text{el}}^{\text{eff}}(t) = \sum_i \sigma_i^+ \sigma_i^- \left\langle \sum_k g_{i,k} (b_{ik} + b_{ik}^\dagger) \right\rangle_t = \sum_{\alpha\beta} \sigma_\alpha^+ \sigma_\beta^- \sum_i C_i^\alpha (C_i^\beta)^* X_i(t), \quad (4.16)$$

where the identified LEMBAS (the exciton basis) determines that  $H_{\text{el}}^{\text{eff,A}}(t)$ , depends on the participation of site  $i$  to exciton  $\alpha$   $|C_i^\alpha|^2$ , whereas  $H_{\text{el}}^{\text{eff,B}}(t)$  is determined by ‘exciton interferences’  $C_i^\alpha (C_i^\beta)^*$ . Work flux into the electronic system is given by

$$\dot{W}_{\text{el}}(t) = \sum_\alpha \rho_{\alpha\alpha}(t) \dot{X}_{\alpha\alpha}(t) - \sum_{\alpha \neq \beta} \Im(\rho_{\alpha\beta}(t)) [E_{\alpha\beta} + (X_{\alpha\alpha}(t) - X_{\beta\beta}(t))] X_{\alpha\beta}(t), \quad (4.17)$$

where  $X_{\alpha\beta}(t) = \sum_i C_i^\alpha (C_i^\beta)^* X_i(t)$ . This partitioning of work flux into contributions from exciton populations and coherences extends the result of equation (4.13) to  $N$  sites.



### 4.4.1 Calculating bath observables within the open systems approach

The general spirit of the open systems approach to calculating system dynamics is to trace away and discard information about bath degrees of freedom. It is nevertheless possible to simultaneously calculate observables of the bath. In the case of hierarchical expansions, Zhu *et al.* [200] recently demonstrated that moments of collective bath coordinates

$$X_i^{(n)}(t) = \left\langle \left( \sum_k g_{i,k} (b_{ik} + b_{ik}^\dagger) \right)^n \right\rangle_t, \quad (4.18)$$

are contained in the auxiliary matrices. Work fluxes are determined by the first moment of the environment at each site which is contained within auxiliary matrices in the first tier of the hierarchy:  $X_i(t) = -\text{Tr} [\sum_{(\sum_k n_{ik}=1)} \rho_{\mathbf{n}}(t)]$ . For a structured environment with a correlation function expressed as a sum of Drude and under-damped Brownian oscillator contributions, the individual displacements can be extracted by summing the auxiliary matrices of the corresponding coefficients appearing in exponential decomposition of the bath correlation function  $C_i(t) = \sum_k c_{ik} \exp(-\nu_{ik}t)$ . In this case the auxiliary matrices corresponding to the Matsubara terms from each component should not be combined. If the hierarchy of equations has been rescaled for numerical purposes, the auxiliary matrices must be transformed to their unscaled versions in order to extract the physical  $X_i^{(n)}(t)$ 's.

### 4.4.2 Work and heat fluxes in a tetrameric system

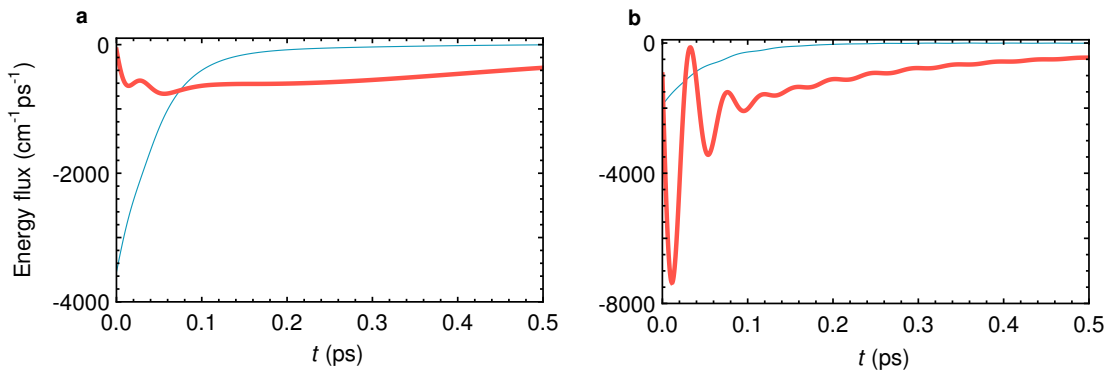


Figure 4.3: Work (thin blue) and heat (thick red) fluxes in (a) PE545 and (b) PC645 tetramic units subject to an unstructured environment described by a Drude spectral density with  $\lambda = 100 \text{ cm}^{-1}$  and  $\Omega_c = 100 \text{ cm}^{-1}$ .

For an  $N$  site system coupled to an arbitrarily structured vibrational environment, the system work flux can be extracted from the auxiliary matrices appearing in the hierarchical expansion of system dynamics. The corresponding heat flux can be determined through energy conservation:  $\dot{Q}_{\text{el}}(t) = \dot{U}(t)_{\text{el}} - \dot{W}_{\text{el}}(t)$ . The dynamics of the work and heat fluxes in the PE545 and PC645 tetramer units when an under-damped vibration is not present are displayed in Fig. 4.3a-b. In both systems the fluxes are negative at all times. As the electronic system dissipates energy into the background in the form of both heat and work.

The heat flux is initially zero but as the electronic and vibrational degrees of freedom become correlated, the electronic system heats the vibrational environment. In both systems it displays oscillations which decays on the same timescale as excitonic coherences. In PC645 the maximum heat flux is larger, consistent with the results in the dimer prototypes.

The work flux decays monotonically from an initial maximum determined by an initial velocity of the bath - as given by the first term in equation (4.17). A finite initial velocity is not consistent with a thermal initial state and is an artifact arising from the coarse-grained nature of the Drude-form correlation function describing the unstructured environment. In particular  $d\Re C(t)/dt|_{t=0}$  and  $\Im C(0)$  should vanish by definition but are non-zero for the Drude bath correlation function. These limitations of the Drude form for an over-damped Brownian oscillator have been highlighted previously [79] and mean that very short time dynamics are inaccurate. Fig. 4.4a-b compares bath velocities in a dimer when the full form for the Brownian oscillator correlation function to the velocities when the approximate Drude form is used. When the full form is used the velocities are correctly zero at  $t = 0$ , rising sharply on a timescale  $\nu^{-1} \approx \gamma^{-1}$  to the values predicted by the Drude form. Fig. 4.4c displays  $\Im C(t)$  for the two forms of correlation function. When considering integrals of work fluxes the additional initial contribution arising from the Drude form of the correlation function is negligible.

The addition of a discrete vibrational mode to the environment distinctly alters the features of heat and work fluxes in both systems as shown in Fig. 4.5. In both systems the work flux now oscillates such that there are periods of time when the system work flux is positive- the environment performs work on the electronic degrees of freedom. This is accompanied by a decay of the envelope of work which is slower than the case where a vibration is not present. In PE545 the additional energy flux through the electronic system due to the vibrational mode is predominantly work-like, whereas in PC645 the energy flux has a significant heat-like component.

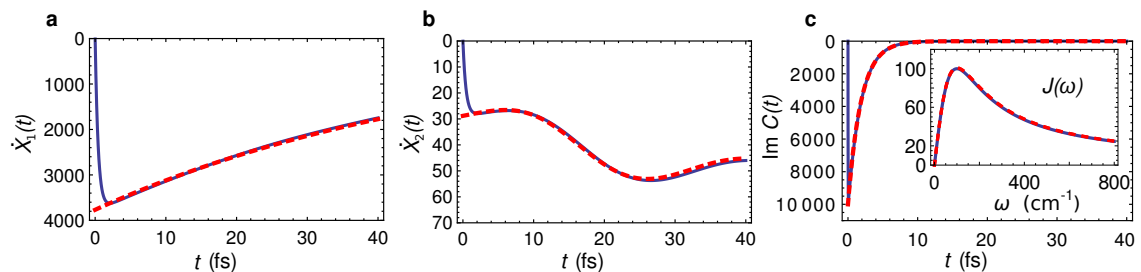


Figure 4.4: **(a-b)** Short time evolution of the velocities of generalized bath coordinates  $\dot{X}_i(t)$  in a dimer system subject to an over-damped Brownian oscillator  $\gamma > 2\omega_{\text{vib}}$  (solid blue) and corresponding Drude approximation (Dashed red). **(c)** The imaginary part of the correlation functions  $C(t)$  corresponding to these two types and (inset) the spectral densities.

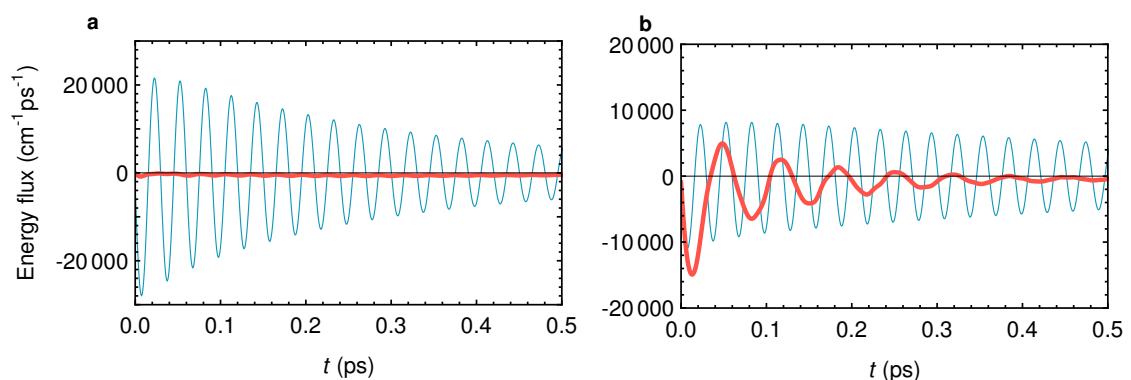


Figure 4.5: Work (thin blue) and heat (thick red) fluxes in **(a)** PE545 and **(b)** PC645 tetramic units. The structured environments described by discrete oscillator as in Chapter 3.

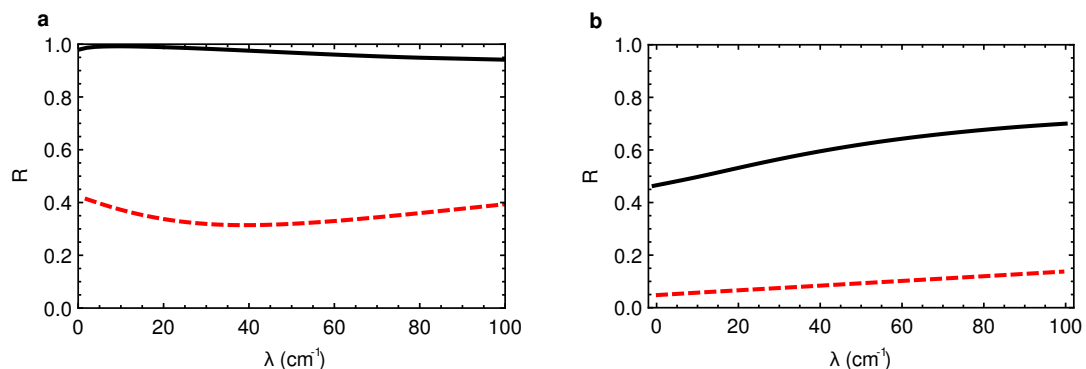


Figure 4.6: Work source quality  $\mathcal{R}_\tau$  as a function of reorganisation energy  $\lambda$  for (a) PE545 (b) PC645 tetramic units. Dashed curves are for an unstructured environment while solid curves include an underdamped vibration.

This is consistent with the findings in the dimer systems and suggests an alternative interpretation of the role of the vibrations beyond tuning the spatio-temporal distribution of electronic excitation energy which has been identified in previous chapters. Vibrational modes also provide a mechanism to alter the nature of energy fluxes between electronic system and vibrational environment.

In Chapter 3 a vibration present in PE545 was found to direct transport to the lower energy exit site. Here we find that this vibration increases the work source quality of the vibrational environment. In PC645, the same vibration was not found to enhance transport. Instead it introduces exciton population oscillations between states of the central dimer. This signifies the coherent exchange of energy between exciton and discrete vibrations. Here we have been able to identify this energy flux with heat. The oscillating exciton-vibration correlations result in periods of time in which the system is being heated ( $\dot{Q}_{\text{el}} > 0$ ) which are not observed with an unstructured environment.

To investigate the role of the strength of the thermal background Fig. 4.6 shows the work source quality the two systems with and without a vibrational mode as a function of the reorganisation energy  $\lambda$ . As reorganisation energy increases the coupling to each vibrational mode of the continuum is proportionally increased. For the weakly electronically coupled sites this causes larger displacements of the local vibrational modes and contributes more to the work flux between the electronic system and environment. For strongly electronically coupled sites or those in close quasi-resonance with a discrete vibration this increases the heat flux between electronic system and environment. In PE545 the vibrational modes increase the work source quality  $\mathcal{R}_\tau$  from  $\sim 0.4$  to close to unity for a wide range of reorganisation

energy with a maximum at  $\lambda = 20 \text{ cm}^{-1}$ . This does not correspond to the biological strength currently identified, however there is evidence from mixed quantum classical molecular dynamics simulations that the reorganisation energies of some pigments within antennae can be of this order [40, 61–63]. In PC645 a wide range of vibrational modes are in resonance with central DBV dimer. The heat flux between this dimer and local vibrations was identified in the model of section 4.3.2. However, vibrations at other sites with weak electronic coupling serve to increase work fluxes so that overall effect of the discrete vibration is an increase of  $\mathcal{R}_\tau$  to  $\sim 0.7$ .

## 4.5 Work exchange under continuous illumination

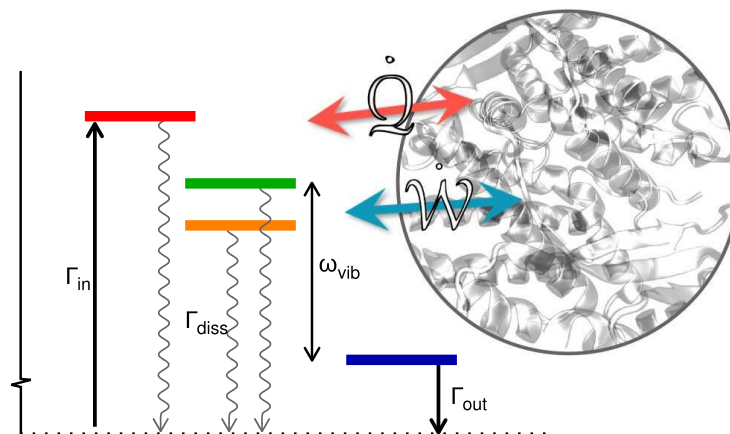


Figure 4.7: Schematic of a light harvesting antenna operating under continuous illumination. Electronic energy levels are of the PE545 subunit as shown in Fig. 3.2. The highest energy exciton state is populated at rate  $\Gamma_{\text{in}}$ , and trapping occurs at the lowest exciton at rate  $\Gamma_{\text{out}}$ .

We have thus far considered energy transfer from a transient perspective, by examining the the dynamics of the energy absorbed by high energy pigments as it transfers to low energy exit chromophores. A complementary picture is to consider the steady-state operation of light harvesting biomolecules which are subject to the continuous input of excitation energy though illumination, and loss channels which describe the recombination and trapping of excitons. An equivalence of these approaches has been demonstrated for the evaluation of certain dynamical properties - namely the quantum yield [201]. The quantum yield is the probability that absorbed energy reaches a desired trapping site. This trapping describes the irreversible transfer of the energy to a reaction centre or another antenna system.

Here we investigate thermodynamic aspects of the dynamics of biomolecules under steady-state operation. The incoherent input, output and dissipation of excitations is described by additional incoherent dissipative terms appearing in the master equation for the excitonic degrees of freedom

$$\dot{\rho}_S(t) = -i [H_S + H_S^{\text{eff}}(t), \rho_S(t)] + (\mathcal{L}_S^{\text{eff}} + \mathcal{L}_{\text{in}} + \mathcal{L}_{\text{diss}} + \mathcal{L}_{\text{out}}) \rho_S(t) . \quad (4.19)$$

Here  $\mathcal{L}_{\text{in/out}}$  are the usual Lindbladian dissipators of the standard form  $\mathcal{L}\rho = \sum_{\alpha} \Gamma [A_{\alpha}\rho A_{\alpha}^{\dagger} - \frac{1}{2}\{A_{\alpha}^{\dagger}A_{\alpha}, \rho\}]$ , which describes incoherent excitation (de-excitation) of excitonic degrees of freedom at rates  $\Gamma_{\text{in}}(\Gamma_{\text{out}})$  with operators  $A_{\alpha} = \sigma_{\alpha}^{+}(\sigma_{\alpha}^{-})$ . A description of coupling to the radiation field [84, 111], results in the slow incoherent input of energy via transitions from ground to excited excitonic states. The rates at which these transitions take place  $\Gamma_{\text{in}}$ , are proportional to the oscillator strengths of the excitonic states which are in turn determined by the orientation of dipole moments in the system. In both PE545 and PE545 the dipole orientations are such that the highest energy exciton states have finite oscillator strength and could therefore be selectively populated in an experiment. For consistency with the transient picture in which the highest energy exciton state is initial populated, a rate of  $\Gamma_{\text{in}} = 0.01 \text{ cm}^{-1} \approx (0.5 \text{ ns})^{-1}$  is considered to populate the highest energy exciton state only. The  $\mathcal{L}_{\text{diss}}$  Liouvillian describes undesirable loss channel representing the fluorescence/recombination at individual chromophores at rates  $\Gamma_{\text{diss}} = (1 \text{ ns})^{-1}$ . Trapping of the excitation is considered to take place at the lowest energy exciton state at a rate  $\Gamma_{\text{out}} = 0.5 \text{ ps}$ . This desirable energy output channel describes the irreversible transfer of the energy to an adjacent complex or reaction centre.

In this chapter we adopted the exciton eigenstates as the local effective measurement basis, therefore measurements of  $U_S(t) = H_S + H_S^{\text{eff},A}(t)$  are possible. Once the system has reached the steady state  $\rho_S(t_s)$ , the measurable system energy is stationary

$$\dot{U}_S = \dot{W}_S + \dot{Q}_S + \dot{Q}_{\text{in}} + \dot{Q}_{\text{diss}} + \dot{Q}_{\text{out}} = 0 . \quad (4.20)$$

The heat-like energy fluxes  $\dot{Q} = \text{Tr}_S[U_S(t_s)\mathcal{L}\rho_S(t_s)]$  are associated with each of the four dissipative terms in (4.19). It is natural to define an efficiency  $\eta = |\dot{Q}_{\text{in}}|/|\dot{Q}_{\text{out}}|$ , the fraction of energy entering the system from the radiation field which exits through the trapping states. This is given by

$$\eta = \frac{\sum_{\alpha} \Gamma_{\text{out}}^{(\alpha)} [E_{\alpha} + X_{\alpha\alpha}(t_s)] \langle \alpha | \rho_S(t_s) | \alpha \rangle}{\sum_{\alpha} \Gamma_{\text{in}}^{(\alpha)} [E_{\alpha} + X_{\alpha\alpha}(t_s)] \langle 0 | \rho_S(t_s) | 0 \rangle} , \quad (4.21)$$

and depends on the steady state occupations of the ground state and trapping exciton states as well as the steady state displacement of the corresponding collective vibrations. Environmental vibrational modes mainly influence this quantity by altering the steady state populations of excitonic states. For the low rates of exciton input considered here the steady state displacements  $X_{\alpha\alpha}(t_s)$  are generally small relative to the energies of excitonic states  $E_\alpha$  and therefore have little influence via this factor. In the steady state, the work-like energy flux is given by

$$\dot{\mathcal{W}}_S = -i\text{Tr}_S[U_S(t_s), H_S^{\text{eff},B}(t_s)]\rho_S(t_s) \quad (4.22)$$

$$= - \sum_{\alpha \neq \beta} \Im(\rho_{\alpha\beta}(t)) [E_{\alpha\beta} + (X_{\alpha\alpha}(t) - X_{\beta\beta}(t))] X_{\alpha\beta}(t). \quad (4.23)$$

which requires both inter-exciton coherences and an environment that is in a displaced steady state.

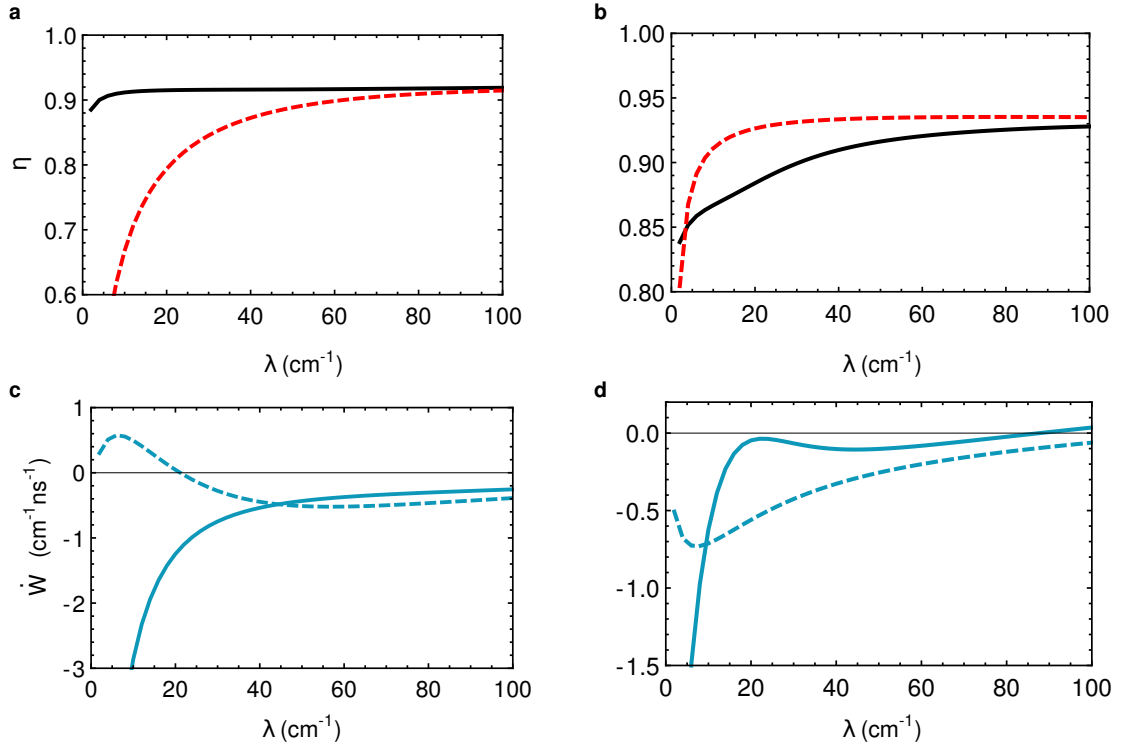


Figure 4.8: Efficiency  $\eta$  as a function of bath reorganisation energy in (a) PE545 and (b) PC645. The corresponding work flux  $\dot{\mathcal{W}}_S$  in (c) PE545 and (d) PC645. Dashed curves are for an unstructured environment while solid curves include an underdamped vibration.

Figure 4.8 displays  $\eta$  and  $\dot{\mathcal{W}}_S$  for the PE545 and PC645 tetramic systems with and without vibrational modes. In PE545 the vibrational mode enhances the efficiency

although at biological reorganisation energies ( $\lambda \sim 100 \text{ cm}^{-1}$ ) the enhancement is less than a percent. In PC645 the vibration inhibits the efficiency but again at biological reorganisation energies the difference in efficiency is around a percentage. As discussed, there is evidence that the local environments of some chromophores may feature reduced reorganisation energies. In this case efficiencies under continuous illumination in these systems would be more dependent on the presence of vibrations. The steady state work flux  $\dot{W}_S$  due to the environment behaves differently as a function of reorganisation energy depending on the presence of a discrete vibrational mode. In both cases the amplitude is small in comparison with the heat fluxes through the system. It therefore does not contribute directly to the input-output efficiency of the antenna. This work flux may serve an alternative function in these systems which has yet to be identified. The amplitude of work fluxes in PE545 are larger than in PC645. This is consistent the weakly coupled PE545 being the superior work source in the transient setting. At lower reorganisation energies, the amplitude of work flux is large if a discrete vibration is included. As reorganisation energies increases this indirectly damps the motion of the discrete vibration, which reduces the work fluxes. In fact, at biological reorganisation energies the amplitude of work flux is reduced by the vibrational mode in both systems. By inspecting equation (4.23), the presence of a non-zero work flux is a clear indicator that both steady state inter-exciton coherences and a displaced vibrational state is present in the system.

If the input rate  $\Gamma_{\text{in}}$  is increased, the steady state of the electronic degrees of freedom shifts further from a state which is diagonal in the exciton basis. Additionally the vibrations are driven further from equilibrium. Figure 4.9a-b shows the work flux in both systems over several orders of magnitude of  $\Gamma_{\text{in}}$  with the bath reorganisation energy fixed at  $\lambda = 100 \text{ cm}^{-1}$ . Correspondingly in Fig. 4.9c-d we construct the measure  $\sum_i |X_i(t_s)|$ . This serves to quantify the extent to which the local environments of all chromophores are displaced. Notice that if this measure is zero, then all  $X_{\alpha\beta} = 0$ . The insets of Fig. 4.9c-d display the efficiency  $\eta$  over the same rate and indicate that it is insensitive to the input rate.

For low rates of excitation input the amplitude of work flux is small and vibrations are not shifted as far from equilibrium. At large rates of excitation input, the work flux and environmental displacement saturates since energy arrives faster than the rate of excitation trapping  $\Gamma_{\text{out}} = 0.5 \text{ ps}^{-1} \approx 10 \text{ cm}^{-1}$ . This limitation on the time scale of system dynamics means the extra energy cannot cause additional displacement of the environment. Even higher rates of excitation input are not con-



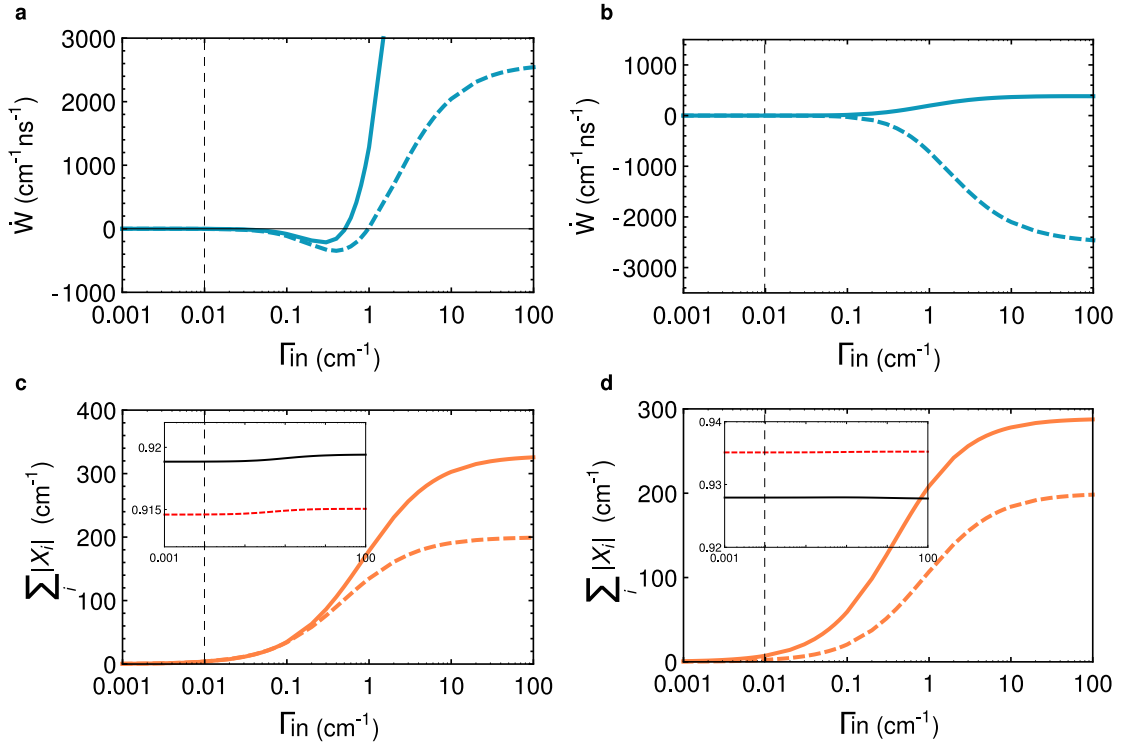


Figure 4.9: The work fluxes  $\dot{W}_S$  under steady state operation as a function of the input rate  $\Gamma_{\text{in}}$  in (a) PE545 and (b) PC645. (c) The measure of steady state environmental displacement  $\sum_i |X_i|$  in PE545 and (d) PC645. In insets show the efficiency  $\eta$  over the same range of  $\Gamma_{\text{in}}$ . Dashed curves are for an unstructured environment while solid curves include an under-damped vibration.

sidered as doubly excited electronic states are not accounted for within the current model. In this regime both systems feature a larger environmental displacement when a discrete vibrational mode is present. Counter-intuitively the amplitude of work flux in PC645 is reduced when a vibration is present. Since we consider measurements to be in the exciton basis, the resulting work flux (equation (4.23)) is partially determined by the non-local collective displacements  $X_{\alpha\beta}$ . Whilst the amplitude of these terms is increased by displacement of local oscillators  $X_i$ , they also depend exciton interferences  $C_i^\alpha(C_i^\beta)^*$ . The summation in equation (4.23) therefore allows for interferences which result in a smaller work flux despite increased local displacements.

In PE545 moderate rates of excitation input result in a negative work flux and therefore the system does work on the vibrations. As the rate is further increased the work flux reverses direction and the vibrations do work on the electronic degrees of freedom. In PC645 the direction of the work flux is reversed and its amplitude reduced by the presence of the vibrational mode. Under-damped vibrations allow the environment to shift further from equilibrium under steady excitation input. This can result in both positive and negative work flux and as a result of exciton interferences can even reduce the amplitude of work flux as is observed in PC645.

In the transient setting the majority of work flux occurs whilst the exciton-vibration system relaxes. This time scale is partially determined by the damping of the vibrational mode  $\gamma_{\text{damp}}$ . Damped vibrations relax faster and therefore reduce the potential for work flux. Figure 4.10 displays the steady state work flux and environmental displacements  $\sum_i |X_i(t_s)|$  as the time scale  $\gamma_{\text{damp}}^{-1}$  of vibration relaxation is altered. In the PE545 subunit both the amplitude of work flux and the net displacement of the environment increase as the time scale of damping is reduced (the vibration relaxes more slowly). This is consistent with the notion that under-damped vibrations can be further out of equilibrium and that this results in a larger work flux. However, in PC645 the central dimer behaves more as a heat source. Rapidly damped vibrations feature a steady state which is displaced further from equilibrium than under-damped vibrations. Thus as the time scale of damping is increased, the amplitude of work flux displays a decreasing trend.

## 4.6 Concluding remarks and outlook

The formalism adopted in this chapter enables the partitioning of energy fluxes between electronic and vibrational degrees of freedom into work-like and heat-like

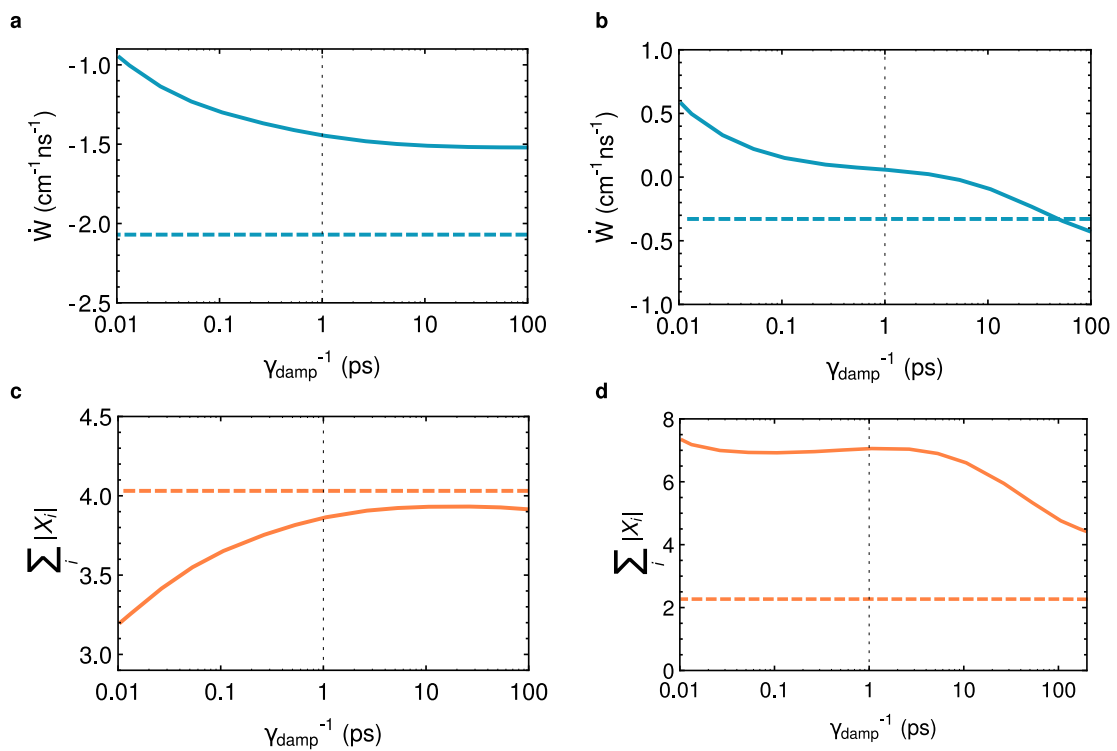


Figure 4.10: Stationary work flux against the time scale of vibrational relaxation  $\gamma_{\text{damp}}^{-1}$  in (a) PE545 and (b) PC645. (c) The corresponding net  $\sum_i |X_i|$  in PE545 and (d) PC645. Dashed curves are for an unstructured environment while solid curves include an underdamped vibration.

contributions. We found that relative nature of energy fluxes is dependent on the strength of electronic coupling between chromophores. In particular we have shown that in the weakly electronically coupled PE545 system the combined exciton-vibration dynamics results in energy exchanges with vibrations which are predominantly work like. The more strongly electronically coupled central dimer of PC645 introduces a significant heat-like component to energy fluxes.

A recent analysis of four phycobiliprotein structures including PE545 and PC645 [202] has highlighted that a genetic switch controls the electronic coupling of the central dimer in these complexes. The addition of a single amino acid to the otherwise identical the protein structure is responsible for causing a change in the orientation assembled protein subunits in the PC612 and PE555 complexes. This results in the separation of the central chromophores and the formation of a water filled channel. As a result the electronic coupling of the central dimers in these ‘open’ structures is highly reduced. In the study they find inter-dimer electronic couplings of  $166\text{ cm}^{-1}$  and  $647\text{ cm}^{-1}$  in the closed PE545 and PC645 structures respectively. The insertion of the amino acid causes the electronic coupling in open PC612 and PE555 structures to be reduced, to  $29\text{ cm}^{-1}$  and  $4\text{ cm}^{-1}$  respectively. In the context of this chapter, the structural switch these cryptophytes have evolved may be viewed as a way of modulating the nature of energy exchange with vibrations motions. In Chapter 3 a classical model of vibrations was employed in which the interaction with vibrations is accounted for entirely as effective time dependent drive of site energies. In the context of the thermodynamic framework adopted in this chapter we immediately see that these classical vibrations act purely as a source of work. We also saw that work fluxes can persist even under continuous illumination, since vibrations are in a non-equilibrium steady state. The character of work fluxes is dependent on the rate of excitation input and the time-scale of damping of the mode while the quantum efficiency remains high. This suggests a potential role for vibrations which is neither beneficial nor detrimental to this efficiency. Vibrations can display a broad range of thermodynamic behaviour which is dependent on the operating regime of the system at hand. If there is any biological role for the steady state work fluxes identified in these photosynthetic prototypes is a matter for debate. Nevertheless the formalism and ideas developed within this chapter are certainly applicable to many other systems. Even if it transpires that the thermodynamic implications of non-equilibrium vibrations are minimal for biological systems, it is not difficult to envisage their importance in the design of quantum technologies which exploit structured environments for their function.

# Chapter 5

## Acclimation of energy transfer

*We investigate how energy transfer within and between light harvesting antenna complexes from purple bacteria acclimates to different illumination conditions. Using generalized Förster theory, we find that intra-complex B800-B850 transfer is accelerated from  $1.14 \text{ ps}^{-1}$  to  $1.43 \text{ ps}^{-1}$  under low light conditions due to an increase in spectral overlap of donating B800 and accepting B850 exciton states. We speculate that differences in quasi-resonance of this energy gap with vibrational modes for certain realizations of disorder may result the acclimation of non-classicality of vibrational modes. Mean inter-complex energy transfer rates are not found to acclimate significantly being  $0.16 \text{ ps}^{-1}$  for both high and low light illumination conditions. However we conclude that mixing of high and low light adapted apoprotein types within a single complex results in a less energetically disordered energetic landscape of partially acclimated photosynthetic membranes which reduces energetic traps.*

### 5.1 Spectral adaptation of the photosynthetic apparatus of purple bacteria

Purple photosynthetic bacteria are generally aquatic microorganisms and can be found in freshwater lakes, stagnant ponds even sewage treatment facilities [4]. They perform photosynthesis anaerobically, meaning that they do not produce oxygen. They are highly adaptable and the architecture of their photosynthetic apparatus varies considerably from species to species. Since they must survive in low light conditions where photons are precious, they have developed a large effective cross-

sectional area for light absorption. Their photosynthetic membranes comprise several types of antenna complex which absorb in different regions of the spectra. A review of the photosynthetic apparatus and energy transfer mechanisms in purple bacteria can be found in [203].

Figure 5.1 illustrates the typical arrangement of circular light harvesting antennae complexes in a purple bacteria cell membrane. Many peripheral light harvesting 2 (LH2) complexes surround light harvesting 1 (LH1) complexes whose core features a single reaction centre towards which absorbed quanta of energy are ‘funnelled’ [204]. Once a reaction centre has absorbed this energy, charge separation takes place which drives a cycle of electron transfer reactions. During this cycle additional electron separations cannot take place and this effectively ‘closes’ the reaction meaning any additional energy absorbed is radiately dissipated. A membrane composed entirely of LH1 complexes would be both inefficient and biosynthetically expensive. The peripheral LH2 complexes allow absorption over a broader spectral and spatial range and enable efficient photosynthesis to take place under a variety of illumination conditions. The ratio of LH1 to LH2 type complexes can acclimate

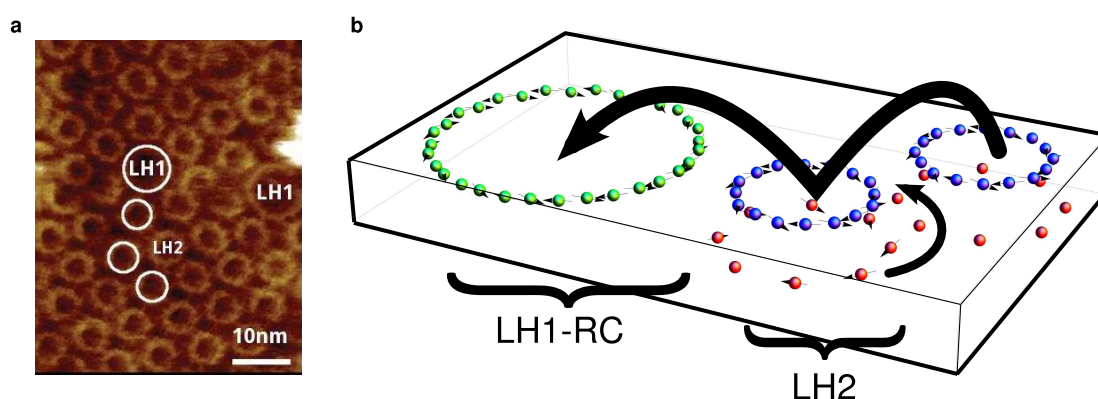


Figure 5.1: (a) Atomic force microscope image of the photosynthetic membrane from *Rhodospirillum rubrum*, adapted from Fig. 3b of ref. 205. (b) Schematic of the arrangement of pigments within LH1 and LH2 complexes based on data from references 206 and 207.

to the level of light intensity [205]. Kinetic models of energy transfer at the level of the photosynthetic membranes have been applied to understand the functional implication of these adaptations [208]. Under stressed environmental conditions such as low light intensity, some species of purple bacteria produce LH2 variants (LH3, LH4 and so forth) which absorb in different regions of the spectra.

The differences in spectral features of LH2 variants result from the acclimation

of electronic and vibrational properties, which must tune electronic and vibrational dynamics. In this chapter we investigate the acclimation of energy transfer in LH2 antennae complexes from purple photosynthetic bacteria at the intra and inter-complex level, as the first steps towards identifying possible adaptation of quantum features of energy transfer dynamics. This is timely, since a number of experiments have reported evidence of quantum coherent transport in the LH2 complex [15, 16, 209].

### 5.1.1 The light harvesting 2 (LH2) antenna complex

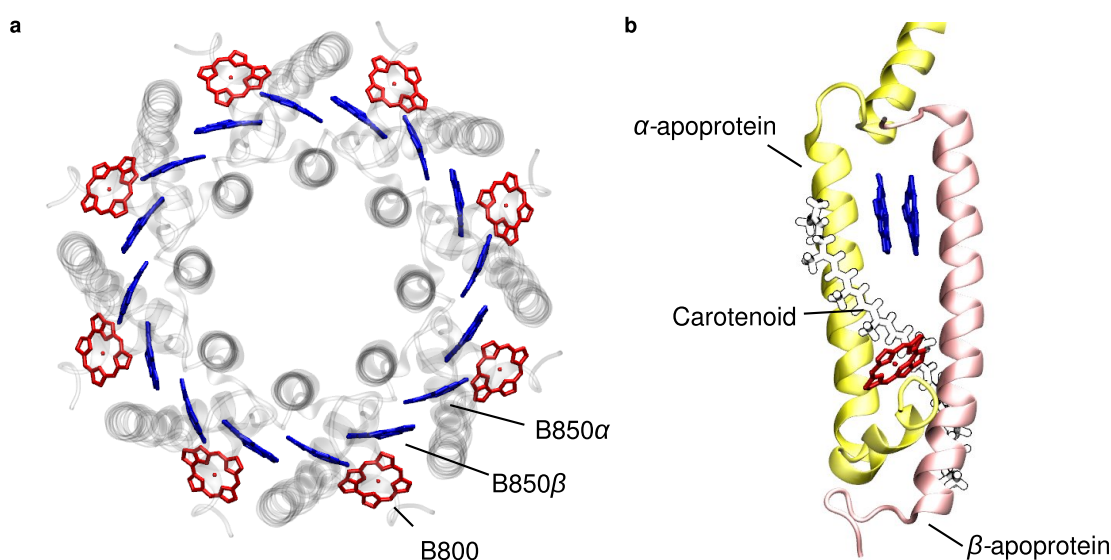


Figure 5.2: Representations of the LH2 structure from *P. molischianum* (Protein Data Bank ID code 1LGH [207]) produced with VMD [210]. (a) Top view of the whole complex: B800 BChls are illustrated red and B850 BChls in blue. alpha-beta apoprotein units are shown in grey. The carotenoids (lycopene) and BChl phytol tails are not displayed for clarity. (b) Side view of a single  $\alpha$ - $\beta$  unit. alpha (beta) apoprotein displayed in yellow (pink).

The LH2 complex comprises eight or nine subunits which oligomerize into a circular macro-structure. The octameric structure of the LH2 complex from *Phaeospirillum molischianum* (formerly *Rhodospirillum molischianum*) is illustrated in Fig. 5.2. Within each subunit an alpha-beta apoprotein heterodimer binds together three bacteriochlorophyll *a* (BChl*a*) chromophores and one (or two) carotenoids. The carotenoids aid in the structural stability of the assembled complex and also have a photo-protective role. By quenching the triplet excited state of BChls they sup-

press energy transfer to oxygen thus they prevent formation of the highly reactive singlet state of oxygen. They also serve as accessory pigments absorbing between 400-600 nm and rapidly ( $\sim 50$  fs) transferring energy to BChls [211]. In the assembled complex, the BChl chromophores form two concentric rings. The first is an octameric or nonameric ring whose chromophores are weakly electronically coupled due to large inter-chromophore distances  $\sim 22$  Å. This is referred to as the B800 ring since it absorbs spectrally close to the position of BChl monomers (800 nm). The second hexadecameric octadecameric ring is more tightly packed with inter-chromophore distances  $\sim 9$  Å and is therefore more strongly electronically coupled the collective absorption is shifted to 850 nm. This ring is therefore referred to as B850.

**Acclimation** The acclimated variants of the LH2 complex which are produced under low light conditions bind together the same numbers of chromophores but have different alpha and beta apoprotein structures. The crystal structure of low light adapted LH2 complex variant of the *Rhodoblastus acidophilus* (formerly *Rhodopseudomonas acidophila*) species has been resolved to 3.0 Å [212]. The positioning of BChl molecules in the low light variant is found to be highly similar to the high light adapted structure. The relative orientation of dipole-moments and therefore electronic couplings between chromophores are therefore expected to be similar. The differences in the alpha and beta apoprotein structures results in altered hydrogen bonding between particular protein residues and acetyl groups of the B850 chromophores. The resulting conformation of the BChl is known to shift site energy of the  $Q_y$  excited state [213]. This results in complexes referred to as B820 or LH3 which absorb near 820 nm.

As the membranes acclimate to lower light intensity the 850 nm peak in ensemble absorption spectra of membrane progressively shifts to 820 nm. Fig. 5.3a displays the absorption spectra of B850 and B820 and three intermediate membranes from *molischianum* (courtesy of James N. Sturgis). It was previously thought that during adaptation membranes consist of a mixture high and low light adapted B850 and B820 type LH2 complexes. However in *molischianum* [214] and *Rhodopseudomonas palustris* [215] it has been demonstrated that both the high and low type alpha-beta apoproteins pairs can found within a single complex. This results in spectrally heterogeneous complexes with character of both B850 and B850 as illustrated in Fig. 5.3b. The mixing of high and low type alpha-beta apoprotein types within a complex results in a less energetically disordered energetic landscape of partially



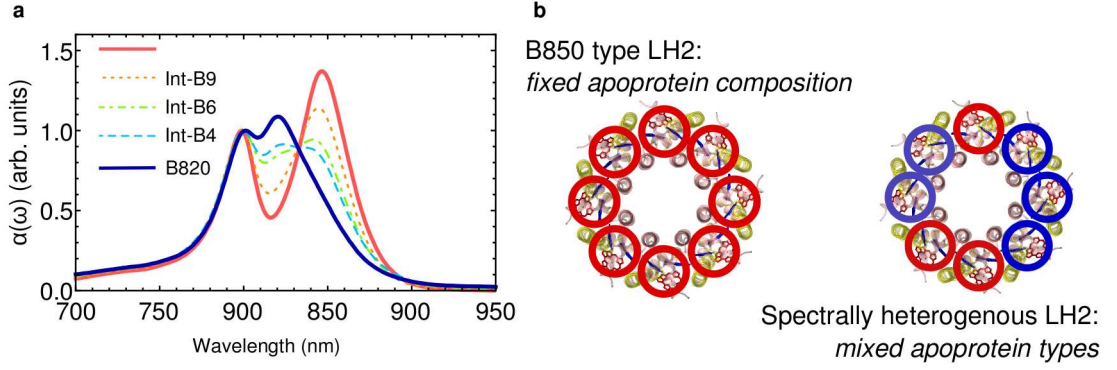


Figure 5.3: (a) Experimental absorption spectra of LH2 complexes acclimated to different light intensities. (b) Schematic of the apoprotein composition of adapted LH2 complexes.

adapted membranes which may eliminate energetic traps.

## 5.2 Linear spectroscopy

Linear absorption and fluorescence (emission) spectra yield information about the electronic structure and vibrational environments of biomolecules. Parameters entering into theoretical models of dynamics can be estimated by fitting experimental spectra. In this chapter the linear spectra of LH2 antenna acclimated to different light conditions are simulated as a benchmark of the parameters describing excitation energy transfer. In this section we therefore briefly outline some background material for the theoretical description of the linear spectra of biomolecules.

Assuming weak interaction with classical light [44, 68], applying Fermi's golden rule with respect to the interaction  $H_{\text{light-matter}} = -\vec{E}(e^{-i\omega t} + e^{+i\omega t}) \cdot \vec{\mu}$  in the rotating wave approximation, gives the rate of transitions between ground and excited states and therefore the calculation of linear absorption  $\alpha(\omega)$  and fluorescence  $I(\omega)$  can be expressed as the Fourier transform of the dipole-dipole correlation functions [44, 47]

$$\alpha(\omega) \propto \omega \, 2 \Re \int_0^\infty dt \, e^{i\omega t} \langle \vec{\mu}(t) \vec{\mu}(0) \rangle_g \quad (5.1)$$

and

$$I(\omega) \propto \omega \, 2 \Re \int_0^\infty dt \, e^{i\omega t} \langle \vec{\mu}(t) \vec{\mu}(0) \rangle_e, \quad (5.2)$$

where  $\vec{\mu} = \sum_i \vec{\mu}_i (|0\rangle \langle i| + |i\rangle \langle 0|)$  is the total dipole moment operator associated with the excited states of the biomolecule. The subscripts e and g denote the state with respect to which the correlation function is calculated. Since thermal fluctuations

are small in comparison with the excitation energies of the chromophores, prior to absorption of a photon the system is assumed to be in the state  $\rho_{(g)}^{\text{eq}} = |0\rangle\langle 0| \otimes \varrho_{\text{vib}}^{\text{eq}}$ . For the case of steady state fluorescence the system has relaxed to an equilibrium state in the excited state and  $\rho_{(e)}^{\text{eq}} = e^{-\beta H} / \text{Tr}\{e^{-\beta H}\}$  where  $H$  is the full exciton-vibration Hamiltonian. These correlation functions can be calculated numerically within the HEOM framework [44, 216],

$$\langle \mu(t)\mu(0) \rangle_g = \text{Tr}_S [\text{Tr}_B \{ \mathcal{U}(t)(\vec{\mu}|0\rangle\langle 0|\varrho^{\text{eq}})\vec{\mu} \}] = \sum_i \mu_i \sigma_{0i}(t) \quad (5.3)$$

where the evolution  $\sigma_{0i}(t) = \langle 0 | \text{Tr}\{ \mathcal{U}(t)\mu \} | i \rangle$ . Perturbative theories can also be applied in the calculation of these correlation functions. Indeed for a monomer interacting with a harmonic oscillator environment the second order cumulant expansion reproduces the line shape exactly [68, 217, 218].

For systems of many coupled chromophores the linear spectra can be expressed in terms of the line shapes of excitonic states as  $\alpha(\omega) \propto \sum_{\alpha} |\vec{\mu}_{\alpha}|^2 D_{\alpha}(\omega)$  and  $I(\omega) \propto \sum_{\alpha} P_{\alpha} |\vec{\mu}_{\alpha}|^2 \bar{D}_{\alpha}(\omega)$ . Here  $P_{\alpha}$  denotes the steady state occupation probability of the exciton states. For weak coupling to the vibrations this has the distribution  $P_{\alpha} = \exp(-\beta E_{\alpha}) / \sum_{\alpha} \exp(-\beta E_{\alpha})$ . The delocalisation of excitonic states results in a redistribution of dipole strengths according to  $|\vec{\mu}_{\alpha}|^2 = |\sum_i C_i^{\alpha} \vec{\mu}_i|^2$  which can result in dark states. As example consider a coupled homo-dimer with aligned transition dipoles  $\mu_1 = \mu_2 = \mu$ . The eigenstates (labeled by  $\pm$ ) have excitonic oscillator strength  $|\mu_{\pm}|^2 = (1 \pm \sin(2\theta))|\mu|^2$  and therefore for strong coupling ( $\theta \rightarrow \pi/4$ ) one of the states has no dipole strength. Perturbative theories can be applied to derive expressions for excitonic line shapes [37, 59, 219–222] which are far more efficient to calculate than directly propagating the HEOM. The excitonic line shapes often have the form

$$D_{\alpha}(\omega) = 2 \Re \int_0^{\infty} dt e^{i\omega t} \exp(-i\omega_{\alpha}t - g_{\alpha\alpha,\alpha\alpha}(t) - t/\tau_{\alpha}) \quad (5.4)$$

and

$$\bar{D}_{\alpha}(\omega) = 2 \Re \int_0^{\infty} dt e^{i\omega t} \exp(-i\omega_{\alpha}t + 2i\lambda_{\alpha\alpha,\alpha\alpha}t - g_{\alpha\alpha,\alpha\alpha}^*(t) - t/\tau_{\alpha}), \quad (5.5)$$

where as before,  $g_{\alpha\beta,\gamma\delta}(t) = \sum_i Q_{\alpha\beta}^i Q_{\gamma\delta}^i g_i(t)$ ,  $g_i(t) = \int_0^t ds \int_0^s ds' C_i(s')$  and  $\lambda_{\alpha\beta,\gamma\delta} = \sum_i Q_{\alpha\beta}^i Q_{\gamma\delta}^i \lambda_i$ . For the present interaction,  $Q_{\alpha\beta}^i = \langle \alpha | \sigma_i^+ \sigma_i^- | \beta \rangle = (C_i^{\alpha})^* C_i^{\beta}$ . Here  $\omega_{\alpha}$  refers to the energies of the eigenstates of the shifted system Hamiltonian  $H_S + H_{\text{reorg}}$ , where reorganisation has been included into bare site energies such that a monomer

absorbs at  $\epsilon_i + \lambda_i$  and fluoresces at  $\epsilon_i - \lambda_i$ . The monomer line broadening function  $g_i(t)$  for a spectral density whose corresponding correlation function is expressed as the series  $C_i(t) = \sum_k c_{i,k} e^{-\nu_{i,k} t}$  is given by

$$g_i(t) = \sum_k \frac{c_{i,k}}{\nu_{i,k}^2} (e^{-\nu_{i,k} t} + \nu_{i,k} t - 1) . \quad (5.6)$$

For a Drude–Lorentz spectral density the summation over Matsubara terms appearing in the line broadening function can be expressed in terms of special functions (`HurwitzLerchPhi` in `Mathematica`), alternatively at high temperatures the series can be truncated. Useful low temperature approximations for underdamped Brownian oscillator spectral density are given in [223]. The exciton lifetimes  $\tau_\alpha$  are determined by rate of transfer to other exciton states  $\tau_\alpha^{-1} = \frac{1}{2} \sum_{\alpha \neq \beta} k_{\alpha\beta}$ . These rates depend on the nature of theory used to calculate the lineshape. If Redfield theory is used, these rates are given by  $k_{\alpha\beta}^R = R_{\alpha\alpha,\beta\beta}$ , the relevant elements of the Redfield tensor given by equation (1.19). For modified Redfield theory  $k_{\alpha\beta}^{MR}$  are given by equation (1.25) and Förster theory gives the transfer rate between localised sites as

$$k_{ab}^F = 2|V_{ab}|^2 \Re \int_0^\infty dt e^{i\omega_{ab}t - g_a(t) - g_b(t) - i\lambda_a t - i\lambda_b t} . \quad (5.7)$$

### 5.2.1 Comparison of perturbative theories

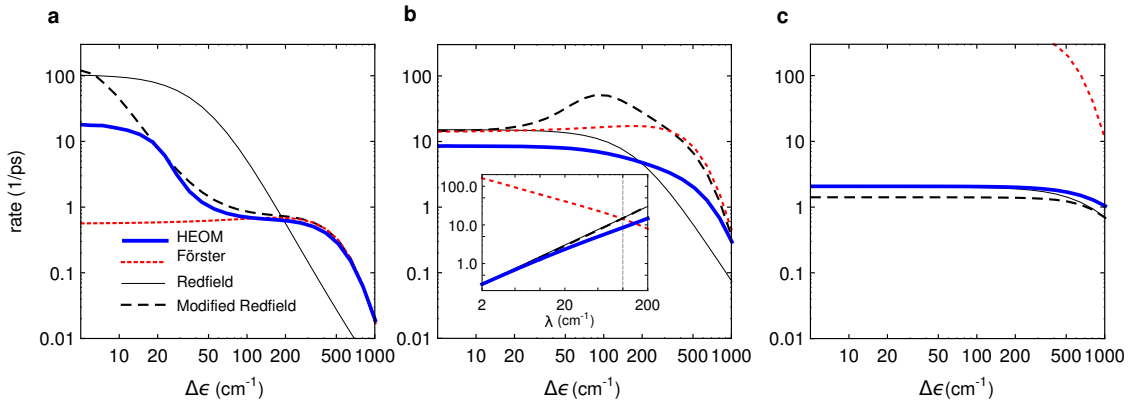


Figure 5.4: The downhill rate of transfer between the excitonic states of a dimer system with Hamiltonian  $H = (\Delta\epsilon/2)\sigma_z + V\sigma_x$  subject to environments characterized a Brownian oscillator spectral density with  $\lambda = 100$  cm<sup>-1</sup> and  $\Omega_c = 53$  cm<sup>-1</sup> = (100 fs)<sup>-1</sup> for electronic coupling strength (a)  $V = 20$  cm<sup>-1</sup>, (b)  $V = 100$  cm<sup>-1</sup> and (c)  $V = 500$  cm<sup>-1</sup>. The inset of panel (b) shows the variation of transfer rate with reorganisation energy  $\lambda$  for  $\Delta\epsilon = 10$  cm<sup>-1</sup>.

In ref. 75 a systematic comparison of the energy transfer rates predicted by

Förster, Redfield and modified Redfield theories was undertaken. In Fig. 5.4 we display the analogue of Figure 2 in ref. 75 but for a Brownian oscillator spectral density rather than the Gaussian form used there. The room temperature (300 K) transfer rate in a dimer  $H = (\Delta\epsilon/2)\sigma_z + V\sigma_x$  is calculated as a function of the site energy gap  $\Delta\epsilon$  for three different electronic coupling strengths. The key addition here is the rate of transfer between exciton states determined from converged HEOM dynamics. For all the rates presented, the dynamics are free from oscillations and rates  $k_{\alpha\beta}^{\text{HEOM}}$  can therefore be extracted from fits to the solution of a Pauli master equation for exciton populations  $\dot{\rho}_{\alpha\alpha}(t) = \sum_{\beta} (-k_{\alpha\beta}\rho_{\alpha\alpha}(t) + k_{\beta\alpha}\rho_{\beta\beta}(t))$ .

For weak electronic coupling with respect to the environment ( $\lambda > V$ , Fig. 5.4a) and localised states ( $\Delta\epsilon \gg 2V$ ) the Förster rate agrees with the exact HEOM rate and modified Redfield theory agrees for energy gaps larger than the electronic coupling. Redfield theory is predictably inaccurate since it is derived assuming strong electronic coupling. For intermediate coupling strength with respect to the environment ( $\lambda \approx V$ , Fig. 5.4b) none of the three theories is adequate. In particular the maxima in the modified Redfield rate near  $\Delta\epsilon = 100 \text{ cm}^{-1}$  is a behaviour completely absent when transfer rates are extracted from the converged HEOM results. This shows that the optimized energy transfer rate highlighted in [75] is spurious. When the electronic and environmental coupling strengths are of the same order, the modified Redfield rate in this system is less accurate than that predicted by standard Redfield theory. It is surprising that for small  $\Delta\epsilon$  where excitons are highly delocalised, the Förster and Redfield rates appear to coincide. The inset of Fig. 5.4b shows the variations of rates with  $\lambda$  for  $\Delta\epsilon = 10 \text{ cm}^{-1}$ . This reveals that while Redfield and modified Redfield rates have excellent agreement with exact HEOM rates for small  $\lambda$ , the Förster rate is much too large. The Förster expression incorrectly predicts a decreasing rate with increasing  $\lambda$  which coincidentally agrees with the Redfield rates near  $\lambda = 100 \text{ cm}^{-1}$ .

For strong electronic coupling with respect to the environment ( $V > \lambda$ , Fig. 5.4c) both modified and standard Redfield theory are accurate. The Förster rate is meaningless in this regime since the exciton states are highly delocalised and again predicts a transfer rate which is much too large.

The absorption spectra  $\alpha(\omega)$  predicted by Redfield, modified Redfield and HEOM theories for the above dimer with  $\Delta\epsilon = 200 \text{ cm}^{-1}$  are shown in Fig. 5.5. Monomer dipole strengths are assumed to be equal and aligned ( $\vec{\mu}_1 = \vec{\mu}_2 = (\mu, 0, 0)$ ). The main differences between the theories arise in the intermediate coupling regime. Since the modified Redfield predicts a transfer rate orders magnitude too large, the

lifetime broadening of the exciton line shapes is hugely overestimated. The standard Redfield line shape is also inaccurate in this regime but provides a better estimate than modified Redfield theory.

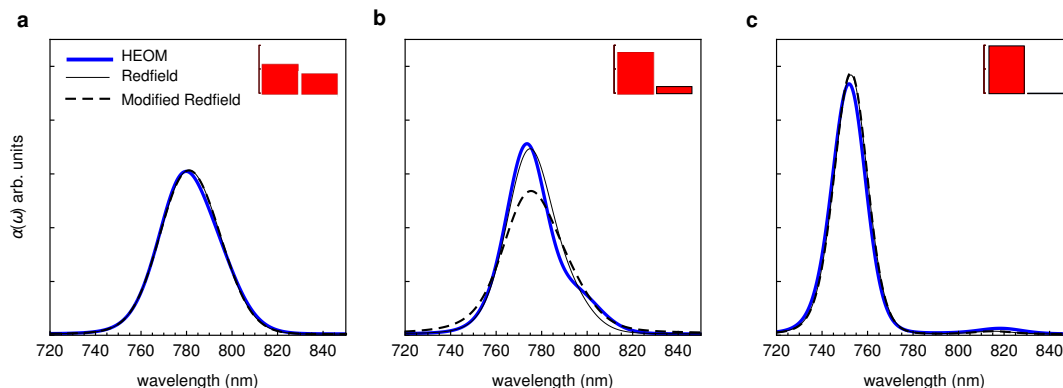


Figure 5.5: The absorption spectra of the dimer for which transfer rates are shown in Fig. 5.4 with  $\Delta\epsilon = 200 \text{ cm}^{-1}$ . (a)  $V = 20 \text{ cm}^{-1}$ , (b)  $V = 100 \text{ cm}^{-1}$  and (c)  $V = 500 \text{ cm}^{-1}$ . The red bars indicate the dipole strength  $|\mu_\alpha|^2$  of the dimer excitonic states.

## 5.2.2 Inhomogeneous line broadening

The theory of line shapes discussed above applies to a single biomolecule only. Standard linear spectroscopy is in fact an ensemble measurement of many biomolecules each with slightly different electronic parameters. In photosynthetic light harvesting antennae, slow conformational motion of the protein environment modulates both site energies and electronic couplings, resulting in shifts which are effectively static on the timescale of absorption and fluorescence measurements. This disorder must therefore be taken into account with an ensemble average over many realizations of electronic parameters. The ensemble average results in inhomogeneous broadening of spectra, in contrast to the homogeneous line broadening which occurs for each individual biomolecule.

Usually, disorder in site energies is accounted for by drawing site energies from a Gaussian distribution with standard deviation  $\sigma$  and mean  $\epsilon_i$ . This is referred to as diagonal disorder, while disorder in electronic couplings is termed off-diagonal disorder. For the B850 ring of LH2 it has been shown that the assumption of Gaussian fluctuations is reasonable and that the magnitude of diagonal and off-diagonal fluctuations are compatible and potentially correlated [224]. It has been proposed that elliptical deformations of the ring [225] is at the origin of these correlations.

Molecular dynamics simulations have shown that off-diagonal interactions are negligible on the timescale of fs to ps [48]. However the duration of these simulations is typically far too short to capture the type of protein motion which results in static disorder (on the order of ms to s) and thus cannot be used to justify the neglect of off-diagonal disorder. Single molecule spectroscopy is a powerful tool which enables the examination of individual realizations of disorder. These techniques have been used to probe large numbers of LH2 complexes in *acidophila*, with the conclusion that static disorder is predominantly diagonal [226].

The mixing of apoprotein types can be viewed as an additional source of inhomogeneous line broadening. In partially adapted photosynthetic membranes, the ensemble contains complexes with mixed  $\alpha$ - $\beta$  subunit types. We assume that complexes are assembled randomly with a probability  $p$  of being B850 type and  $(1 - p)$  B820 type. Thus,  $p = 1(0)$  describes an ensemble of spectrally pure B850(B820) complexes.

### 5.3 Generalizations of Förster theory

Of the perturbative theories discussed in section 5.2.1, none is able to adequately reproduce transfer rates for weak, intermediate and strong electronic coupling simultaneously, hence the need for the non-perturbative HEOM method used in previous chapters. However, it is extremely numerically intensive to apply the HEOM method to larger systems such as the 24 site B800-B850 LH2 or 32 site B850-B850 system. In the current study we investigate the role of disorder introduced by acclimation, which also requires the calculation of dynamics for many realizations of disorder. One often encounters the scenario where a strongly electronically coupled cluster of sites is weakly coupled to another strongly coupled cluster. This is true of the intra-complex energy transfer between the B800 and B850 rings of LH2 as well as inter-complex transfer between the B850 rings of adjacent LH2 complexes.

Whilst conventional Förster theory which describes the rate of energy transfer between weakly electronically coupled sites which have localised excited states, generalizations of Förster theory have been developed [227–230] which give the rate of energy transfer between the delocalised excited states of different clusters, when inter-cluster coupling is weak. Here we utilize the diagonal formulation of the theory [228], which gives transfer rates from donor cluster D to acceptor cluster A as  $K_{DA}^{GFT} = \sum_{\alpha\beta} P_{\alpha} k_{\alpha\beta}$ . As with conventional Förster theory, the donor is assumed to equilibrate rapidly before transfer to the acceptor takes place. Thus  $P_{\alpha}$  denotes the

thermal occupation of the donor cluster exciton states. Transfer rates from donor state  $\alpha$  to acceptor state  $\beta$  are given by

$$k_{\alpha\beta} = \frac{|V_{\alpha\beta}|^2}{2\pi} \int_{-\infty}^{\infty} d\omega \bar{D}_{\alpha}(\omega) D_{\beta}(\omega) = |V_{\alpha\beta}|^2 J_{\alpha\beta} , \quad (5.8)$$

where the coupling of donor exciton state  $\alpha$  to acceptor exciton state  $\beta$  is given by  $V_{\alpha\beta} = \sum_{i \in D, j \in A} C_i^{\alpha} C_j^{\beta*} V_{i,j}$ . The overlap  $J_{\alpha\beta}$  of donor fluorescence and acceptor absorption line shapes should be calculated with a theory which adequately describes energy transfer within the strongly coupled cluster. For the line shape expressions given by (5.4) and (5.5), this overlap can be conveniently expressed in the time domain as

$$J_{\alpha\beta} = 2 \Re \int_0^{\infty} dt e^{i\omega_{\alpha\beta}t} e^{-i(\lambda_{\alpha\alpha,\alpha\alpha} + \lambda_{\beta\beta,\beta\beta})t} e^{-(g_{\alpha\alpha,\alpha\alpha}(t) + g_{\beta\beta,\beta\beta}(t))} e^{-(1/\tau_{\alpha} + 1/\tau_{\beta})t} , \quad (5.9)$$

where the property of the line broadening function  $g(-t) = g^*(t)$  is used.

## 5.4 Acclimation of intra-complex energy transfer

The highest energy chromophores in the LH2 complex lie in the weakly electronically coupled B800 ring. Energy transfer between the B800 and B850 bands of this system has been extensively studied [228, 231, 232] and conventional Förster theory is known to underestimate the rate of transfer [233]. Previous studies have modelled energy transfer from a single B800 chromophore to the B850 ring, however in 234 the role of coherence in the B800 ring was emphasised in improving the uniformity and robustness of energy transfer to B850 by modelling the B800 ring as a dimer. Here we apply GFT to calculate transfer rates from the full B800 ring to B850 rings with different degrees of acclimation.

### 5.4.1 Electronic parameters

To estimate the electronic couplings of the  $Q_y$  excited states of the BChl chromophores in the LH2 complex, the point dipole approximation of equation (1.4) is often applied since inter-chromophore distances and directions of dipole moments (assumed to point from the  $N_b$  to  $N_d$  nitrogen atoms in each BChl) are readily extracted from the crystal structure data. The constant  $C$  appearing in equation (1.4) is then adjusted to reproduce the energies of excitonic states. Values vary, with early literature on *molischianum* e.g. Hu *et al.* [206] using large values



Coupling	Point dipole ( $\text{cm}^{-1}$ )	CEO ( $\text{cm}^{-1}$ )
$V_{B800}$	-19	-19
$V_{\alpha_1\beta_1}$	470	258
$V_{\beta_1\alpha_2}$	428	210
$V_{\alpha_1\alpha_2}$	-67	-67
$V_{\beta_1\beta_2}$	-45	-40
$V_{\alpha_1\beta_2}$	18	22
$V_{\beta_1\alpha_3}$	15	17
$V_{B800\alpha_1}$	5.3	8.2
$V_{B800\beta_1}$	21	25
$V_{B800\alpha_2}$	-31	-36
$V_{B800\beta_2}$	2.6	5.4

Table 5.1: Strength of electronic coupling between selected chromophores of the LH2 complex from *molischianum*. Point dipole values calculated using equation (1.4) with  $C = 230000 \text{ \AA}^3 \text{cm}^{-1}$ . Collective electronic oscillators method values taken from [236].

( $C = 519310 \text{ \AA}^3 \text{cm}^{-1}$ ) which results in large intra and inter B850 dimer couplings  $V_{\alpha_1\beta_1} = 806 \text{ cm}^{-1}$  and  $V_{\beta_1\alpha_2} = 337 \text{ cm}^{-1}$ . This has been revised downwards in subsequent works, for example Sundstrom *et al.* [235] found intra and inter B850 dimer couplings  $V_{\alpha_1\beta_1} = 339 \text{ cm}^{-1}$  and  $V_{\beta_1\alpha_2} = 336 \text{ cm}^{-1}$  and nearest neighbour B800 couplings  $V_{B800} = -14 \text{ cm}^{-1}$  ( $C \approx 174000 \text{ \AA}^3 \text{cm}^{-1}$ ). Novoderezhkin *et al.* [232] found  $V_{\alpha_1\beta_1} = 273 \text{ cm}^{-1}$ ,  $V_{\beta_1\alpha_2} = 249 \text{ cm}^{-1}$  and  $V_{B800} = -11 \text{ cm}^{-1}$  using  $C \approx 133850 \text{ \AA}^3 \text{cm}^{-1}$ . More sophisticated theories such as the transition density cubes method (TDCM) have yielded in more accurate values for the *acidophila* species. The collective electronic oscillators (CEO) method is applied in [236] to estimate electronic couplings for a subset of chromophores in *molischianum* giving values which are reproduced in the last column of Table 5.1. In the present work, electronic couplings between chromophores in the LH2 complex are calculated using pigment positions and dipole moments extracted from the crystal structure of *molischianum* (1LGH) [207] and listed in Table 5.A.1 and 5.A.2. Employing the point dipole approximation with the value  $C = 230000 \text{ \AA}^3 \text{cm}^{-1}$  reproduces the coupling  $V_{B800} = -19 \text{ cm}^{-1}$  of [236] for which the dipole approximation is anticipated to be accurate. Many other couplings calculated using the CEO algorithm [236] are reasonably reproduced with this value of  $C$  as shown in Table 5.1. Couplings between chromophores in close proximity (*e.g.* nearest neighbour couplings in the tightly packed B850 ring  $V_{\alpha_1\beta_1}$  and  $V_{\alpha_2\beta_1}$ ) are not well approximated by the point dipole approach and are therefore replaced with the results of the more accurate theory



[236]. For site energies we use  $E_{B800} = 12540 \text{ cm}^{-1}$ ,  $E_{B850\alpha} = 12355 \text{ cm}^{-1}$  and  $E_{B850\beta} = 12055 \text{ cm}^{-1}$  based on [232] and with slight adjustments such that the calculations of absorption spectra in Fig. 5.6 reproduce experimental spectra.

The low light adapted LH2 B820 structure of *molischianum* has not yet been crystallised. Based on the similarity of the high [237] and low [212] light adapted LH2 structures from *acidophilla*, we assume identical positioning and dipole-moments of BChl molecules in high and low light adapted complexes from *molischianum*. We therefore assume that electronic couplings are identical in both B850 and B820 type subunits in *molischianum*. However, the low light  $\alpha$ - $\beta$  apoprotein structures interact differently with  $Q_y$  excited states in the B820 ring which results in a shift in site energy [213]. We use  $E_{B820\alpha(\beta)} = E_{B850\alpha(\beta)} + 320 \text{ cm}^{-1}$ , a shift which reproduces the position of the maxima in calculations of B820 absorption spectra (Fig. 5.6a).

### 5.4.2 Environmental parameters

The environments of B800 and B850 chromophores are characterized so as to reproduce the features of the experimental absorption spectra calculated using Redfield theory and displayed in Fig. 5.6. We assume a Drude–Lorentz form  $J_D(\omega)$  for the spectral density with  $\lambda^{B800} = 35 \text{ cm}^{-1}$ ,  $\Omega_c^{B800} = 35 \text{ cm}^{-1}$ ,  $\lambda^{B850} = 200 \text{ cm}^{-1}$  and  $\Omega_c^{B800} = 53 \text{ cm}^{-1}$  and neglect vibrational modes. Diagonal static disorder is accounted for by sampling site energies from Gaussian distribution with  $\sigma^{B800} = 50 \text{ cm}^{-1}$  and  $\sigma^{B850} = 200 \text{ cm}^{-1}$ . The above parameters are typical of those used in previous literature on LH2 [206, 224, 228, 232, 234, 238, 239].

### 5.4.3 Calculated linear spectra

Fig. 5.6 displays ensemble average high and low light LH2 absorption and fluorescence spectra. The curves are the results of the use of equations (5.4) and (5.5) with exciton lifetimes calculated using Redfield rates and 10,000 realizations of diagonal static disorder. The points are experimental absorption spectra (courtesy of James N. Sturgis). The high light (B850) absorption is reproduced well, although the high energy tail is underestimated. This may arise from the broadened vibronic progressions associated with under-damped discrete modes which are neglected in our model. In the low light (B820) absorption spectra, there is also shoulder in the low energy region which is missing in the calculated spectra. It could be that the excitonic dipole strength  $|d_\alpha|^2$  associated with the lowest exciton is underestimated. For a circular system without disorder and only nearest neighbour interactions, only

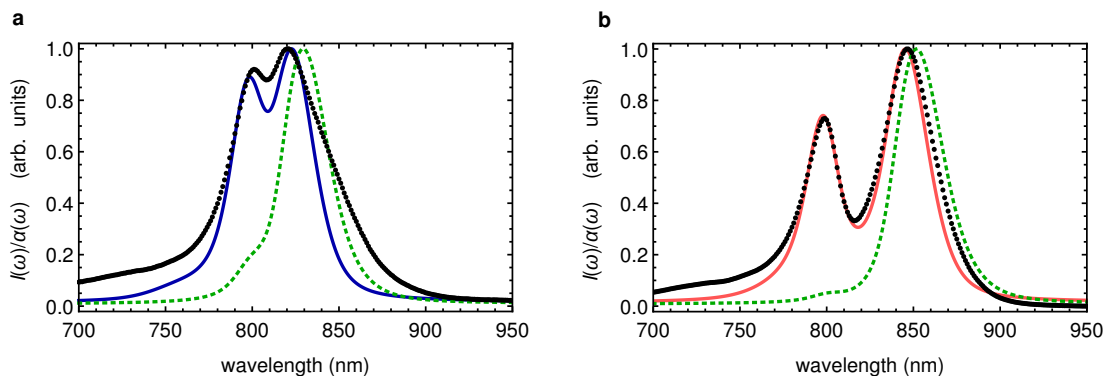


Figure 5.6: **(a)** Low light (B820) **(b)** High light (B850) absorption and fluorescence spectra. Black points are experimental absorption spectra. Solid red/blue curves are calculated absorption and dashed green curves are calculated fluorescence spectra. The shoulder of the low light absorption spectra is not well reproduced but could be LH1 complexes, incomplete adaptation or the influence of vibrational modes.

the second and third lowest exciton states share the total dipole strength strength [44]. Upon the inclusion of static disorder, the circular symmetry of the ring is partially lifted. As shown in Fig. 5.7, as the standard deviation  $\sigma$  of the normal distribution from which site energy perturbations are sampled increases, the lowest energy exciton state gains dipole strength while the second and third lowest energy exciton states lose dipole strength. Increases to static disorder in B820 sites and or adjustments of electronic parameters could improve the fit of the absorption spectra, but here we keep values equal for B850 and B820 for simplicity. The corresponding

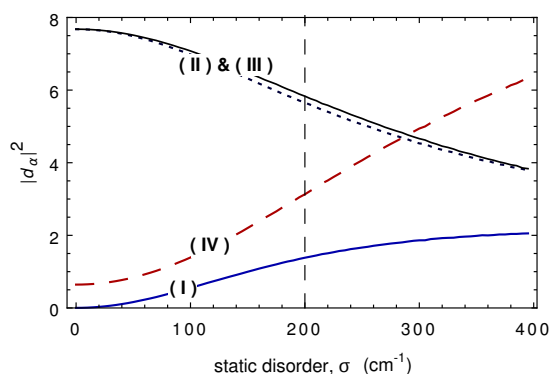


Figure 5.7: Mean dipole strength of exciton states in low light B820 as a function of the static disorder strength  $\sigma$ . Curves **(I)**, **(II)** and **(III)** are the dipole strength of the lowest, second and third lowest exciton states. Curve **(IV)** is the dipole strength of the remaining states. The dashed line at  $\sigma = 200 \text{ cm}^{-1}$  denotes the static disorder value used in calculations.

experimental fluorescence data for these samples is not available. In *acidophila* the B850 fluorescence maxima lies close to 870 nm [240, 241], whereas here the calculated fluorescence maxima of high light adapted *molischianum* lies close to 860 nm. This suggests that these calculations under-estimate the stokes shift between fluorescence and absorption in *molischianum*. The inclusion of high energy modes in the spectral density could account for some of this extra shift.

Calculations of the exact absorption spectra for the full LH2 complex (24 sites) using the HEOM method were attempted for a few realizations. The results are not displayed here as the maximum truncation possible (limited by available memory for this 24 site system) did not produce a converged result. However it was possible infer some inadequacies of the Redfield line shapes. In particular the peak associated with exciton states of B800 character is narrower which can be attributed to the under estimation of exciton lifetimes  $\tau_\alpha$  within Redfield theory. The use of modified Redfield theory to calculate the lifetimes of B800 states could be used to correct this deficiency [242]. However, in the present implementation of MRT, the integrals appearing in equation (1.25) are performed numerically. This is impractical in the present 24 site system given the need for many realizations of static disorder. Additionally, as discussed in section 5.2.1 the use of MRT in scenarios where environmental and electronic couplings are of the same order (as in the B850 and rings) can result in lifetimes which are even shorter than those predicted by Redfield. In [243] it is highlighted for a spectral density  $J_D(\omega)$  these integrals can be performed analytically using a continued fraction representation [244]. In future work this could be applied to efficiently calculate rates in mixed approach which uses different levels of theory according to the regime of electronic coupling. This approach has been applied to the LHCII complex [245].

#### 5.4.4 B800-B850 energy transfer

Generalized Förster theory (GFT) is used to calculate the rate of transfer between the B800 and B850 rings of the *molischianum* LH2 complex at room temperature. A number of studies have previously studied B800 to B850 energy transfer using GFT in *molischianum* at 77 K [232] and *acidophila* [228, 246]. Here, disorder arises from fluctuations of site energies due to protein motion as well as the stochastic assembly of acclimated complexes with heterogeneous  $\alpha$ - $\beta$  dimer composition. Fig. 5.8 displays the distribution of intra-complex energy transfer rates for complexes with homogeneous  $\alpha$ - $\beta$  dimer composition. The mean transfer rate for complexes acclimated to high light conditions (composed purely of B850  $\alpha$ - $\beta$  dimers) is  $1.14 \text{ ps}^{-1}$ ,

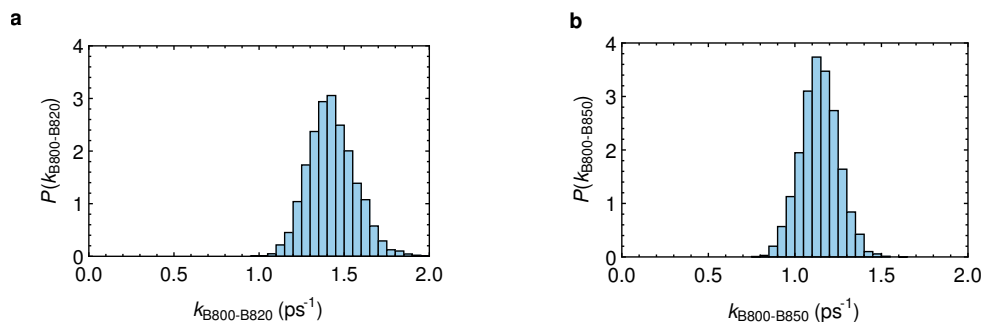


Figure 5.8: Distribution of *molischianum* LH2 intra-complex energy transfer rates, fully acclimated to (a) low light conditions (B800→B820) and (b) acclimated to high light conditions (B800→B850). 50000 realizations of static disorder.

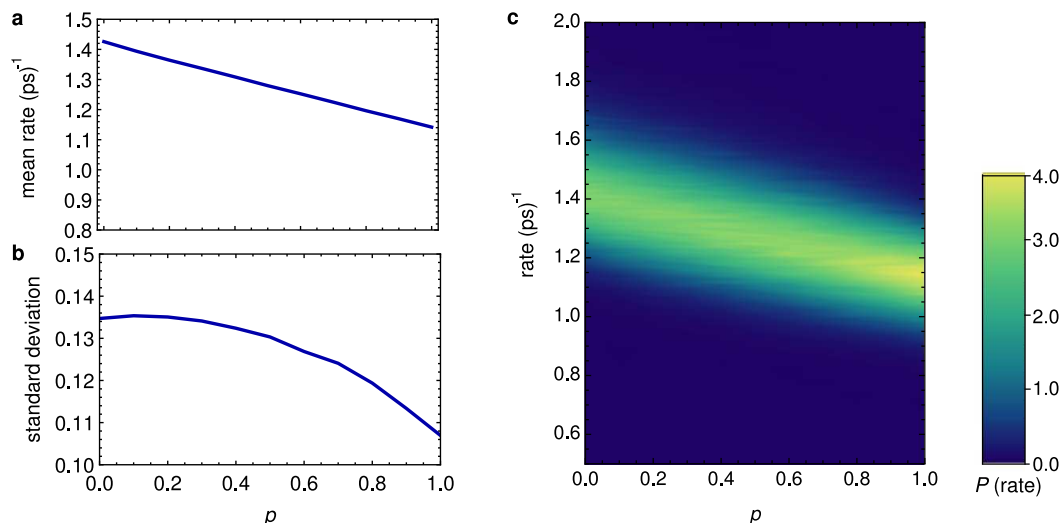


Figure 5.9: (a) Mean, (b) standard deviation and (c) probability density of intra-complex B800 → B850 transfer as a function of  $p$ .  $p = 0$  ( $p = 1$ ) corresponds to complexes composed only of B820 (B850) type  $\alpha$ - $\beta$  dimer.

which corresponds to a mean transfer time of 0.88 ps. This is consistent with room temperature experiments in the same species. A two color transient absorption measurement determined a transfer time of 0.9 ps [247], while modelling of three-pulse photon echo spectroscopy established a rate of 0.8 ps [248]. The mean transfer rate for complexes acclimated to low light conditions (composed purely of B820  $\alpha$ - $\beta$  dimers) is  $1.43 \text{ ps}^{-1}$  (transfer time - 0.7 ps). This increase in the transfer rate is consistent with experiment [249]. The increase arises from the decrease in energy gap between donating and accepting chromophore clusters - the spectral overlap of B800 fluorescence and B850 absorption excitonic line shapes is therefore increased leading to faster transfer of energy. The distribution of intra-complex energy transfer rates

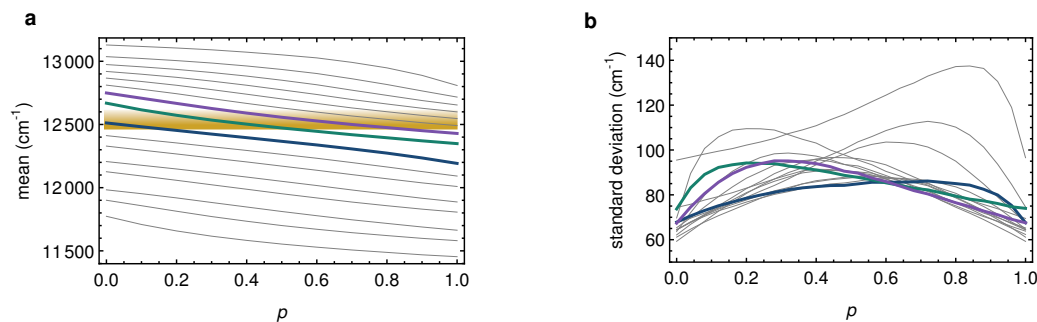


Figure 5.10: Statistics of the energies of excitonic states in the B850 ring of *molischianum* LH2 as a function of mixing parameter  $p$  for a static disorder  $\sigma_{\text{B850}} = 200 \text{ cm}^{-1}$  (50000 realizations). (a) Mean and (b) standard deviation. The yellow shading indicates the energy of the B800 band, and the B850 states with mean energy close to this band are highlighted in both figures.

for complexes with mixed apoprotein is displayed in Fig. 5.9c. The mean transfer rate decreases linearly with increasing  $p$ . This is because the B850 states which have most overlap with the lower B800 states have energies which on average, have a linear dependence on  $p$ . Fig. 5.10a displays the mean energies of the B850 ring as a function of  $p$ . The three exciton states closest to the B800 band are highlighted. As the B850 ring acclimates to low light intensities (smaller  $p$ ), the spectral overlap of these excitonic line shapes with the stationary B800 band must increase linearly. This explains the behaviour of the mean B800-B850 transfer rate with  $p$ .

Correspondingly Fig. 5.10b highlights that the standard deviation in the energies of these three states increases for intermediate  $p$ , displaying maxima at low values of  $p$ . Large deviations in the excitonic energies will result in large deviations in spectral overlap and hence transfer

This behaviour manifests in the standard deviation of transfer rates which decreases for smaller values of  $p$  and displays a maximum at  $p \sim 0.1$ .

#### 5.4.5 B800-B850 energy transfer dynamics

We now consider intra-complex energy transfer in a single  $\alpha$ - $\beta$  apoprotein dimer subunit from LH2 illustrated as in Fig. 5.2b. It contains three chromophores - the weakly electronically coupled B800 site and the strongly coupled B850 $\alpha$ -B850 $\beta$  dimer. Studying this reduced subunit of the full LH2 system in isolation does not capture all of the properties of the full ring but nevertheless allows some insights into the energy transfer dynamics. The small system size enables exact calculations of energy transfer dynamics using the HEOM method for many realizations of disorder.

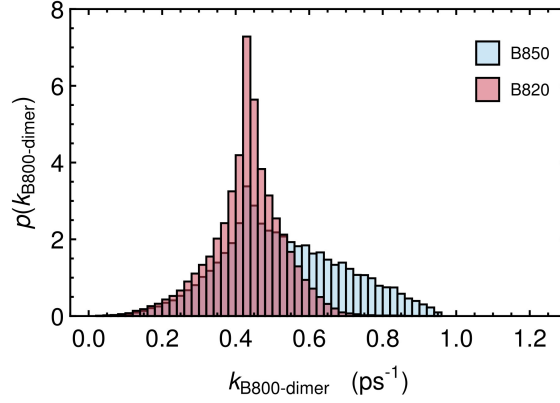


Figure 5.11: The distribution of transfer rates from the B800 chromophore to the B850/B820 dimer in the subunit of LH2 molischianum considered.

Analysis of experimental 2D spectra of a similar  $\alpha$ - $\beta$  apoprotein dimer isolated from the LH1 complex of *Rhodospirillum rubrum* has recently suggested that particular realizations of static disorder can bring energy gaps into resonance with vibrational modes [250]. The system has the electronic Hamiltonian

$$H_{\alpha-\beta\text{dimer}} = \begin{pmatrix} E_{\text{B800}} & V_{\text{B800}\alpha_1} & V_{\text{B800}\beta} \\ V_{\text{B800}\alpha_1} & E_{\text{B850}\alpha_1} & V_{\alpha_1\beta_1} \\ V_{\text{B800}\beta} & V_{\alpha_1\beta_1} & E_{\text{B850}\beta_1} \end{pmatrix}, \quad (5.10)$$

and local chromophore environments characterized by Drude spectral densities (as specified in earlier sections). *i.e.* not including any vibrational modes. Dynamics are simulated for 50000 realizations of disorder and the transfer rate from B800 to B850/B820 dimer is determined by fitting the dynamics of chromophore populations to a Pauli master equation. The energy is assumed to start localised on the B800 chromophore. Oscillations in the chromophore population dynamics are not present and therefore rates can be extracted for every realization of static disorder.

Fig. 5.11a displays the distribution of transfer rates from B800 site to the strongly coupled dimer (B850 or B20 depending on acclimation). The mean rates are  $0.529 \text{ ps}^{-1}$  and  $0.432 \text{ ps}^{-1}$  for B850 and B820 site energies respectively. These rates are more than half those predicted by GFT in the full LH2 ring, but also display the reverse trend - a slower transfer rate with acclimated to low light conditions. There is also a more pronounced difference the shape of B850 and B820 the distributions. The B850 distribution is broad, with a long tail up to rates of  $1.0 \text{ ps}^{-1}$  whereas the B820 distribution is narrower and more symmetric. The relates to the positioning of energy gaps within each of the two subunits. Note that the difference between

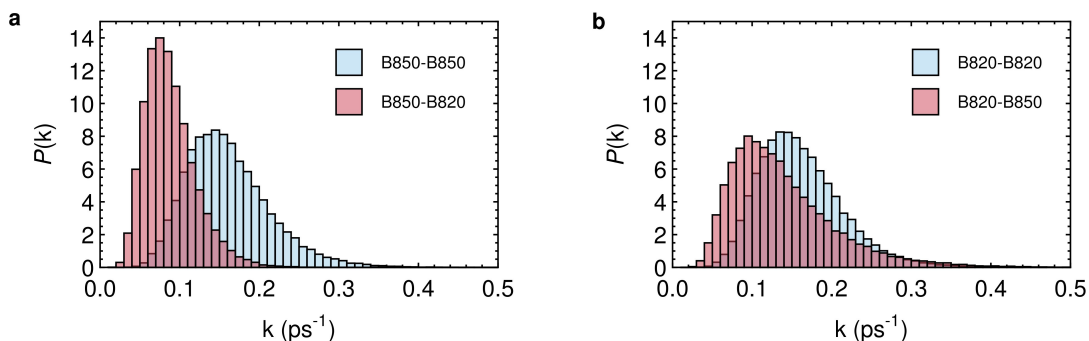


Figure 5.12: Distribution of transfer rates between LH2 complexes with homogeneous  $\alpha$ - $\beta$  apoprotein composition for transfer from (a) B850-B850, B850-B820, (b) B820-B820 and B820-B850.

B800 and B850/B820 dimer chromophore reorganisation energies means that the apparent energy gap between B800 and the dimer is reduced. This is a result of the counter term  $H^{\text{reorg}} = \sum_i \lambda_i \sigma_i^+ \sigma_i$ . In the B820 unit, static disorder does not result in the rare but favourable matching of energy gaps that is the origin of the long tail observed in the B850 unit. Most of these differences can be attributed to the neglect of the remaining sites of the ring. In the full ring there are many more nearby accepting B850 states with the possibility of resonance with B800 for a particular realization of disorder. Thus in the GFT calculations, the rates are faster and differences between the shape of the distribution for B850 and B820 are less pronounced. Additionally, as shown in Table 5.1, electronic coupling between B800 and B850 pigments in adjacent  $\alpha$ - $\beta$  dimers is actually larger than coupling to B850 within the same  $\alpha$ - $\beta$  dimer. This is due to favourable alignment of dipoles. Since B800 chromophores are significantly electronically coupled to chromophores in adjacent  $\alpha$ - $\beta$  dimers, it is necessary to consider the ring as a whole. This goes some way to explaining the reduced transfer rates obtained in this subunit.

## 5.5 Acclimation of inter-complex energy transfer

### 5.5.1 B850-B850 transfer rates

Generalized Förster theory is used to calculate the rate of energy transfer between adjacent LH2 complexes from *molischianum* at room temperature. The energy transfer dynamics between LH2 complexes of *acidophila* has been studied using the HEOM method for a single realization of disorder [239], where GFT was found to give an adequate description of transfer rates. This justifies the current use

of GFT, which additionally enables calculations of many realizations of energetic disorder arising from slow protein motions as well as the stochastic assembly of acclimated complexes with heterogeneous  $\alpha$ - $\beta$  dimer composition. The arrangement of chromophores is taken from [206] which results in a LH2 centre-to-centre distance of 70 Å. Inter-complex couplings are calculated in the point dipole approximation.

Fig. 5.12 displays the resulting distribution of transfer rates between complexes of homogeneous  $\alpha$ - $\beta$  dimer composition. The mean rates for B850-B850 and B820-B820 transfer are  $0.161 \text{ ps}^{-1}$  (6.22 ps) and  $0.160 \text{ ps}^{-1}$  (6.24 ps) respectively. Using conventional Förster theory, previous work [251] predicted transfer times of 10.0 ps and 11.3 ps for B850-B850 and B820-B820 transfer respectively. In acidophila, HEOM calculations for a single realization of disorder predicted 9.1ps [239]. Recently LH2-LH2 transfer has also been calculated in *Rhodospirillum photometricum* using the HEOM method, yielding transfer times of *e.g.* 4.3 ps, 6.3 ps and 5.3 ps [252]. These times arise from different in LH2 centre-to-centre distances which are also known to vary within an assembled membrane as can easily be seen in the AFM image of membrane topology in Fig. 5.1a. The transfer rates calculated here are consistent with those predicted by previous theoretical works. The similarity of the transfer rates B820-B820 and B850-B850 could be anticipated.. Unlike the case of B800 to B850/B820 transfer explored in section 5.4.4, the energies of both donating and receiving chromophore clusters are shifted. Thus on average, spectral overlaps are similar as both fluorescence and absorption are shifted by the same amount.

Regarding the acclimation of energy transfer within a membrane, a general observation can be made about relative rates of transfer between complexes of homogeneous  $\alpha$ - $\beta$  dimer composition which does not necessarily depend on absolute accuracy of transfer rates. Without the mixing of antennae proteins, during acclimation to lower light conditions membranes will contain LH2 complexes of pure B820 type adjacent to pure B850 type complexes. The mean transfer rates from B820-B850 and B850-B820 are  $0.138 \text{ ps}^{-1}$  and  $0.090 \text{ ps}^{-1}$  respectively. These rates of transfer mean that close to full adaptation when a membrane is mainly composed of B820 type complexes, the remaining B850 complexes represent an energetic trap which the excitation can transfer into more rapidly than it can transfer out. This inhibits the path of the excitation towards an LH1 complex. The *molischianum* species does not adapt to low light conditions in this way, instead for a particular level of adaptation  $p$ , membranes contain complexes of heterogeneous  $\alpha$ - $\beta$  dimer composition. The variation of the mean transfer rate with  $p$  is displayed in 5.13a.



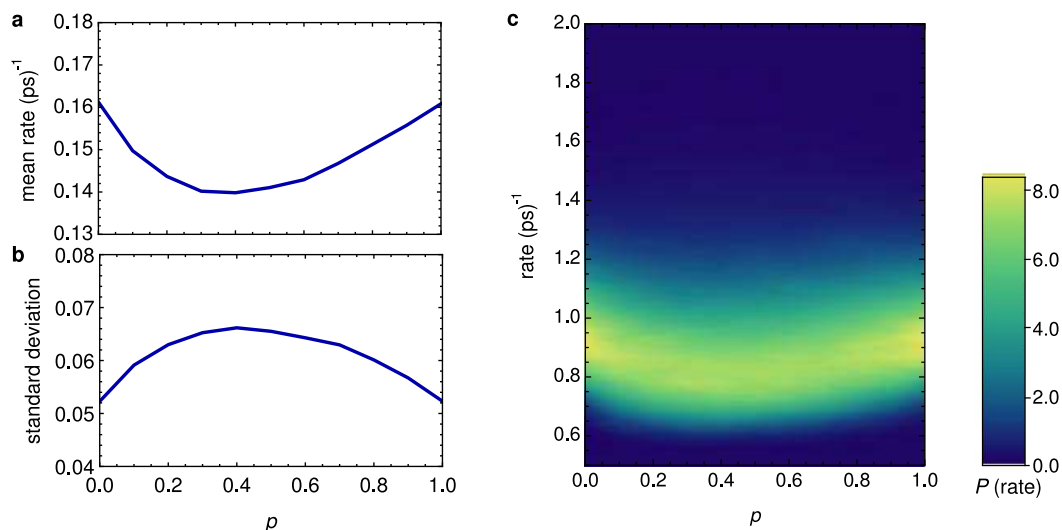


Figure 5.13: (a) Mean, (b) standard deviation and (c) probability density of inter-complex B850  $\rightarrow$  B850 transfer for spectrally heterogeneous complexes with  $\alpha$ - $\beta$  apoprotein composition determined by  $p$ .  $p = 0$  ( $p = 1$ ) corresponds to complexes composed only of B820 (B850) type  $\alpha$ - $\beta$  dimer.

The minimum transfer rate is  $\sim 0.14 \text{ ps}^{-1}$  and thus the additional energetic disorder introduced by antennae mixing alleviates the energetic traps discussed. At intermediate levels of adaptation ( $p \neq 0, 1$ ), the width of the distribution of rates increases. This is to be expected - the additional disorder arising from antennae mixing causes more variation in the spectral overlaps of excitonic line shapes. Intriguingly, this disorder is not maximized at  $p = 0.5$  as might be naively anticipated. The standard deviation of B850 energies as a function of  $p$  displayed in 5.10b goes some way to explaining this. Lower energy levels feature a maxima in standard deviation at  $p < 0.5$ , while higher energy levels feature a maxima at  $p > 0.5$ . Since the donor aggregate is assumed to reach thermal populations before inter-complex transfer takes place, the disorder in lower energy B850 states is emphasized. Thus, transfer rates between complexes with  $p < 0.5$  feature more disorder than those with  $p > 0.5$ .

## 5.6 Concluding remarks and outlook

Energy transfer within and between LH2 complexes from *molischianum* is influenced by the changes in apoprotein type composition which take place during acclimation to lower light levels. By modelling energy transfer with generalized Förster theory which correctly describes the delocalised nature of the excited states of donor and acceptor chromophore groups, we have been able to make quantitative statements

about the acclimation of energy transfer statistics. At low light intensities, we found that the rate of intra-complex transfer from B800 to B850 rings increases as the B850 ring shifts energetically closer, increasing the spectral overlap. At the same time the distribution of transfer rates broadens, reflecting the sensitivities of particular accepting exciton states (lying energetically close to the B800 band) to the disorder. We explored energy transfer rates predicted by the accurate HEOM technique in a small subunit of the LH2. The results were found to be inconsistent with GFT calculations in the full system, demonstrating the importance of the coupling of B800 sites to multiple  $\alpha$ - $\beta$  dimer pairs. Large tails in the distribution of transfer rates were attributed to rare energetic alignment events, which are far less significant when the all states associated with the full B850 ring are considered.

The environments of B800 and B850 chromophores are known to features intra-molecular vibrational modes. In particular specific under-damped high energy modes have been identified [48, 231, 253]. The inclusion of strong coupling to such modes is expected to alter the distribution of transfer rates. For certain realizations of static disorder, the energy differences between B800 and B850 excitonic states will be quasi-resonant with high energy vibrational modes. This will result in excitation dynamics not properly characterized by a transfer rate - for example featuring exciton population oscillations, or non-exponentiality. Since high energy modes have been identified, the non-classicality of the vibrational modes may assist transfer for some realizations of disorder. Acclimation to low light intensities in *molischianum* alters the distribution of disorder, bringing more (or less) realizations into quasi-resonance with vibrations and thus may increase/decrease the extent to which non-classicality is harnessed. This causes us to speculate - does the acclimation of inter-complex energy transfer in LH2 exploit non-classicality? We anticipate that accurate HEOM calculations including vibrational modes can shed light on the acclimation of non-classicality for specific realizations of disorder.

Our GFT calculations of inter-complex transfer have also revealed the importance of heterogeneous  $\alpha$ - $\beta$  apoprotein composition for transport across photosynthetic membranes. Intra-complex transfer is accelerated in low light adapted complexes, yet the statistics of energy transfer rates between high and low light adapted complexes of the same type are similar (with mean rates  $\sim 0.16$  ps<sup>-1</sup>).

However, the mean transfer rates from complexes composed purely of one type of  $\alpha$ - $\beta$  apoprotein to a complex composed purely of another are reduced. The mixing of high and low type  $\alpha$ - $\beta$  apoprotein types within a complex helps to alleviate this problem. The stochastic assembly of complexes determined by the parameter  $p$ ,

means that adjacent high and low light complexes of homogeneous  $\alpha$ - $\beta$  composition are unlikely. Thus, the energetic disorder introduced mixing of high and low type alpha-beta apoprotein types within LH2 complexes allows for a smoother energetic landscape at the level of the photosynthetic membrane during the acclimation to lower light intensities. Intra-complex transfer is accelerated without to inter-complex transfer and more macroscopic transport across photosynthetic membrane. This insight can be further investigated within kinetic models of energy migration at the level of the photosynthetic membranes.

## 5.A LH2 structural data

	$r_x$	$r_y$	$r_z$
B800 <sub>1</sub>	72.062	-12.081	-90.095
B800 <sub>2</sub>	72.913	9.924	-90.122
B800 <sub>3</sub>	57.881	26.262	-90.095
B800 <sub>4</sub>	35.876	27.113	-90.122
B800 <sub>5</sub>	19.538	12.081	-90.095
B800 <sub>6</sub>	18.687	-9.924	-90.122
B800 <sub>7</sub>	33.719	-26.262	-90.095
B800 <sub>8</sub>	55.724	-27.113	-90.122
B850 $\alpha$ <sub>1</sub>	55.911	-20.536	-72.269
B850 $\beta$ <sub>1</sub>	63.758	-15.433	-72.089
B850 $\alpha$ <sub>2</sub>	67.471	-7.476	-72.296
B850 $\beta$ <sub>2</sub>	69.411	1.682	-72.116
B850 $\alpha$ <sub>3</sub>	66.336	10.111	-72.269
B850 $\beta$ <sub>3</sub>	61.233	17.958	-72.089
B850 $\alpha$ <sub>4</sub>	53.276	21.671	-72.296
B850 $\beta$ <sub>4</sub>	44.118	23.611	-72.116
B850 $\alpha$ <sub>5</sub>	35.689	20.536	-72.269
B850 $\beta$ <sub>5</sub>	27.842	15.433	-72.089
B850 $\alpha$ <sub>6</sub>	24.129	7.476	-72.296
B850 $\beta$ <sub>6</sub>	22.189	-1.682	-72.116
B850 $\alpha$ <sub>7</sub>	25.264	-10.111	-72.269
B850 $\beta$ <sub>7</sub>	30.367	-17.958	-72.089
B850 $\alpha$ <sub>8</sub>	38.324	-21.671	-72.296
B850 $\beta$ <sub>8</sub>	47.482	-23.611	-72.116

Table 5.A.1: Positions  $\mathbf{r}_i$ , of central Mg atoms of the BChl chromophores of the LH2 complex from *Phaeospirillum molischianum* as determined from 1LGH.

	$d_x$	$d_y$	$d_z$
B800 <sub>1</sub>	-0.823073	-0.524628	-0.217523
B800 <sub>2</sub>	-0.211081	-0.952959	-0.217515
B800 <sub>3</sub>	0.524628	-0.823073	-0.217523
B800 <sub>4</sub>	0.952959	-0.211081	-0.217515
B800 <sub>5</sub>	0.823073	0.524628	-0.217523
B800 <sub>6</sub>	0.211081	0.952959	-0.217515
B800 <sub>7</sub>	-0.524628	0.823073	-0.217523
B800 <sub>8</sub>	-0.952959	0.211081	-0.217515
B850 $\alpha_1$	0.981526	0.14405	-0.125919
B850 $\beta_1$	-0.927041	-0.354464	-0.122272
B850 $\alpha_2$	0.592081	0.795981	-0.125916
B850 $\beta_2$	-0.405016	-0.9061	-0.122246
B850 $\alpha_3$	-0.14405	0.981526	-0.125919
B850 $\beta_3$	0.354464	-0.927041	-0.122272
B850 $\alpha_4$	-0.795981	0.592081	-0.125916
B850 $\beta_4$	0.9061	-0.405016	-0.122246
B850 $\alpha_5$	-0.981526	-0.14405	-0.125919
B850 $\beta_5$	0.927041	0.354464	-0.122272
B850 $\alpha_6$	-0.592081	-0.795981	-0.125916
B850 $\beta_6$	0.405016	0.9061	-0.122246
B850 $\alpha_7$	0.14405	-0.981526	-0.125919
B850 $\beta_7$	-0.354464	0.927041	-0.122272
B850 $\alpha_8$	0.795981	-0.592081	-0.125916
B850 $\beta_8$	-0.9061	0.405016	-0.122246

Table 5.A.2: Dipole moment direction unit vectors  $\hat{\mathbf{d}}_i$  the BChl chromophores of the LH2 complex from *Phaeospirillum molischianum* as determined from NB to ND nitrogen atoms.

# Chapter 6

## Final Remarks and Outlook

This thesis has been devoted to investigation of non-trivial quantum features of light initiated dynamics in light harvesting systems.

In Chapter 1 we reviewed the necessary theoretical framework for the description of dynamics in biomolecular systems. In particular we outlined the hierarchical equations of motion approach which while being numerically intensive, can generate accurate dynamics for any regime of coupling strengths. We also reviewed measures of the quantum traits of both electronic and vibrational dynamics.

In Chapter 2 we investigated exciton-vibration dynamics in a prototype system typical of those found in a variety of light harvesting antennae. By extending the hierarchical equations of motion to include a quantized mode, we were able to demonstrate that non-classicality of specific vibrational motions results in enhanced transport. We found that phonon number statistics violate classical bounds, due to the coherent exchange of energy with electronic degrees of freedom. The non-classical states resemble single-phonon added thermal states, whose non-classicality was unambiguously illustrated by the appearance of negative regions in a phase space representation. Vibrational motion is at play in a variety of processes in biomolecules. In photosynthesis, vibrations are also known to sustain coherence during the charge-separation process in reaction centres [254]. There are suggestions that olfactory reception - the process of molecular recognition, long thought to be characterised in terms of a “lock-and-key” model has a vibrational sensing component [153, 154]. Experiments [155] have shown that the fruit fly *Drosophila melanogaster* can be trained to discriminate between deuterated and undeuterated odourants. The replacement of hydrogen with deuterium causes no change to structure of the molecule, but significantly alters its vibrational modes. Indeed flies trained to avoid a particular deuterated compound went on to avoid unrelated molecules with vibrational modes in the same frequency range. Specific intramolecular vibrational motions are

---

also driven out of thermal equilibrium during the light-initiated electronic dynamics during the isomerization of photoreceptors [152]. Vibrations are ubiquitous in biology, often playing a role in the function of the system. The importance of non-classicality of vibrations we have identified in light harvesting systems, may have broader implications for the field of quantum biology.

Vibrations are often treated classically, but the results of Chapter 2 highlight the breakdown of such an approximation. Classical physics is not always adequate to describe the dynamics of energy transfer in these systems. In Chapter 3 we imposed a classical description of vibrational modes and found qualitative differences in the resulting excitonic dynamics in two cryptophyte marine algae species. The classical model of vibrations employed is less able to direct energy towards particular chromophores, does not predict the oscillatory transfer of energy between the electronic and vibrational components seen with quantized vibrations and cannot account correctly for storage of energy in vibrations. This suggests that in other biomolecular systems quantized vibrations could enable or enhance functional features of dynamics. For example in olfaction, the response of an olfactory system (or artificial bio-inspired equivalent) to odourants featuring particular intra-molecular motions may be enhanced by the quantized nature of the vibrations.

In Chapter 4 we considered the role that thermodynamics may play when vibrations are treated in a quantum mechanical setting. The study of thermodynamics in the quantum regime is an active and ongoing area of research and may have many practical applications in addition to providing an increased understanding of fundamental physics. Applying these concepts to biomolecular systems is of particular interest as they have evolved to perform a specific function. Differences between species (as well as variations introduced by mutagenesis) provides a test bed of systems with the same biological function which feature different interactions. We considered the differences in thermodynamic behaviour for complexes from two marine algae species, PE545 which contains only weakly electronically coupled chromophores and PC645 which features a strongly electronically coupled dimer. The formalism adopted in Chapter 4 identified work-like and heat-like contributions to the energy flux between electronic and vibrational degrees of freedom. We found that the relative nature of energy fluxes is dependent on the strength of electronic coupling between chromophores. In particular we have shown that in the PE545 system the combined exciton-vibration dynamics results in energy exchanges with vibrations which are predominantly work-like. The more strongly electronically coupled central dimer of PC645 introduces a significant heat-like component to energy

---

fluxes. A classical description of vibrations supposes that they only drives a time dependence of electronic site energies. This type of driving implies an entirely work-like energy flux. The degree to which a classical description of vibrations is appropriate dictates the thermodynamic nature of energy fluxes in biomolecular systems. We also showed by properly accounting for the compatibility of energy measurements, that a work-like energy flux between electronic and vibrational degrees of freedom can arise under continuous illumination due to a non-equilibrium steady state. Under natural illumination, the rate of excitation input for light harvesting systems is low. This does not drive the system far from equilibrium and results in a small work flux, which does not have any obvious biological role. Nevertheless, the steady state work fluxes identified in these photosynthetic prototypes would be important in an artificial system, for example one exploiting a structured environment and driven by a laser source. The emergence of quantum technologies will surely mean that the consideration of quantum thermodynamics will be of increasing importance.

In Chapter 5 we investigated how the acclimation of purple bacteria to different light intensities affects energy transfer. Changes in the apoprotein composition of LH2 complexes which occur when light levels are altered results in a different electronic energy landscape. Using generalized Förster theory we showed that this accelerated intra-complex energy transfer without detriment to inter-complex energy transfer. The disorder introduced by the assembly of antennae with mixed apoprotein composition reduces the likelihood of energetic traps appearing in the photosynthetic membrane. Energy transfer was characterized according to rates and the influence of vibrational modes was not accounted for. Resonance with vibrations known to be present in these systems may alter the nature of intra-complex energy transfer. Being high in energy, it is likely that the non-classicality of these vibrations may manifest and enhance the B800-B850 inter-band energy transfer in LH2. Acclimation of the energy transfer the landscape resulting from the changes in apoprotein composition may promote or diminish resonances with these vibrations. This suggests that acclimation may serve to exploit non-trivial quantum phenomena.



# References

- [1] Fleming, G. R., Scholes, G. D. & Cheng, Y.-C. Quantum effects in biology. *Procedia Chem.* **3**, 38–57 (2011). 22nd Solvay Conference on Chemistry.
- [2] Lambert, N. *et al.* Quantum biology. *Nat. Phys.* **9**, 10–18 (2013).
- [3] Huelga, S. F. & Plenio, M. B. Vibrations, quanta and biology. *Contemp. Phys.* **54**, 181–207 (2013).
- [4] Blankenship, R. *Molecular Mechanisms of Photosynthesis* (Wiley, 2008).
- [5] Förster, T. Energiewanderung und fluoreszenz. *Naturwissenschaften* **33**, 166–175 (1946).
- [6] Förster, T. Zwischenmolekulare energiewanderung und fluoreszenz. *Annalen der Physik* **437**, 55–75 (1948).
- [7] Förster, T. 10th spiels memorial lecture. transfer mechanisms of electronic excitation. *Discuss. Faraday Soc.* **27**, 7–17 (1959).
- [8] Kenkre, V. & Knox, R. Optical spectra and exciton coherence. *J. Lumin.* **12-13**, 187–193 (1976).
- [9] Nedbal, L. & Szöcs, V. How long does excitonic motion in the photosynthetic unit remain coherent? *Journal of Theoretical Biology* **120**, 411–418 (1986).
- [10] Engel, G. S. *et al.* Evidence for wavelike energy transfer through quantum coherence in photosynthetic systems. *Nature* **446**, 782–786 (2007).
- [11] Lee, H., Cheng, Y.-C. & Fleming, G. R. Coherence dynamics in photosynthesis: Protein protection of excitonic coherence. *Science* **316**, 1462–1465 (2007).
- [12] Calhoun, T. R. *et al.* Quantum coherence enabled determination of the energy landscape in light-harvesting complex II. *J. Phys. Chem. B* **113**, 16291–16295 (2009).
- [13] Collini, E. *et al.* Coherently wired light-harvesting in photosynthetic marine algae at ambient temperature. *Nature* **463**, 644–647 (2010).

- 
- [14] Panitchayangkoon, G. *et al.* Long-lived quantum coherence in photosynthetic complexes at physiological temperature. *Proc. Natl. Acad. Sci. USA* **107**, 12766–12770 (2010).
- [15] Harel, E. & Engel, G. S. Quantum coherence spectroscopy reveals complex dynamics in bacterial light-harvesting complex 2 (LH2). *Proc. Natl. Acad. Sci. USA* **109**, 706–711 (2012).
- [16] Hildner, R., Brinks, D., Nieder, J. B., Cogdell, R. J. & van Hulst, N. F. Quantum coherent energy transfer over varying pathways in single light-harvesting complexes. *Science* **340**, 1448–1451 (2013).
- [17] Fuller, F. D. *et al.* Vibronic coherence in oxygenic photosynthesis. *Nat. Chem.* doi:10.1038/nchem.2005 (2014).
- [18] Werner, H., Schulten, Z. & Schulten, K. Theory of the magnetic field modulated geminate recombination of radical ion pairs in polar solvents: Application to the pyrene-n,n-dimethylaniline system. *J. Chem. Phys.* **67**, 646–663 (1977).
- [19] Schulten, K., Swenberg, C. E. & Weller, A. A biomagnetic sensory mechanism based on magnetic field modulated coherent electron spin motion. *Z. Phys. Chem.* **111**, 1–5 (1978).
- [20] Ritz, T., Adem, S. & Schulten, K. A model for photoreceptor-based magnetoreception in birds. *Biophys. J.* **78**, 707–718 (2000).
- [21] Fusani, L., Bertolucci, C., Frigato, E. & Foà, A. Cryptochrome expression in the eye of migratory birds depends on their migratory status. *J. Exp. Biol.* **217**, 918–923 (2014).
- [22] Ritz, T., Ahmad, M., Mouritsen, H., Wiltschko, R. & Wiltschko, W. Photoreceptor-based magnetoreception: optimal design of receptor molecules, cells, and neuronal processing. *J. R. Soc., Interface* **7**, S135–S146 (2010).
- [23] Gauger, E. M., Rieper, E., Morton, J. J. L., Benjamin, S. C. & Vedral, V. Sustained quantum coherence and entanglement in the avian compass. *Phys. Rev. Lett.* **106**, 040503 (2011).
- [24] Stoneham, A., Gauger, E., Porfyrakis, K., Benjamin, S. & Lovett, B. A new type of radical-pair-based model for magnetoreception. *Biophys. J.* **102**, 961–968 (2012).
- [25] Cai, J. & Plenio, M. B. Chemical compass model for avian magnetoreception as a quantum coherent device. *Phys. Rev. Lett.* **111**, 230503 (2013).
- [26] Phillips, J. B. & Borland, S. C. Behavioural evidence for use of a light-dependent magnetoreception mechanism by a vertebrate. *Nature* **359**, 142–144 (1992).

- 
- [27] Ritz, T., Thalau, P., Phillips, J. B., Wiltschko, R. & Wiltschko, W. Resonance effects indicate a radical-pair mechanism for avian magnetic compass. *Nature* **429**, 177–180 (2004).
- [28] Wiltschko, R., Stapput, K., Thalau, P. & Wiltschko, W. Directional orientation of birds by the magnetic field under different light conditions. *J. R. Soc., Interface* **7**, S163–S177 (2010).
- [29] Ritz, T. *et al.* Magnetic compass of birds is based on a molecule with optimal directional sensitivity. *Biophys. J.* **96**, 3451–3457 (2009).
- [30] Phan, N. M., Cheng, M. F., Bessarab, D. A. & Krivitsky, L. A. Interaction of fixed number of photons with retinal rod cells. *Phys. Rev. Lett.* **112**, 213601 (2014).
- [31] Sia, P. I., Luiten, A. N., Stace, T. M., Wood, J. P. & Casson, R. J. Quantum biology of the retina. *Clin. Exp. Ophthalmol.* **42**, 582–589 (2014).
- [32] Prokhorenko, V. I. *et al.* Coherent control of retinal isomerization in bacteriorhodopsin. *Science* **313**, 1257–1261 (2006).
- [33] Prokhorenko, V. I., Nagy, A. M., Brown, L. S. & Dwayne Miller, R. On the mechanism of weak-field coherent control of retinal isomerization in bacteriorhodopsin. *Chem. Phys.* **341**, 296–309 (2007).
- [34] Ulanowicz, R. E. & Hannon, B. M. Life and the production of entropy. *Proc. R. Soc. B* **232**, 181–192 (1987).
- [35] Jarzynski, C. Nonequilibrium equality for free energy differences. *Phys. Rev. Lett.* **78**, 2690–2693 (1997).
- [36] Crooks, G. E. Entropy production fluctuation theorem and the nonequilibrium work relation for free energy differences. *Phys. Rev. E* **60**, 2721–2726 (1999).
- [37] Kolli, A., O’Reilly, E. J., Scholes, G. D. & Olaya-Castro, A. The fundamental role of quantized vibrations in coherent light harvesting by cryptophyte algae. *J. Chem. Phys.* **137**, 174109 (2012).
- [38] O’Reilly, E. J. & Olaya-Castro, A. Non-classicality of the molecular vibrations assisting exciton energy transfer at room temperature. *Nat. Commun.* **5** (2014).
- [39] Hossein-Nejad, H., Albert, V. V., O’Reilly, E. J. & Scholes, G. D. Corrigendum: Energy transfer, entanglement and decoherence in a molecular dimer interacting with a phonon bath (2010 new j. phys. 12 065045). *New J. Phys.* **16**, 019502 (2014).
- [40] Viani, L. *et al.* Molecular basis of the exciton-phonon interactions in the PE545 light-harvesting complex. *Phys. Chem. Chem. Phys.* **16**, 16302–16311 (2014).

- 
- [41] Sakurai, J. J. *Modern Quantum Mechanics* (Addison Wesley, 1993).
- [42] Breuer, H. & Petruccione, F. *The Theory of Open Quantum Systems* (Oxford University Press, 2002).
- [43] Weiss, U. *Quantum Dissipative Systems*. Series in modern condensed matter physics (World Scientific, 2012).
- [44] May, V. & Kühn, O. *Charge and Energy Transfer Dynamics in Molecular Systems* (Wiley, 2011).
- [45] Renger, T., May, V. & Kühn, O. Ultrafast excitation energy transfer dynamics in photosynthetic pigment-protein complexes. *Phys. Rep.* **343**, 137–254 (2001).
- [46] Krueger, B. P., Scholes, G. D. & Fleming, G. R. Calculation of couplings and energy-transfer pathways between the pigments of LH2 by the ab initio transition density cube method. *J. Phys. Chem. B* **102**, 5378–5386 (1998).
- [47] Schatz, G. & Ratner, M. *Quantum Mechanics in Chemistry*. Dover Books on Chemistry (Dover Publications, 2012).
- [48] Damjanović, A., Kosztin, I., Kleinekathöfer, U. & Schulten, K. Excitons in a photosynthetic light-harvesting system: A combined molecular dynamics, quantum chemistry, and polaron model study. *Phys. Rev. E* **65**, 031919 (2002).
- [49] Onuchic, J. & da Gama, A. Influence of intersite modes on the exchange interaction in electron transfer at large distances. *Theor. Chim. Acta* **69**, 89–100 (1986).
- [50] Daizadeh, I., Medvedev, E. S. & Stuchebrukhov, A. A. Effect of protein dynamics on biological electron transfer. *Proc. Natl. Acad. Sci. USA* **94**, 3703–3708 (1997).
- [51] Skourtis, S. S., Waldeck, D. H. & Beratan, D. N. Fluctuations in biological and bioinspired electron-transfer reactions. *Annu. Rev. Phys. Chem.* **61**, 461–485 (2010).
- [52] Feynman, R. & Jr., F. V. The theory of a general quantum system interacting with a linear dissipative system. *Ann. Phys.* **24**, 118–173 (1963).
- [53] Yan, Y. & Xu, R. Quantum mechanics of dissipative systems. *Annu. Rev. Phys. Chem.* **56**, 187–219 (2005).
- [54] Nitzan, A. *Chemical Dynamics in Condensed Phases : Relaxation, Transfer and Reactions in Condensed Molecular Systems: Relaxation, Transfer and Reactions in Condensed Molecular Systems*. Oxford Graduate Texts (OUP Oxford, 2006).

- 
- [55] Peterman, E. J. G., Pullerits, T., van Grondelle, R. & van Amerongen, H. Electron-phonon coupling and vibronic fine structure of light-harvesting complex II of green plants: Temperature dependent absorption and high-resolution fluorescence spectroscopy. *J. Phys. Chem. B* **101**, 4448–4457 (1997).
- [56] Creemers, T. M. H., De Caro, C. A., Visschers, R. W., van Grondelle, R. & Völker, S. Spectral hole burning and fluorescence line narrowing in subunits of the light-harvesting complex LH1 of purple bacteria. *J. Phys. Chem. B* **103**, 9770–9776 (1999).
- [57] Wendling, M. *et al.* Electron-vibrational coupling in the Fenna-Matthews-Olson complex of *prosthecochloris aestuarii* determined by temperature-dependent absorption and fluorescence line-narrowing measurements. *J. Phys. Chem. B* **104**, 5825–5831 (2000).
- [58] Mirkovic, T. *et al.* Ultrafast light harvesting dynamics in the cryptophyte phycocyanin 645. *Photochem. Photobiol. Sci.* **6**, 964–975 (2007).
- [59] Renger, T. & Marcus, R. A. On the relation of protein dynamics and exciton relaxation in pigment-protein complexes: An estimation of the spectral density and a theory for the calculation of optical spectra. *J. Chem. Phys.* **116**, 9997–10019 (2002).
- [60] Adolphs, J. & Renger, T. How proteins trigger excitation energy transfer in the FMO complex of green sulfur bacteria. *Biophys. J* **91**, 2778–2797 (2006).
- [61] Olbrich, C., Strümpfer, J., Schulten, K. & Kleinekathöfer, U. Theory and simulation of the environmental effects on FMO electronic transitions. *J. Phys. Chem. Lett.* **2**, 1771–1776 (2011).
- [62] Rivera, E., Montemayor, D., Masia, M. & Coker, D. F. Influence of site-dependent pigment-protein interactions on excitation energy transfer in photosynthetic light harvesting. *J. Phys. Chem. B* **117**, 5510–5521 (2013).
- [63] Aghtar, M., Strümpfer, J., Olbrich, C., Schulten, K. & Kleinekathöfer, U. The FMO complex in a glycerol-water mixture. *J. Phys. Chem. B* **117**, 7157–7163 (2013).
- [64] Kell, A., Feng, X., Reppert, M. & Jankowiak, R. On the shape of the phonon spectral density in photosynthetic complexes. *J. Phys. Chem. B* **117**, 7317–7323 (2013).
- [65] Leggett, A. J. *et al.* Dynamics of the dissipative two-state system. *Rev. Mod. Phys.* **59**, 1 (1987).
- [66] Kreisbeck, C. & Kramer, T. Long-lived electronic coherence in dissipative exciton dynamics of light-harvesting complexes. *J. Phys. Chem. Lett.* **3**, 2828–2833 (2012).

- 
- [67] Chin, A. W. *et al.* The role of non-equilibrium vibrational structures in electronic coherence and recoherence in pigment-protein complexes. *Nat. Phys.* **9**, 113–118 (2013).
- [68] Mukamel, S. *Principles of nonlinear optical spectroscopy*. Oxford series in optical and imaging sciences (Oxford University Press, 1995).
- [69] Croy, A. & Saalman, U. Partial fraction decomposition of the fermi function. *Phys. Rev. B* **80**, 073102 (2009).
- [70] Redfield, A. G. On the theory of relaxation processes. *IBM J. Res. Dev.* **1**, 19–31 (1957).
- [71] Cheng, Y.-C. & Fleming, G. R. Dynamics of light harvesting in photosynthesis. *Annu. Rev. Phys. Chem.* **60**, 241–262 (2009).
- [72] Ishizaki, A. & Fleming, G. R. On the adequacy of the Redfield equation and related approaches to the study of quantum dynamics in electronic energy transfer. *J. Chem. Phys.* **130**, 234110 (2009).
- [73] Okada, A., Chernyak, V. & Mukamel, S. Solvent reorganization in long-range electron transfer: A density matrix approach. *J. Phys. Chem. A* **102**, 1241–1251 (1998).
- [74] Zhang, W. M., Meier, T., Chernyak, V. & Mukamel, S. Exciton-migration and three-pulse femtosecond optical spectroscopies of photosynthetic antenna complexes. *J. Chem. Phys.* **108**, 7763–7774 (1998).
- [75] Yang, M. & Fleming, G. R. Influence of phonons on exciton transfer dynamics: comparison of the Redfield, Förster, and modified Redfield equations. *Chem. Phys.* **275**, 355–372 (2002).
- [76] Ai, Q., Yen, T.-C., Jin, B.-Y. & Cheng, Y.-C. Clustered geometries exploiting quantum coherence effects for efficient energy transfer in light harvesting. *J. Phys. Chem. Lett.* **4**, 2577–2584 (2013).
- [77] Sahoo, H. Förster resonance energy transfer A spectroscopic nanoruler: Principle and applications. *Journal of Photochemistry and Photobiology C: Photochemistry Reviews* **12**, 20–30 (2011).
- [78] Tanimura, Y. & Kubo, R. Time evolution of a quantum system in contact with a nearly Gaussian-markoffian noise bath. *J. Phys. Soc. Jpn.* **58**, 101–114 (1989).
- [79] Ishizaki, A. & Fleming, G. R. Unified treatment of quantum coherent and incoherent hopping dynamics in electronic energy transfer: Reduced hierarchy equation approach. *J. Chem. Phys.* **130**, 234111 (2009).

- 
- [80] Shi, Q., Chen, L., Nan, G., Xu, R.-X. & Yan, Y. Efficient hierarchical liouville space propagator to quantum dissipative dynamics. *J. Chem. Phys.* **130**, 084105 (2009).
- [81] Ishizaki, A. & Tanimura, Y. Quantum dynamics of system strongly coupled to low-temperature colored noise bath: Reduced hierarchy equations approach. *J. Phys. Soc. Jpn.* **74**, 3131–3134 (2005).
- [82] Zhu, J., Kais, S., Rebentrost, P. & Aspuru-Guzik, A. Modified scaled hierarchical equation of motion approach for the study of quantum coherence in photosynthetic complexes. *J. Phys. Chem. B* **115**, 1531–1537 (2011).
- [83] Strümpfer, J. & Schulten, K. Open quantum dynamics calculations with the hierarchy equations of motion on parallel computers. *J. Chem. Theory Comput.* **8**, 2808–2816 (2012).
- [84] Kreisbeck, C., Kramer, T., Rodríguez, M. & Hein, B. High-performance solution of hierarchical equations of motion for studying energy transfer in light-harvesting complexes. *J. Chem. Theory Comput.* **7**, 2166–2174 (2011).
- [85] Haken, H. & Strobl, G. An exactly solvable model for coherent and incoherent exciton motion. *Z. Phys. A Hadron. Nucl.* **262**, 135–148 (1973).
- [86] Kolli, A., Nazir, A. & Olaya-Castro, A. Electronic excitation dynamics in multichromophoric systems described via a polaron-representation master equation. *J. Chem. Phys.* **135**, 154112 (2011).
- [87] Jang, S. Theory of multichromophoric coherent resonance energy transfer: A polaronic quantum master equation approach. *J. Chem. Phys.* **135**, 034105 (2011).
- [88] Pollock, F. A., McCutcheon, D. P. S., Lovett, B. W., Gauger, E. M. & Nazir, A. A multi-site variational master equation approach to dissipative energy transfer. *New J. Phys.* **15**, 075018 (2013).
- [89] Mori, H. Transport, collective motion, and brownian motion. *Prog. Theor. Phys.* **33**, 423–455 (1965).
- [90] Dupuis, M. Moment and continued fraction expansions of time autocorrelation functions. *Prog. Theor. Phys.* **37**, 502–537 (1967).
- [91] Cederbaum, L. S., Gindensperger, E. & Burghardt, I. Short-time dynamics through conical intersections in macrosystems. *Phys. Rev. Lett.* **94**, 113003 (2005).
- [92] Gindensperger, E., Burghardt, I. & Cederbaum, L. S. Short-time dynamics through conical intersections in macrosystems. i. theory: Effective-mode formulation. *J. Chem. Phys.* **124**, – (2006).

- 
- [93] Prior, J., Chin, A. W., Huelga, S. F. & Plenio, M. B. Efficient simulation of strong system-environment interactions. *Phys. Rev. Lett.* **105**, 050404 (2010).
- [94] Chin, A. W., Rivas, A., Huelga, S. F. & Plenio, M. B. Exact mapping between system-reservoir quantum models and semi-infinite discrete chains using orthogonal polynomials. *J. Math. Phys.* **51**, 092109 (2010).
- [95] Martinazzo, R., Hughes, K. H. & Burghardt, I. Unraveling a brownian particle's memory with effective mode chains. *Phys. Rev. E* **84**, 030102 (2011).
- [96] Meyer, H.-D., Manthe, U. & Cederbaum, L. The multi-configurational time-dependent hartree approach. *Chem. Phys. Lett.* **165**, 73–78 (1990).
- [97] White, S. R. Density matrix formulation for quantum renormalization groups. *Phys. Rev. Lett.* **69**, 2863–2866 (1992).
- [98] Bose, S. Quantum communication through spin chain dynamics: an introductory overview. *Contemp. Phys.* **48**, 13–30 (2007).
- [99] Makri, N. & Makarov, D. E. Tensor propagator for iterative quantum time evolution of reduced density matrices. i. theory. *J. Chem. Phys.* **102**, 4600–4610 (1995).
- [100] Nalbach, P. & Thorwart, M. Landau-zener transitions in a dissipative environment: Numerically exact results. *Phys. Rev. Lett.* **103**, 220401 (2009).
- [101] Nalbach, P., Ishizaki, A., Fleming, G. R. & Thorwart, M. Iterative path-integral algorithm versus cumulant time-nonlocal master equation approach for dissipative biomolecular exciton transport. *New J. Phys.* **13**, 063040 (2011).
- [102] Hoyer, S., Ishizaki, A. & Whaley, K. B. Spatial propagation of excitonic coherence enables ratcheted energy transfer. *Phys. Rev. E* **86**, 041911 (2012).
- [103] Fassioli, F., Oblinsky, D. G. & Scholes, G. D. Designs for molecular circuits that use electronic coherence. *Faraday Discuss.* **163**, 341–351 (2013).
- [104] Creatore, C., Parker, M. A., Emmott, S. & Chin, A. W. Efficient biologically inspired photocell enhanced by delocalized quantum states. *Phys. Rev. Lett.* **111**, 253601 (2013).
- [105] Nielsen, M. & Chuang, I. *Quantum Computation and Quantum Information* (Cambridge University Press, 2000).
- [106] Yuen-Zhou, J., Krich, J. J., Mohseni, M. & Aspuru-Guzik, A. Quantum state and process tomography of energy transfer systems via ultrafast spectroscopy. *Proc. Natl. Acad. Sci. USA* **108**, 17615–17620 (2011).
- [107] Yuen-Zhou, J. *et al.* Coherent exciton dynamics in supramolecular light-harvesting nanotubes revealed by ultrafast quantum process tomography. *ACS Nano* **8**, 5527–5534 (2014).



- 
- [108] Monras, A., Chęcińska, A. & Ekert, A. Witnessing quantum coherence in the presence of noise. *New J. Phys.* **16**, 063041 (2014).
- [109] Mancál, T. & Valkunas, L. Exciton dynamics in photosynthetic complexes: excitation by coherent and incoherent light. *New J. Phys.* **12**, 065044 (2010).
- [110] Brumer, P. & Shapiro, M. Molecular response in one-photon absorption via natural thermal light vs. pulsed laser excitation. *Proc. Natl. Acad. Sci. USA* **109**, 19575–19578 (2012).
- [111] Fassioli, F., Olaya-Castro, A. & Scholes, G. D. Coherent energy transfer under incoherent light conditions. *J. Phys. Chem. Lett.* **3**, 3136–3142 (2012).
- [112] Sarovar, M., Ishizaki, A., Fleming, G. R. & Whaley, K. B. Quantum entanglement in photosynthetic light-harvesting complexes. *Nat. Phys.* **6**, 462–467 (2010).
- [113] Caruso, F., Chin, A. W., Datta, A., Huelga, S. F. & Plenio, M. B. Entanglement and entangling power of the dynamics in light-harvesting complexes. *Phys. Rev. A* **81**, 062346 (2010).
- [114] Fassioli, F. & Olaya-Castro, A. Distribution of entanglement in light-harvesting complexes and their quantum efficiency. *New J. Phys.* **12**, 085006 (2010).
- [115] Whaley, K. B., Sarovar, M. & Ishizaki, A. Quantum entanglement phenomena in photosynthetic light harvesting complexes. *Procedia Chem.* **3**, 152–164 (2011).
- [116] Ishizaki, A. & Fleming, G. R. Quantum superpositions in photosynthetic light harvesting: delocalization and entanglement. *New J. Phys.* **12**, 055004 (2010).
- [117] Smyth, C., Fassioli, F. & Scholes, G. D. Measures and implications of electronic coherence in photosynthetic light-harvesting. *Philos. Trans. R. Soc., A* **370**, 3728–3749 (2012).
- [118] Scholes, G. D. & Smyth, C. Perspective: Detecting and measuring exciton delocalization in photosynthetic light harvesting. *J. Chem. Phys.* **140**, 110901 (2014).
- [119] Thouless, D. Electrons in disordered systems and the theory of localization. *Phys. Rep.* **13**, 93–142 (1974).
- [120] Davidovich, L. Sub-poissonian processes in quantum optics. *Rev. Mod. Phys.* **68**, 127–173 (1996).
- [121] Scully, M. & Zubairy, S. *Quantum Optics* (Cambridge University Press, 1997).
- [122] Barnett, S. & Radmore, P. *Methods in Theoretical Quantum Optics*. Oxford Series in Optical and Imaging Sciences (Oxford University Press, 2002).

- 
- [123] Kiesel, T. & Vogel, W. Nonclassicality filters and quasiprobabilities. *Phys. Rev. A* **82**, 032107 (2010).
- [124] Kiesel, T., Vogel, W., Bellini, M. & Zavatta, A. Nonclassicality quasiprobability of single-photon-added thermal states. *Phys. Rev. A* **83**, 032116 (2011).
- [125] Mandel, L. Sub-poissonian photon statistics in resonance fluorescence. *Opt. Lett.* **4**, 205–207 (1979).
- [126] Klyshko, D. Observable signs of nonclassical light. *Phys. Lett. A* **213**, 7–15 (1996).
- [127] Miller, W. H. Perspective: Quantum or classical coherence? *J. Chem. Phys.* **136**, 210901 (2012).
- [128] Briggs, J. S. & Eisfeld, A. Equivalence of quantum and classical coherence in electronic energy transfer. *Phys. Rev. E* **83**, 051911 (2011).
- [129] Wilde, M. M., McCracken, J. M. & Mizel, A. Could light harvesting complexes exhibit non-classical effects at room temperature? *Proc. R. Soc. A* **466**, 1347–1363 (2010).
- [130] Olaya-Castro, A., Lee, C. F., Olsen, F. F. & Johnson, N. F. Efficiency of energy transfer in a light-harvesting system under quantum coherence. *Phys. Rev. B* **78**, 085115 (2008).
- [131] Plenio, M. B. & Huelga, S. F. Dephasing-assisted transport: quantum networks and biomolecules. *New J. Phys.* **10**, 113019 (2008).
- [132] Rebentrost, P., Mohseni, M., Kassal, I., Lloyd, S. & Aspuru-Guzik, A. Environment-assisted quantum transport. *New J. Phys.* **11**, 033003 (2009).
- [133] Richards, G. H., Wilk, K. E., Curmi, P. M. G., Quiney, H. M. & Davis, J. A. Coherent vibronic coupling in light-harvesting complexes from photosynthetic marine algae. *J. Phys. Chem. Lett.* **3**, 272–277 (2012).
- [134] Turner, D. B. *et al.* Quantitative investigations of quantum coherence for a light-harvesting protein at conditions simulating photosynthesis. *Phys. Chem. Chem. Phys.* **14**, 4857–4874 (2012).
- [135] Chin, A. W., Huelga, S. F. & Plenio, M. B. Coherence and decoherence in biological systems: principles of noise-assisted transport and the origin of long-lived coherences. *Philos. Trans. R. Soc., A* **370**, 3638–3657 (2012).
- [136] Christensson, N., Kauffmann, H. F., Pullerits, T. & Mancäl, T. Origin of long-lived coherences in light-harvesting complexes. *J. Phys. Chem. B* **116**, 7449–7454 (2012).

- 
- [137] Tiwari, V., Peters, W. K. & Jonas, D. M. Electronic resonance with anticorrelated pigment vibrations drives photosynthetic energy transfer outside the adiabatic framework. *Proc. Natl. Acad. Sci. USA* **110**, 1203–1208 (2013).
- [138] Perdomo, A., Vogt, L., Najmaie, A. & Aspuru-Guzik, A. Engineering directed excitonic energy transfer. *Appl. Phys. Lett.* **96**, 093114 (2010).
- [139] Rey, M. d., Chin, A. W., Huelga, S. F. & Plenio, M. B. Exploiting structured environments for efficient energy transfer: The phonon antenna mechanism. *J. Phys. Chem. Lett.* **4**, 903–907 (2013).
- [140] Biggs, J. D. & Cina, J. A. Using wave-packet interferometry to monitor the external vibrational control of electronic excitation transfer. *J. Chem. Phys.* **131**, 224101 (2009).
- [141] Biggs, J. D. & Cina, J. A. Studies of impulsive vibrational influence on ultrafast electronic excitation transfer. *J. Phys. Chem. A* **116**, 1683–1693 (2012).
- [142] Waldermann, F. C. *et al.* Measuring phonon dephasing with ultrafast pulses using raman spectral interference. *Phys. Rev. B* **78**, 155201 (2008).
- [143] Lee, K. C. *et al.* Entangling macroscopic diamonds at room temperature. *Science* **334**, 1253–1256 (2011).
- [144] Womick, J. M. & Moran, A. M. Vibronic enhancement of exciton sizes and energy transport in photosynthetic complexes. *J. Phys. Chem. B* **115**, 1347–1356 (2011).
- [145] Doust, A. B. *et al.* Developing a structure-function model for the cryptophyte phycoerythrin 545 using ultrahigh resolution crystallography and ultrafast laser spectroscopy. *J. Mol. Biol.* **344**, 135–153 (2004).
- [146] Novoderezhkin, V. I., Doust, A. B., Curutchet, C., Scholes, G. D. & van Grondelle, R. Excitation dynamics in phycoerythrin 545: Modeling of steady-state spectra and transient absorption with modified Redfield theory. *Biophys. J.* **99**, 344–352 (2010).
- [147] Liu, Z. *et al.* Crystal structure of spinach major light-harvesting complex at 2.72 Å resolution. *Nature* **428**, 287–292 (2004).
- [148] Barros, T. & KÄijhlbrandt, W. Crystallisation, structure and function of plant light-harvesting complex II. *Biochim. Biophys. Acta, Bioenerg.* **1787**, 753–772 (2009).
- [149] Novoderezhkin, V. I., Palacios, M. A., van Amerongen, H. & van Grondelle, R. Energy-transfer dynamics in the LHCII complex of higher plants: modified Redfield approach. *J. Phys. Chem. B* **108**, 10363–10375 (2004).

- 
- [150] Novoderezhkin, V. I., Yakovlev, A. G., van Grondelle, R. & Shuvalov, V. A. Coherent nuclear and electronic dynamics in primary charge separation in photosynthetic reaction centers: A Redfield theory approach. *J. Phys. Chem. B* **108**, 7445–7457 (2004).
- [151] Hay, S. & Scrutton, N. S. Good vibrations in enzyme-catalysed reactions. *Nat. Chem.* **4**, 161–168 (2012).
- [152] Dasgupta, J., Frontiera, R. R., Taylor, K. C., Lagarias, J. C. & Mathies, R. A. Ultrafast excited-state isomerization in phytochrome revealed by femtosecond stimulated raman spectroscopy. *Proc. Natl. Acad. Sci. USA* **106**, 1784–1789 (2009).
- [153] Turin, L. A spectroscopic mechanism for primary olfactory reception. *Chem. Senses* **21**, 773–791 (1996).
- [154] Brookes, J. C., Hartoutsiou, F., Horsfield, A. P. & Stoneham, A. M. Could humans recognize odor by phonon assisted tunneling? *Phys. Rev. Lett.* **98**, 038101 (2007).
- [155] Franco, M. I., Turin, L., Mershin, A. & Skoulakis, E. M. C. Molecular vibration-sensing component in drosophila melanogaster olfaction. *Proc. Natl. Acad. Sci. USA* **108**, 3797–3802 (2011).
- [156] Wong, C. Y. *et al.* Electronic coherence lineshapes reveal hidden excitonic correlations in photosynthetic light harvesting. *Nat. Chem.* **5**, 396–404 (2012).
- [157] Schlau-Cohen, G. S. *et al.* Pathways of energy flow in LHCII from two-dimensional electronic spectroscopy. *J. Phys. Chem. B* **113**, 15352–15363 (2009).
- [158] Hayes, D., Griffin, G. B. & Engel, G. S. Engineering coherence among excited states in synthetic heterodimer systems. *Science* **340**, 1431–1434 (2013).
- [159] Samsonoff, W. & MacColl, R. Biliproteins and phycobilisomes from cyanobacteria and red algae at the extremes of habitat. *Arch. Microbiol.* **176**, 400–405 (2001).
- [160] Scholes, G. D., Mirkovic, T., Turner, D. B., Fassioli, F. & Buchleitner, A. Solar light harvesting by energy transfer: from ecology to coherence. *Energy Environ. Sci.* **5**, 9374–9393 (2012).
- [161] Singh, D. K., Srivastava, S. K., Ojha, A. K. & Asthana, B. pH-dependent raman study of pyrrole and its vibrational analysis using DFT calculations. *Spectrochim. Acta, Part A* **71**, 823–829 (2008).
- [162] Zhou, C., Diers, J. R. & Bocian, D. F. Qy-excitation resonance raman spectra of chlorophyll a and related complexes. normal mode characteristics of the low-frequency vibrations. *J. Phys. Chem. B* **101**, 9635–9644 (1997).

- 
- [163] Vöhringer, P. *et al.* Solvent and frequency dependence of vibrational dephasing on femtosecond time-scales. *J. Raman Spectrosc.* **26**, 535–551 (1995).
- [164] Kukura, P., McCamant, D. W. & Mathies, R. A. Femtosecond stimulated raman spectroscopy. *Annu. Rev. Phys. Chem.* **58**, 461–488 (2007).
- [165] Kühn, O., Renger, T. & May, V. Theory of exciton-vibrational dynamics in molecular dimers. *Chem. Phys.* **204**, 99–114 (1996).
- [166] Hossein-Nejad, H., Olaya-Castro, A. & Scholes, G. D. Phonon-mediated path-interference in electronic energy transfer. *J. Chem. Phys.* **136**, 024112 (2012).
- [167] Palma, G. M., Suominen, K.-A. & Ekert, A. K. Quantum computers and dissipation. *Philos. Trans. R. Soc., A* **452**, 567–584 (1996).
- [168] Merlo, M., Haupt, F., Cavaliere, F. & Sassetti, M. Sub-poissonian phononic population in a nanoelectromechanical system. *New J. Phys.* **10**, 023008 (2008).
- [169] Cavaliere, F., Piovano, G., Paladino, E. & Sassetti, M. Phonon distributions of a single-bath mode coupled to a quantum dot. *New J. Phys.* **10**, 115004 (2008).
- [170] Zavatta, A., Parigi, V. & Bellini, M. Experimental nonclassicality of single-photon-added thermal light states. *Phys. Rev. A* **75**, 052106 (2007).
- [171] Silbey, R. & Harris, R. A. Variational calculation of the dynamics of a two level system interacting with a bath. *J. Chem. Phys.* **80**, 2615–2617 (1984).
- [172] Cai, J., Popescu, S. & Briegel, H. J. Dynamic entanglement in oscillating molecules and potential biological implications. *Phys. Rev. E* **82**, 021921 (2010).
- [173] Dorfman, K. E., Voronine, D. V., Mukamel, S. & Scully, M. O. Photosynthetic reaction center as a quantum heat engine. *Proc. Natl. Acad. Sci. USA* **110**, 2746–2751 (2013).
- [174] Eisfeld, A. & Briggs, J. S. Classical master equation for excitonic transport under the influence of an environment. *Phys. Rev. E* **85**, 046118 (2012).
- [175] Mancăl, T. Excitation energy transfer in a classical analogue of photosynthetic antennae. *J. Phys. Chem. B* **117**, 11282–11291 (2013).
- [176] Shi, Q., Chen, L., Nan, G., Xu, R. & Yan, Y. Electron transfer dynamics: Zusman equation versus exact theory. *J. Chem. Phys.* **130**, 164518 (2009).
- [177] León-Montiel, R. d. J. & Torres, J. P. Highly efficient noise-assisted energy transport in classical oscillator systems. *Phys. Rev. Lett.* **110**, 218101 (2013).

- 
- [178] Allen, L. & Eberly, J. *Optical Resonance and Two-level Atoms*. Dover Books on Physics Series (Dover, 1987).
- [179] Davies, R. & Davies, K. On the wigner distribution function for an oscillator. *Ann. Phys.* **89**, 261–273 (1975).
- [180] Scholes, G. D., Fleming, G. R., Olaya-Castro, A. & van Grondelle, R. Lessons from nature about solar light harvesting. *Nat. Chem.* **3**, 763–774 (2012).
- [181] Curutchet, C. *et al.* Electronic energy transfer in condensed phase studied by a polarizable QM/MM model. *J. Chem. Theory Comput.* **5**, 1838–1848 (2009).
- [182] Curutchet, C. *et al.* Energy flow in the cryptophyte PE545 antenna is directed by bilin pigment conformation. *J. Phys. Chem. B* **117**, 4263–4273 (2013).
- [183] Hossein-Nejad, H. & Scholes, G. D. Energy transfer, entanglement and decoherence in a molecular dimer interacting with a phonon bath. *New J. Phys.* **12**, 065045 (2010).
- [184] Sato, Y. & Reynolds, M. F. Resonant coherence in photosynthetic electronic energy transfer by site-dependent pigment-protein interactions. *J. Phys. Chem. B* **118**, 1229–1233 (2014).
- [185] Quan, H. T., Liu, Y.-x., Sun, C. P. & Nori, F. Quantum thermodynamic cycles and quantum heat engines. *Phys. Rev. E* **76**, 031105 (2007).
- [186] Horodecki, M. & Oppenheim, J. Fundamental limitations for quantum and nanoscale thermodynamics. *Nat. Commun.* **4** (2013).
- [187] Skrzypczyk, P., Short, A. J. & Popescu, S. Work extraction and thermodynamics for individual quantum systems. *Nat. Commun.* **5** (2014).
- [188] Campisi, M., Blattmann, R., Kohler, S., Zueco, D. & Hänggi, P. Employing circuit QED to measure non-equilibrium work fluctuations. *New J. Phys.* **15**, 105028 (2013).
- [189] Herbert, R. *et al.* Phototrophic purple sulfur bacteria as heat engines in the south andros black hole. *Photosynthesis Research* **95**, 261–268 (2008).
- [190] Scully, M. O., Chapin, K. R., Dorfman, K. E., Kim, M. B. & Svidzinsky, A. Quantum heat engine power can be increased by noise-induced coherence. *Proc. Natl. Acad. Sci. USA* **108**, 15097–15100 (2011).
- [191] Alicki, R. The quantum open system as a model of the heat engine. *J. Phys. A: Math. Gen.* **12**, L103 (1979).
- [192] Talkner, P., Lutz, E. & Hänggi, P. Fluctuation theorems: Work is not an observable. *Phys. Rev. E* **75**, 050102 (2007).

- 
- [193] Campisi, M., Hänggi, P. & Talkner, P. Colloquium: Quantum fluctuation relations: Foundations and applications. *Rev. Mod. Phys.* **83**, 771–791 (2011).
- [194] Mazzola, L., De Chiara, G. & Paternostro, M. Measuring the characteristic function of the work distribution. *Phys. Rev. Lett.* **110**, 230602 (2013).
- [195] Dorner, R. *et al.* Extracting quantum work statistics and fluctuation theorems by single-qubit interferometry. *Phys. Rev. Lett.* **110**, 230601 (2013).
- [196] Watanabe, G., Venkatesh, B. P., Talkner, P., Campisi, M. & Hänggi, P. Quantum fluctuation theorems and generalized measurements during the force protocol. *Phys. Rev. E* **89**, 032114 (2014).
- [197] Venkatesh, B. P., Watanabe, G. & Talkner, P. Transient quantum fluctuation theorems and generalized measurements. *New J. Phys.* **16**, 015032 (2014).
- [198] Weimer, H., Henrich, M. J., Rempp, F., Schröder, H. & Mahler, G. Local effective dynamics of quantum systems: A generalized approach to work and heat. *EPL* **83**, 30008 (2008).
- [199] Schröder, H. & Mahler, G. Work exchange between quantum systems: The spin-oscillator model. *Phys. Rev. E* **81**, 021118 (2010).
- [200] Zhu, L., Liu, H., Xie, W. & Shi, Q. Explicit system-bath correlation calculated using the hierarchical equations of motion method. *J. Chem. Phys.* **137**, 194106 (2012).
- [201] Jesenko, S. & Žnidarič, M. Excitation energy transfer efficiency: Equivalence of transient and stationary setting and the absence of non-markovian effects. *J. Chem. Phys.* **138**, 174103 (2013).
- [202] Harrop, S. J. *et al.* Single-residue insertion switches the quaternary structure and exciton states of cryptophyte light-harvesting proteins. *Proc. Natl. Acad. Sci. USA* (2014).
- [203] Hu, X., Ritz, T., Damjanović, A., Autenrieth, F. & Schulten, K. Photosynthetic apparatus of purple bacteria. *Q. Rev. Biophys.* **35**, 1–62 (2002).
- [204] Cogdell, R. J. *et al.* How photosynthetic bacteria harvest solar energy. *J. Bacteriol.* **181**, 3869–3879 (1999).
- [205] Scheuring, S. & Sturgis, J. N. Chromatic adaptation of photosynthetic membranes. *Science* **309**, 484–487 (2005).
- [206] Hu, X., Ritz, T., Damjanović, A. & Schulten, K. Pigment organization and transfer of electronic excitation in the photosynthetic unit of purple bacteria. *J. Phys. Chem. B* **101**, 3854–3871 (1997).

- 
- [207] Koepke, J., Hu, X., Muenke, C., Schulten, K. & Michel, H. The crystal structure of the light-harvesting complex II (B800–850) from *rhodospirillum rubrum*. *Structure* **4**, 581–597 (1996).
- [208] Fassio, F., Olaya-Castro, A., Scheuring, S., Sturgis, J. N. & Johnson, N. F. Energy transfer in light-adapted photosynthetic membranes: From active to saturated photosynthesis. *Biophys. J.* **97**, 2464–2473 (2009).
- [209] Harel, E., Long, P. D. & Engel, G. S. Single-shot ultrabroadband two-dimensional electronic spectroscopy of the light-harvesting complex {LH2}. *Opt. Lett.* **36**, 1665–1667 (2011).
- [210] Humphrey, W., Dalke, A. & Schulten, K. VMD – Visual Molecular Dynamics. *J. Mol. Graph.* **14**, 33–38 (1996).
- [211] Polli, D. *et al.* Carotenoid-bacteriochlorophyll energy transfer in {LH2} complexes studied with 10-fs time resolution. *Biophys. J.* **90**, 2486–2497 (2006).
- [212] McLuskey, K., Prince, S. M., Cogdell, R. J. & Isaacs, N. W. The crystallographic structure of the B800-820 LH3 light-harvesting complex from the purple bacteria *rhodospirillum rubrum* strain 7050. *Biochemistry (Mosc.)* **40**, 8783–8789 (2001).
- [213] Cogdell, R., Howard, T., Isaacs, N., McLuskey, K. & Gardiner, A. Structural factors which control the position of the qy absorption band of bacteriochlorophyll a in purple bacterial antenna complexes. *Photosynth. Res.* **74**, 135–141 (2002).
- [214] Mascle-Allemand, C., Dunquesne, K., Lebrun, R., Scheuring, S. & Sturgis, N., James. Antenna mixing in photosynthetic membranes from *phaeospirillum rubrum*. *Proc. Natl. Acad. Sci. USA* **107**, 5537–5562 (2010).
- [215] Brotsudarmo, T. H. P. *et al.* The light intensity under which cells are grown controls the type of peripheral light-harvesting complexes that are assembled in a purple photosynthetic bacterium. *Biochem. J.* **440**, 51–61 (2011).
- [216] Chen, L., Zheng, R., Shi, Q. & Yan, Y. Optical line shapes of molecular aggregates: Hierarchical equations of motion method. *J. Chem. Phys.* **131**, 094502 (2009).
- [217] Lax, M. The franck-condon principle and its application to crystals. *J. Chem. Phys.* **20**, 1752–1760 (1952).
- [218] Kubo, R. & Toyozawa, Y. Application of the method of generating function to radiative and non-radiative transitions of a trapped electron in a crystal. *Prog. Theor. Phys.* **13**, 160–182 (1955).
- [219] Mukamel, S. Non-markovian theory of molecular relaxation. I. vibrational relaxation and dephasing in condensed phases. *Chem. Phys.* **37**, 33–47 (1979).



- [220] Jang, S. & Silbey, R. J. Theory of single molecule line shapes of multichromophoric macromolecules. *J. Chem. Phys.* **118**, 9312–9323 (2003).
- [221] Schröder, M., Kleinekathöfer, U. & Schreiber, M. Calculation of absorption spectra for light-harvesting systems using non-markovian approaches as well as modified Redfield theory. *J. Chem. Phys.* **124**, 084903 (2006).
- [222] Roden, J., Strunz, W. T. & Eisfeld, A. Non-markovian quantum state diffusion for absorption spectra of molecular aggregates. *J. Chem. Phys.* **134**, 034902 (2011).
- [223] Knox, R. S., Small, G. J. & Mukamel, S. Low-temperature zero phonon lineshapes with various brownian oscillator spectral densities. *Chem. Phys.* **281**, 1–10 (2002).
- [224] Jang, S., Dempster, S. E. & Silbey, R. J. Characterization of the static disorder in the B850 band of LH2. *J. Phys. Chem. B* **105**, 6655–6665 (2001).
- [225] Ketelaars, M. *et al.* Spectroscopy on the B850 band of individual light-harvesting 2 complexes of rhodospseudomonas acidophila I. experiments and monte carlo simulations. *Biophys. J.* **80**, 1591–1603 (2001).
- [226] Hofmann, C., Aartsma, T. J. & Köhler, J. Energetic disorder and the B850-exciton states of individual light-harvesting 2 complexes from rhodospseudomonas acidophila. *Chem. Phys. Lett.* **395**, 373–378 (2004).
- [227] Sumi, H. Theory on rates of excitation-energy transfer between molecular aggregates through distributed transition dipoles with application to the antenna system in bacterial photosynthesis. *J. Phys. Chem. B* **103**, 252–260 (1999).
- [228] Scholes, G. D. & Fleming, G. R. On the mechanism of light harvesting in photosynthetic purple bacteria: B800 to B850 energy transfer. *J. Phys. Chem. B* **104**, 1854–1868 (2000).
- [229] Scholes, G. D., Jordanides, X. J. & Fleming, G. R. Adapting the Förster theory of energy transfer for modeling dynamics in aggregated molecular assemblies. *The Journal of Physical Chemistry B* **105**, 1640–1651 (2001).
- [230] Jang, S., Newton, M. D. & Silbey, R. J. Multichromophoric Förster resonance energy transfer. *Phys. Rev. Lett.* **92**, 218301 (2004).
- [231] Reddy, N., Small, G., Seibert, M. & Picorel, R. Energy transfer dynamics of the B800-B850 antenna complex of rhodobacter sphaeroides: a hole burning study. *Chem. Phys. Lett.* **181**, 391–399 (1991).
- [232] Novoderezhkin, V., Wendling, M. & van Grondelle, R. Intra- and interband transfers in the B800-B850 antenna of rhodospirillum molischianum: A Redfield theory modeling of polarized pump-probe kinetics. *J. Phys. Chem. B* **107**, 11534–11548 (2003).

- [233] Herek, J. *et al.* B800→B850 energy transfer mechanism in bacterial LH2 complexes investigated by B800 pigment exchange. *Biophys. J.* **78**, 2590–2596 (2000).
- [234] Cheng, Y. C. & Silbey, R. J. Coherence in the B800 ring of purple bacteria LH2. *Phys. Rev. Lett.* **96**, 028103 (2006).
- [235] Sundström, V., Pullerits, T. & van Grondelle, R. Photosynthetic light-harvesting: Reconciling dynamics and structure of purple bacterial LH2 reveals function of photosynthetic unit. *J. Phys. Chem. B* **103**, 2327–2346 (1999).
- [236] Tretiak, S., Middleton, C., Chernyak, V. & Mukamel, S. Bacteriochlorophyll and carotenoid excitonic couplings in the LH2 system of purple bacteria. *J. Phys. Chem. B* **104**, 9540–9553 (2000).
- [237] Prince, S. *et al.* Apoprotein structure in the LH2 complex from *rhodospseudomonas acidophila* strain 10050: modular assembly and protein pigment interactions. *J. Mol. Biol.* **268**, 412–423 (1997).
- [238] Mukai, K., Abe, S. & Sumi, H. Theory of rapid excitation-energy transfer from B800 to optically-forbidden exciton states of B850 in the antenna system LH2 of photosynthetic purple bacteria. *J. Phys. Chem. B* **103**, 6096–6102 (1999).
- [239] Strümpfer, J. & Schulten, K. Light harvesting complex II B850 excitation dynamics. *J. Chem. Phys.* **131**, 225101 (2009).
- [240] Novoderezhkin, V. I., Rutkauskas, D. & van Grondelle, R. Dynamics of the emission spectrum of a single LH2 complex: Interplay of slow and fast nuclear motions. *Biophys. J.* **90**, 2890–2902 (2006).
- [241] Kunz, R. *et al.* Fluorescence-excitation and emission spectra from {LH2} antenna complexes of *rhodospseudomonas acidophila* as a function of the sample preparation conditions. *J. Phys. Chem. B* **117**, 12020–12029 (2013).
- [242] Novoderezhkin, V. & van Grondelle, R. Spectra and dynamics in the B800 antenna: Comparing hierarchical equations, Redfield and Förster theories. *J. Phys. Chem. B* **117**, 11076–11090 (2013).
- [243] Sarovar, M. & Whaley, K. B. Design principles and fundamental trade-offs in biomimetic light harvesting. *New J. Phys.* **15**, 013030 (2013).
- [244] Takagahara, T., Hanamura, E. & Kubo, R. Stochastic models of intermediate state interaction in second order optical processes - stationary response. II. *J. Phys. Soc. Jpn.* **43**, 811–816 (1977).
- [245] Novoderezhkin, V. Combined Förster-Redfield theory for modeling energy transfer in plant photosynthetic antenna complexes. *Biochemistry (Moscow) Supplement Series A: Membrane and Cell Biology* **6**, 314–319 (2012).

- 
- [246] Cleary, L. & Cao, J. Optimal thermal bath for robust excitation energy transfer in disordered light-harvesting complex 2 of purple bacteria. *New J. Phys.* **15**, 125030 (2013).
- [247] Ihalainen, J. A. *et al.* Energy transfer in LH2 of rhodospirillum molischianum, studied by subpicosecond spectroscopy and configuration interaction exciton calculations. *J. Phys. Chem. B* **105**, 9849–9856 (2001).
- [248] Salverda, J. M., van Mourik, F., van der Zwan, G. & van Grondelle, R. Energy transfer in the B800 rings of the peripheral bacterial light-harvesting complexes of rhodopseudomonas acidophila and rhodospirillum molischianum studied with photon echo techniques. *J. Phys. Chem. B* **104**, 11395–11408 (2000).
- [249] Bergström, H., Sundström, V., van Grondelle, R., Gillbro, T. & Cogdell, R. Energy transfer dynamics of isolated B800-850 and B800-820 pigment-protein complexes of rhodobacter sphaeroides and rhodopseudomonas acidophila. *Biochim. Biophys. Acta, Bioenerg.* **936**, 90–98 (1988).
- [250] Ferretti, M. *et al.* The nature of coherences in the B820 bacteriochlorophyll dimer revealed by two-dimensional electronic spectroscopy. *Phys. Chem. Chem. Phys.* **16**, 9930–9939 (2014).
- [251] Ritz, T., Park, S. & Schulten, K. Kinetics of excitation migration and trapping in the photosynthetic unit of purple bacteria. *J. Phys. Chem. B* **105**, 8259–8267 (2001).
- [252] Chandler, D. E., Strümpfer, J., Sener, M., Scheuring, S. & Schulten, K. Light harvesting by lamellar chromatophores in rhodospirillum rubrum. *Biophys. J.* **106**, 2503–2510 (2014).
- [253] Novoderezhkin, V., Monshouwer, R. & van Grondelle, R. Electronic and vibrational coherence in the core light-harvesting antenna of rhodopseudomonas viridis. *J. Phys. Chem. B* **104**, 12056–12071 (2000).
- [254] Romero, E. *et al.* Quantum coherence in photosynthesis for efficient solar-energy conversion. *Nat. Phys.* **10**, 676–682 (2014).